UNIVERSITY OF CALIFORNIA, SAN DIEGO

From Channel Modeling to Signal Processing for Bit Patterned Media Recording

A dissertation submitted in partial satisfaction of the
requirements for the degree
Doctor of Philosophy

in

Electrical Engineering
(Communication Theory and Systems)

by

Seyhan Karakulak

Committee in charge:

Professor Paul H. Siegel, Co-Chair
Professor Jack K. Wolf, Co-Chair
Professor Raymond A. de Callafon
Professor Eric Fullerton
Professor William S. Hodgkiss, Jr.

2010

The dissertation of Seyhan Karakulak is approved, and it is acceptable in quality and form for publication on microfilm and electronically:

_____

_____

_____

_____
Co-Chair

_____
Co-Chair

University of California, San Diego

2010

DEDICATION

In loving memory of my paternal and maternal grandparents,
this thesis is dedicated to my parents and my sisters.

CONTENTS

LIST OF FIGURES

LIST OF TABLES

ACKNOWLEDGEMENTS

I am deeply grateful to my advisors Prof. Paul H. Siegel and Prof. Jack K. Wolf for their guidance, wisdom, kindness, encouragement, and patience throughout my graduate studies. They are the role models of scientists not only with high achievements in their fields but also with perseverance, integrity, honesty, and their dedication to teaching and to their students.

I am grateful to Prof. H. Neal Bertram for starting my thesis work by his read channel model for bit-patterned media recording. I am indebted to his explanations of the underlying physics and his collaboration at any stage. I admire how he combines his passion for music and science in his life.

I would like to thank my committee members Prof. Raymond de Callafon, Prof. William Hodgkiss, and Prof. Eric Fullerton for their comments and time. I am thankful to Prof. Eric Fullerton for many discussions on bit-patterned media recording and for the self-assembly specimen he provided for AFM and MFM images in Chapter 2.

I am thankful to Prof. Alon Orlitsky for being my academic advisor on my first year. Many thanks to professors in the ECE department. I am thankful to Prof. Vitaliy Lomakin, Dr. Fred Spada, and Dr. Boris Livshitz for many discussions on bit-patterned media. Many thanks to Dr. Fred Spada for the AFM and MFM images of bit-patterned media specimens in Chapter 2. I am thankful to my supervisor Dr. Amood Khandekar in my internship at Qualcomm for his guidance.

STAR Lab and WOLF Lab members are very distinct in their support and group dynamics. Many thanks to former and current members, and visiting scholars of STAR Lab and WOLF Lab for helping me in my research, fruitful discussions, and the great workspace: Eitan Yaakobi, Junsheng Han, Zheng Wu, Sharon Aviran, Joseph Soriaga, Mike Cheng, Zienab Taghavi, Federica Garin, Panu Chaichanavong, Brian Butler, Ido Tal, Han Wang, Aravind Iyengar, Hossein Taghavi, Amir Hadi Djahanshadi, Ismail Demirkan, Lynn Greiner, Xiaojie (Eric) Zhang, Saeed Sharifi Tehrani, Marco Papaleo, and Ori Shental. Thanks to my colleagues in the ECE department whose names I could not list here. Special thanks to my former and current officemates Zeinab Taghavi, Federica Garin, and Eitan Yaakobi.

I am very thankful to Betty Manoulian, Iris Villanueva, Jan Neumann, Ray Descoteaux, and Nate Heintzman for their excellence in administrative assistance. Special thanks to ECE staff, especially to Gennie Miranda, Megan Scott, and Bernadette Villaluz.

I would like to thank all of my friends for all the joy, courage, support, and friendship

they brought to my life. I am very thankful to Barış for his encouragement, friendship and for being there from the beginning.

I am deeply thankful to my parents and sisters for their everlasting love, encouragement, and friendship. Their sense of humor has always brightened my days. This dissertation would not be possible without their support and love.

This thesis is supported by CMRR Sponsors Funds and the National Science Foundation (grant numbers H98230-05-P-1485, H98230-07-P-0728, NSA H98230-09-P-0074).

Portions of Chapter 3 appear in the the paper: S. Karakulak, P. H. Siegel, J. K. Wolf, and H. N. Bertram, "A new read channel model for patterned media storage," *IEEE Trans. Magn.*, vol. 44, pp. 193-197, Jan. 2008. Portions of Chapter 4 appear in the the papers: S. Karakulak, P. H. Siegel, J. K. Wolf, and H. N. Bertram, "A new read channel model for patterned media storage," *IEEE Trans. Magn.*, vol. 44, pp. 193-197, Jan. 2008, S. Karakulak, P. H. Siegel, J. K. Wolf, and H. N. Bertram, "Equalization and detection in patterned media recording," *Intermag Dig. of Tech. Papers*, p. HT10, May 2008, and S. Karakulak, P. H. Siegel, J. K. Wolf, and H. N. Bertram, "Joint-track equalization and detection in patterned media recording," submitted to *IEEE Trans. Magn.*, 2008. Portions of Chapter 5 appear in the the paper: S. Karakulak, P. H. Siegel, and J. K. Wolf, "A Parametric Study of Inter-Track Interference in Bit Patterned Media Record," *IEEE Trans. Magn.*, vol. 46, pp. 819-824, Mar. 2010.

VITA

2003	B.S., Electronics and Communications Engineering, Istanbul Technical University, Istanbul
2004	B.S., Mathematics, Istanbul Technical University, Istanbul
2007	M.S., Electrical Engineering, University of California, San Diego
2010	Ph.D., Electrical Engineering, University of California, San Diego

PUBLICATIONS

S. Karakulak, P. H. Siegel, J. K. Wolf, and H. N. Bertram, "A new read head model for patterned media storage," *The Magnetic Recording Conference*, Minneapolis, Minnesota, May 2007, USA.

S. Karakulak, P. H. Siegel, J. K. Wolf, and H. N. Bertram, "A new read channel model for patterned media storage," *IEEE Trans. Magn.*, vol. 44, no. 1, pp. 193-197, Jan. 2008.

S. Karakulak, P. H. Siegel, J. K. Wolf, and H. N. Bertram, "Equalization and detection for patterned media recording," *The International Magnetics Conference*, May 2008, Madrid, Spain.

S. Karakulak, P. H. Siegel, J. K. Wolf, and H. N. Bertram, "Joint-track equalization and detection for patterned media recording," submitted to *IEEE Trans. Magn.*, Oct. 2008.

S. Karakulak, P. H. Siegel, and J. K. Wolf, "A parametric study of inter-track interference in bit patterned media recording," *The Magnetic Recording Conference*, Tuscaloosa, Alabama, Oct 2009, USA.

S. Karakulak, P. H. Siegel, and J. K. Wolf, "A Parametric Study of Inter-Track Interference in Bit Patterned Media Record," *IEEE Trans. Magn.*, vol. 46, pp. 819-824, Mar. 2010.

ABSTRACT OF THE DISSERTATION

From Channel Modeling to Signal Processing for Bit Patterned Media Recording

by

Seyhan Karakulak
Doctor of Philosophy in Electrical Engineering
(Communication Theory and Systems)

University of California San Diego, 2010

Professor Paul H. Siegel, Co-Chair
Professor Jack K. Wolf, Co-Chair

Bit-patterned media (BPM) recording is one method proposed to overcome the density limitations imposed by the superparamagnetic effect in continuous recording media. Channel modeling, equalization, and detection aspects of BPM recording are studied in this dissertation.

In BPM recording, each bit is recorded on a single domain "island." A read channel model for BPM recording is introduced where the signal contribution from each island is evaluated. Intersymbol interference (ISI) and inter-track interference (ITI) are observed in the model due to the considered head/media geometries. The noise that arises from write/read electronics is modeled by additive white Gaussian noise (AWGN). In the model, the main component of the media noise, which is called "island jitter", is assumed to arise from the location fluctuations of islands. Island position shift in the down-track and cross-track directions is modeled with two independent Gaussian random variables. It has been shown that the jitter-induced readback voltage is non-Gaussian. Therefore, higher order approximation for the jitter-induced readback voltage is more accurate in terms of capturing the statistical properties of this noise source.

Schemes that utilize different equalization and detection methods are compared for BPM recording channels. A maximum-likelihood (ML) bit sequence detector using the Viterbi algorithm with the modified branch metric is presented for a special case of a symmetric channel response matrix. Joint-track equalization was introduced in the literature before in the context of a single interfering track. A scheme is proposed which utilizes joint-track equalization followed by a Viterbi detector for BPM recording channels. For certain recording densities, simulation

results show that the performance of this scheme is comparable to that of the much more complex schemes utilizing optimal bit detection or optimal symbol sequence detection. The proposed scheme also outperforms another scheme of the same complexity introduced in the literature.

A parametric study of ITI for BPM recording channel is presented. A surprising phenomenon is observed in the performance curves of optimal bit detectors: The detector performance improved for a certain range of increasing ITI levels for channels both with and without ISI and in the absence as well as in the presence of track misregistration (TMR). For the no-ISI case, this behavior is explained by means of an exact probability of error analysis for the maximum *a posteriori* (MAP) bit detector, i.e. optimal bit detector. An error event analysis of a punctured ML joint-track detector is used to understand the observed effects of ITI on system performance for channels with ISI.

Chapter 1

Introduction to Magnetic Recording

1.1 Introduction

With the rapidly evolving digital computer age and spreading of internet usage all over the world, the demand for data storage is expected to significantly increase. Magnetic storage devices, optical discs, and flash memory-based solid state devices are some of the storage systems that are widely used to satisfy this growing demand. In addition to having higher storage capacity, other desired features in a data storage system are non-volatility, which is being able to retain the recorded data in the absence of power, and random access, which is being capable of reaching a desired data/track fast.

The two features, namely non-volatility and random access, have been realized practically since the fabrication of the IBM 350 Disk Drive in 1956. Fig. 1.1 shows the picture of this first commercial magnetic hard disk drive which weighed more than 500 lb with capacity of only 5 MB. With the advances in materials design, head design techniques, mechanical design, signal processing, and coding, an incredible reduction in the size and price, and an ever increasing data storage capability have been achieved. Such a reduced price and portability enabled the widespread usage of hard disk drives in many systems that require data storage.

In digital storage, the data is a stream of binary digits (bits), namely 0's and 1's. In magnetic hard disk drives, the stream of bits is encoded into a stream of bipolar channel symbols $\{-1, +1\}$ that is recorded by magnetizing the continuous thin magnetic film in two different directions corresponding to -1 and $+1$'s.

There are two magnetic recording technologies called longitudinal recording and perpendicular recording which were developed sequentially. In longitudinal recording, the medium

Figure 1.1 The IBM 350 Disk Drive (with permission from Hitachi Global Storage Technologies).

anisotropy is oriented in the thin film plane whereas it is aligned perpendicular to the film plane in perpendicular recording [1]. Due to enabling the usage of a soft underlayer (SUL), higher recording densities are achieved with perpendicular recording. Advances in the head design such as the introduction of a magnetoresistive (MR) head significantly reduced the sizes of disks.

In continuous media, a bit is recorded on a number of magnetic grains which are magnetized in the same direction. In order to increase the recording density, one can shrink the bit size. This reduces the number of magnetic grains per bit. However, there is a lower limit in terms of the number of grains per bit since a sufficient number of grains per bit is necessary to maintain an acceptable signal-to-noise ratio (SNR). To reduce the bit size, the grain diameters can be scaled. On the other hand, as grain sizes are reduced, thermal fluctuations can spontaneously reverse the grain magnetization direction.

Bit patterned media (BPM) where each bit is recorded on a predefined, single domain “island" may provide an alternative to conventional continuous media for higher recording densities. For this new type of media, not only will the media manufacturing process change, but

also the head design, signal processing, and many other system features will be affected.

The main focus of this dissertation is channel modeling, equalization, and detection for BPM recording channels. In the remainder of this chapter, we review channel modeling, signal processing, and coding for a typical recording system with continuos media. Later, in Chapter 2, we present the fabrication and writing process for BPM, and an overview of signal processing and coding techniques for a BPM recording system.

1.2 Channel Modeling

A model that reflects the channel input/output relationship close to the physical reality is one of the crucial components in a data storage system design. Since it is only a model and is designed for efficient detection and coding algorithms, it does not completely represent the underlying physics of the data storage system. Nevertheless, a chosen model can be improved by incorporating models for errors in the writing/reading process as well as for noise sources that arise from the imperfections in the recording media or from the read/write electronics.

In a hard disk drive, the stream of bits are recorded on a thin film consisting of magnetic grains. Each bit is recorded by a write head which magnetizes a number of grains in the same direction. Since the media is continuous, no writing synchronization is needed for recording. In longitudinal recording, the media anisotropy is horizontal to the film plane whereas in perpendicular recording, the media anisotropy is perpendicular to the film plane. When the orientation of the media changes, an isolated transition response occurs in the read head.

The noiseless readback signal in a recording system with a continuous media is represented by a linear model

$$v(t) = \sum_i u_i \, g(t - iT) \tag{1.1}$$

where $\{u_i\}$ represents the stream of coded bits from the alphabet $\{-1, +1\}$ and $g(t)$, called the dipulse response, represents an approximation to the channel response of an isolated bit. Here, T represents the time required for the read head to move from one bit to the next one. The dipulse response is

$$g(t) = \frac{1}{2}(h(t) - h(t - T)) \tag{1.2}$$

where $h(t)$ represents the channel response to an isolated transition. For longitudinal recording,

the isolated transition is approximated by a Lorentzian pulse, shown in Fig. 1.2, defined as

$$h(t) = \frac{A}{1 + (\frac{2t}{PW50})^2} \tag{1.3}$$

where A denotes the peak amplitude and $PW50$ represents the width of the pulse at half the peak amplitude.

For perpendicular recording, an isolated transition response can be approximated by an error function [2]

$$h(t) = A \cdot \text{erf}\left(\frac{2\sqrt{\ln 2}\, t}{PW50}\right) \tag{1.4}$$

where $PW50$ is the width of the derivative of the transition response at half of its peak amplitude and the error function is defined as

$$\text{erf}(t) = \frac{2}{\sqrt{\pi}} \int_0^t e^{-x^2}\, dx. \tag{1.5}$$

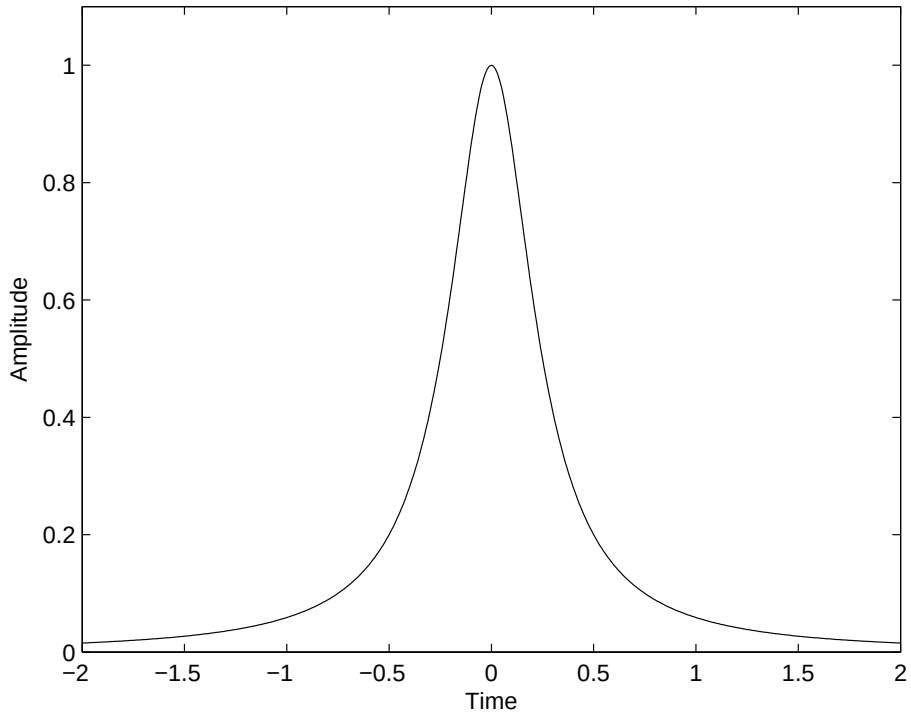

Figure 1.2 The isolated transition response in longitudinal recording represented by a Lorentzian pulse where $A = 1$ and $PW50 = 1$.

Fig. 1.3 shows the isolated transition response for perpendicular recording.

The electronics noise and head noise $n(t)$ can be modeled by additive white Gaussian noise (AWGN). Then the readback signal takes the form of

$$y(t) = \sum_i u_i \, g(t - iT) + n(t). \tag{1.6}$$

The dominant noise in a recording system comes from the media, which is called "media noise" [3]. The main component of this noise source is "transition noise" which occurs due to the randomness of the grain shapes at the bit transition [3]-[2]. The readback signal $y(t)$ then can be modeled as

$$y(t) = \sum_i u_i \, g(t + t_i - iT) + n(t) \tag{1.7}$$

where t_i represents the transition jitter for the input bit u_i and is modeled with a Gaussian distribution.

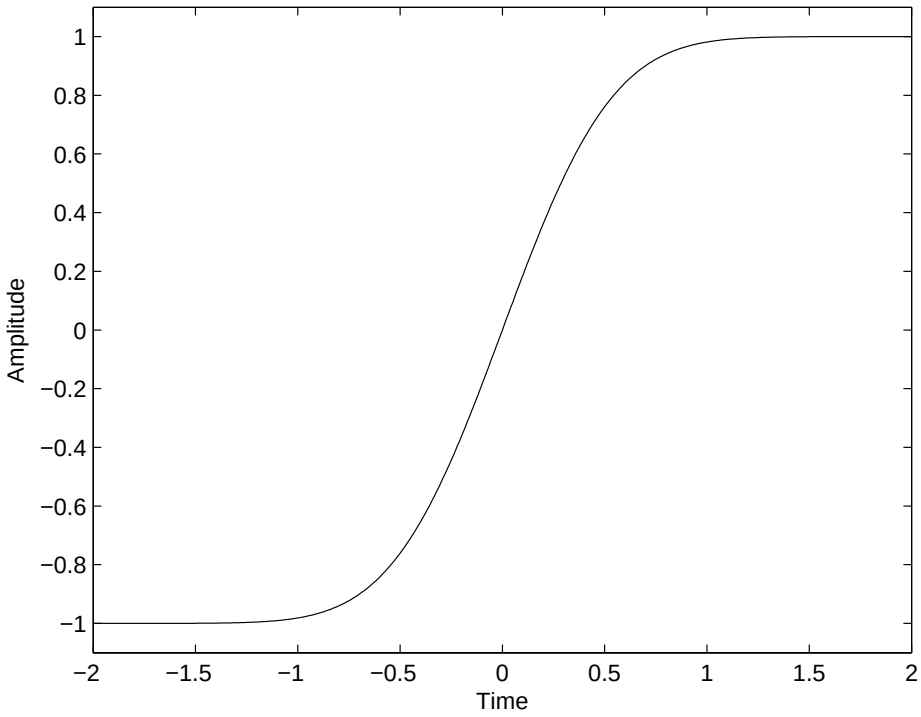

Figure 1.3 The isolated transition response in perpendicular recording represented by an error function where $A = 1$ and $PW50 = 0.5$.

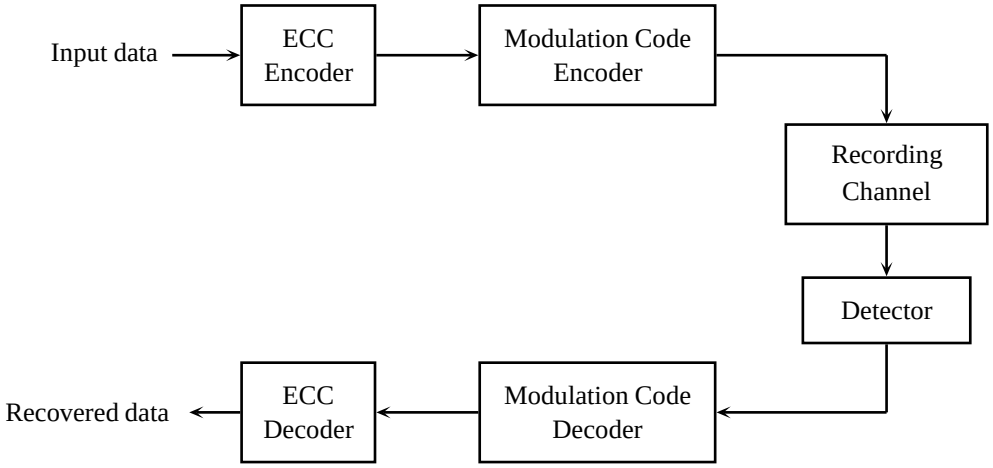

Figure 1.4 A typical data storage system.

In order to increase the recording density, the bit size is reduced, resulting in fewer grains per bit. Such a reduction in the size of each bit introduces inter-symbol interference (ISI) due to the smaller size of bit separation along the track. When the track pitch is reduced, the intertrack interference (ITI) becomes an important source of interference when the read head senses signals from the neighboring tracks. Also the linear model assumption might become invalid for higher recording densities [4]. A more realistic channel model should include the effect of interfering signals along the track and in the cross-track direction as well as the non-linearities that could arise from higher recording densities.

In the next section, we review the signal processing and coding techniques for magnetic recording channels that can combat the ISI and ITI, media noise, and many other imperfections arising in a recording system.

1.3 Signal Processing and Coding for Magnetic Recording Channels

Fig. 1.4 shows a typical data storage system that consists of an error correction code (ECC) encoder/decoder, a modulation code encoder/decoder, the recording channel, and the detector. Error correction coding is utilized to eliminate the errors that occur due to the noise in the recording channel whereas modulation coding is utilized for timing recovery and in order to enhance the channel performance by encoding the data stream into a more noise resilient stream.

Advanced equalization, detection, and coding techniques enabled higher capacity and more reliable storage. In this section, we review different detection techniques including partial-

response maximum-likelihood detection, noise-predictive maximum-likelihood detection, and error correction coding for magnetic recording channels.

1.3.1 Equalization and Detection

In the early stages of magnetic recording systems with low recording densities, each transition was separated well enough for *peak detection* to be efficient. In peak detection, the peaks in the readback signal correspond to the transitions which are then used to recover the channel input. However, with increasing recording densities, the smaller separation between transitions introduces ISI. For such a case, peak detection becomes an unreliable method since it can not resolve the ISI.

To combat ISI, a new approach was taken. Rather than viewing the ISI as a phenomenon to eliminate, a partial-response (PR) channel which allows ISI in a controlled manner with maximum-likelihood (ML) sequence detection is introduced. This new approach is called partial-response maximum-likelihood (PRML) detection. For ML sequence detection, the Viterbi algorithm is utilized which works on a trellis representing the channel input and noiseless channel output sequences. The discrete channel output, which is obtained by sampling the continuous channel output with a sampling interval corresponding to the bit separation, is fed to the Viterbi detector which outputs the most likely bit sequence. The complexity of the Viterbi algorithm is linear in the number of states and in the length of the sequence. However, the number of states in the trellis increases exponentially with the length of the channel response. Therefore, for more manageable complexity, the sampled channel outputs are equalized to a PR channel response with a limited length.

The reduced length of the channel response comes at the cost of noise enhancement and noise coloration. When the Viterbi algorithm, which is optimal for white noise, is utilized for detection, the performance is degraded to an extent that depends on the amount of noise enhancement and noise coloration. To improve the performance of a PRML system, noise-predictive maximum-likelihood (NPML) detectors were introduced [5]-[6]. An NPML system involves a generalized partial response (GPR) target with arbitrary real number coefficients which whitens the noise before detection. The complexity of detection is increased due to the usage of longer GPR targets compared to the PR targets.

For media noise which is data dependent, a new detection method is introduced that exploits the pattern dependency in the signal distortion and noise reflected in the noise metrics. This new technique is called patterned-dependent noise-predictive maximum-likelihood (PDNP-

ML) detection [7]. PDNP-ML detection can be viewed as a generalization of NPML detection. These new techniques enhanced the detection performance for recording channels with more complex noise sources such as media noise [8].

1.3.2 Error Correction Codes

In order to correct errors in magnetic recording disk drives, Reed-Solomon (RS) codes with hard decision decoding have been utilized for decades. The error correction capability of these codes with hard decision decoding is largely determined by its minimum distance. However, with hard decision decoding of RS codes, the rates are far away from the Shannon limit, namely the channel capacity, which is the highest rate for which reliable communication is possible [9].

For decades, no known codes achieved reliable performance at rates near the Shannon limit. With the introduction of turbo codes with iterative decoders in 1993 [10], the traditional way of code design with good minimum distances has been reformed. Later, low-density parity check (LDPC) codes, which were introduced by Gallager a long time ago [11], have been shown to perform close to the Shannon limit [12]-[15]. It is expected that these advanced codes will find more use in hard disk drives, a viewpoint supported by the recent integration of LDPC codes with iterative detection into a hard disk read channel in [16].

Bibliography

[1] H. Zhou, T. Roscamp, R. Gustafson, E. Boerner, and R. Chantrell, “Physics of longitudinal and perpendicular recording.” *Coding and Signal Processing for Magnetic Recording Systems*, B. Vasic and E. Kurtas, CRS Press, 2005.

[2] X. Yang and E. M. Kurtas, “Signal and noise generation for magnetic recording channel simulations.” *Coding and Signal Processing for Magnetic Recording Systems*, B. Vasic and E. Kurtas, CRS Press, 2005.

[3] H. N. Bertram, *Theory of Magnetic Recording*. Cambridge University Press, 1994.

[4] J. P. Caroselli, “Modeling, analysis, and mitigation of medium noise in thin film magnetic recording channels.” Ph.D. dissertation, University of California, San Diego, 1998.

[5] E. Eleftheriou and W. Hirt, “Improving performance of PRML/EPRML through noise prediction,” *IEEE Trans. Magn.*, vol. 32, pp. 3968–3970, Sept. 1996.

[6] J. Coker, E. Eleftheriou, R. Galbraith, and W. Hirt, “Noise-predictive maximum likelihood (NPML) detection,” *IEEE Trans. Magn.*, vol. 34, pp. 110–117, Jan. 1998.

[7] A. Kavcic and J. Moura, “The Viterbi algorithm and Markov noise memory,” *IEEE Trans. Inform. Theory*, vol. 46, pp. 291–301, Jan. 2000.

[8] J. Moon and J. Park, “Pattern-dependent noise prediction in signal-dependent noise,” *IEEE J. Select. Areas Commun.*, vol. 19, pp. 730–743, Apr. 2001.

[9] C. E. Shannon, “A mathematical theory of communication,” *Bell System Technical Journal*, vol. 27, pp. 379–423, 625–656, Jul., Oct. 1948.

[10] C. Berrou, A. Glavieux, and P. Thitimajshima, “Near Shannon limit error-correcting coding and decoding: Turbo-codes. 1,” in *Proc. IEEE International Conf. on Communications (ICC’93)*, vol. 2, pp. 1064–1070 vol.2, May 1993.

[11] R. G. Gallager, *Low-Density Parity-Check Codes*. The M. I. T. Press, 1963.

[12] D. MacKay and R. Neal, “Near Shannon limit performance of low density parity check codes,” *Elect. Lett.*, vol. 32, p. 1645, Aug. 1996.

[13] M. Sipser and D. Spielman, “Expander codes,” *IEEE Trans. Inform. Theory*, vol. 42, pp. 1710–1722, Nov. 1996.

[14] D. Spielman, “Linear-time encodable and decodable error-correcting codes,” *IEEE Trans. Inform. Theory*, vol. 42, pp. 1723–1731, Nov. 1996.

[15] D. MacKay, “Good error-correcting codes based on very sparse matrices,” *IEEE Trans. Inform. Theory*, vol. 45, pp. 399–431, Mar. 1999.

[16] R. L. Galbraith, T. Oenning, M. Ross, B. Wilson, I. Djurdjevic, and J. Park, “Architecture and implementation of a first-generation iterative detection read channel,” *IEEE Trans. Magn.*, vol. 46, pp. 837–843, Mar. 2010.

Chapter 2

Introduction to Bit Patterned Media Recording

2.1 Introduction

The recording density in hard disk drives is measured in terms of areal density, i.e. the number of bits per square inch. To increase the recording densities, the areal density needs to be increased. In conventional magnetic recording systems, a thin continuous magnetic layer which consists of magnetic grains is utilized for recording. Each bit consists of a number of magnetic grains that are magnetized in the same direction, behaving as one unit.

By scaling the number of grains per bit, the areal density can be increased. However, due to the randomness in the grain size and shape, the transition from one bit to another might introduce a considerable amount of noise, called transition jitter, to the readback signal. This is illustrated in Fig. 2.1. Therefore, in order to obtain sufficient signal-to-noise ratio (SNR) for each recorded bit, the number of magnetic grains per bit can not be decreased beyond a certain number. Grains with smaller diameters can be utilized to increase the recording densities. However, grains with small diameters become thermally unstable by the superparamagnetic effect, i.e. the magnetic energy of the grain K_uV is not large enough compared to the thermal energy k_BT. Here, K_u and V, respectively, represent the magnetic anisotropy and the magnetic switching volume of a grain whereas k_B and T, respectively, represent the Boltzmann constant and the temperature. If grains with large magnetic anisotropy are utilized to eliminate the superparamagnetic effect, the required magnetic field for writing is increased. However, the magnetic field of the write element is limited. Therefore, to magnetize or to change the polarity of a grain,

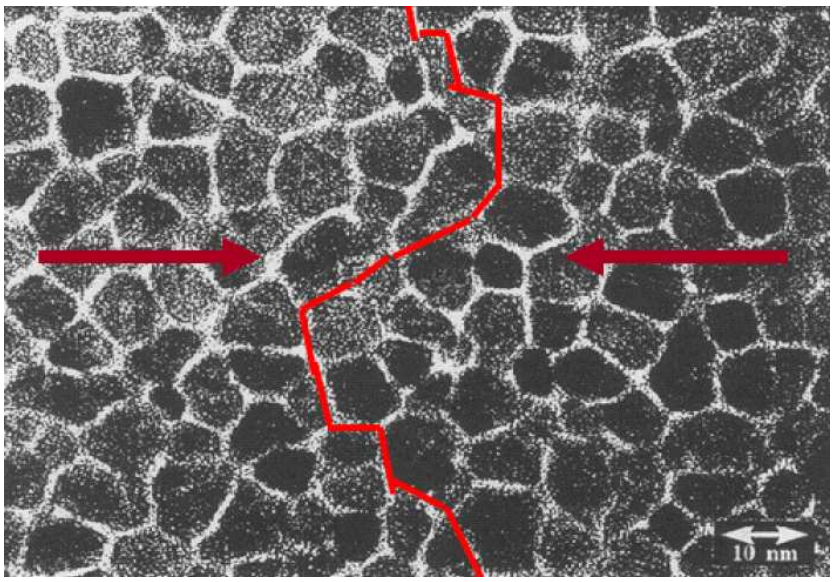

Figure 2.1 Illustration of a transition in continuous film media. Taken from [2] with permission.

the magnetic anisotropy of the grain needs to be reduced by means of recording techniques with energy assistance such as in heat-assisted magnetic recording (HAMR) [1].

There are two other methods proposed for higher recording densities that require patterning of the continuous media, i.e. discrete track media and bit-patterned media (BPM). In discrete track media, the magnetic film is patterned by means of lithography. The tracks are separated by a nonmagnetic material. Such a technique reduces the interference coming from different tracks, mitigates the effects of track misregistration arising from improper positioning of the write/read elements, and increases the tolerance on the dimensions of write/read elements [3]-[5]. On the other hand, since the data is recorded on tracks in continuous media, the transition noise is still a problem and the superparamagnetic effect is inevitable for increasing recording densities.

In order to combat the superparamagnetic effect, the media is patterned to magnetic "islands" where each island can store an individual bit in BPM recording [6]-[7]. Each island consists of one grain or a few coupled grains. There is non-magnetic material between islands. Such a system offers a great potential for recording densities beyond 1 Tb/in^2. Due to the patterned transitions along the track and in the cross-track directions, less transition noise is observed in BPM in contrast to the continuous media.

Many challenges for BPM recording need to be addressed for this new recording

method to be successful. Such challenges include, but not limited to, the media fabrication, the write/read head and servo design, signal processing, coding, and system integration. It might take time to overcome these challenges and we might have to settle for a slower pace of increasing recording densities in the near future.

In the remainder of this chapter, we briefly summarize the media fabrication, the writing process, servo and timing recovery, written-in errors, signal processing and coding for BPM recording channels. In Section 2.6, we present an overview of this dissertation, whose focus is on channel modeling and signal processing aspects of BPM recording channels.

2.2 Fabrication Process

To achieve high recording densities with BPM, one challenge is to fabricate patterned disks with the properties necessary for successful magnetic recording at a reasonable cost. E-beam lithography, nanoimprint lithography, and self-assembly are some of the techniques proposed for the fabrication of BPM. The first step in the mass fabrication process of patterned disks is the creation of a master pattern. With the current technology, creation of the master pattern is a time-consuming and expensive process. At the second step, templates are created by replicating the master pattern which is followed by the third stage where the templates are replicated to create the patterned disks. The second and the third stage, shown in Fig. 2.2, can be carried out at a reasonable cost by nanoimprint technology. In the rest of this section, we briefly summarize e-beam lithography, self-assembly, and guided self-assembly techniques and the process of fabricating a patterned disk from a master pattern with nanoimprint technology. More information about these techniques and other techniques not mentioned here can be found in [8].

The master pattern can be obtained by several techniques such as lithography, self-assembly, or guided self-assembly. Optical lithography can not meet the higher resolutions required for the recording densities targeted for BPM. Another lithography technique called as e-beam lithography is a candidate to generate a master pattern with the areal density up to 1Tb/in^2 [10]. Fig. 2.3(a) and Fig. 2.3(b), respectively, show a height and a phase image of a specimen patterned by e-beam lithography and with dimension of 1 μm. The height image is obtained by an atomic force microscope (AFM) whereas the phase image is obtained by a magnetic force microscope (MFM). In e-beam lithography, the writing process is serial, which results in a slow and expensive procedure to obtain the master pattern. To achieve recording

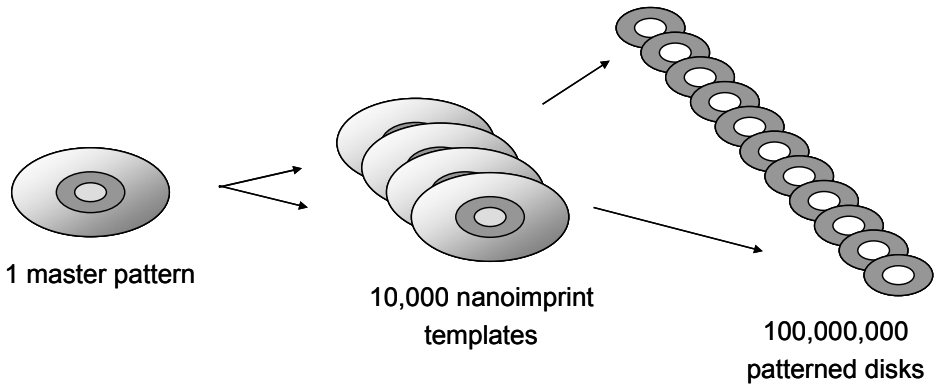

Figure 2.2 Two-generation nanoimprinting process. Taken from [9] with permission.

densities more than 1Tb/in^2, self-assembly is another proposed technique to create the master pattern. Self-assembly is a natural lithography method where the self-assembled patterns are found in nature. These self-assembled patterns can be utilized as a template. The disadvantage of this technique is the missing circular symmetry which is needed for a rotating disk. Fig. 2.4 shows AFM and MFM images of a self-assembled pattern.

In order to overcome the problems observed in the self-assembly method, such as long range ordering and placement jitter, a guided self-assembly method is proposed. This method combines natural assembly with a lithography process. In the guided self-assembly process, a topographical pattern is created physically in a substrate or the surface chemistry is modified to accommodate the specified form of pattern [9].

Once a master pattern is created, it is later replicated by nanoimprint lithography. A simple process is demonstrated in Fig. 2.5 where a patterned disk is created through a master pattern serving as a nanoimprint template. In the process, first a master pattern is created by e-beam lithography. Later, a resist pattern on the master pattern is developed by reactive ion-etching (RIE) and the master pattern is inverted and pressed into the liquid resist layer. By means of UV light, the liquid resist layer is hardened into a solid replica of the master pattern. Later, pillars are formed by means of reactive ion etching. In the last step, to create the magnetic islands, magnetic material is deposited on top of pillars.

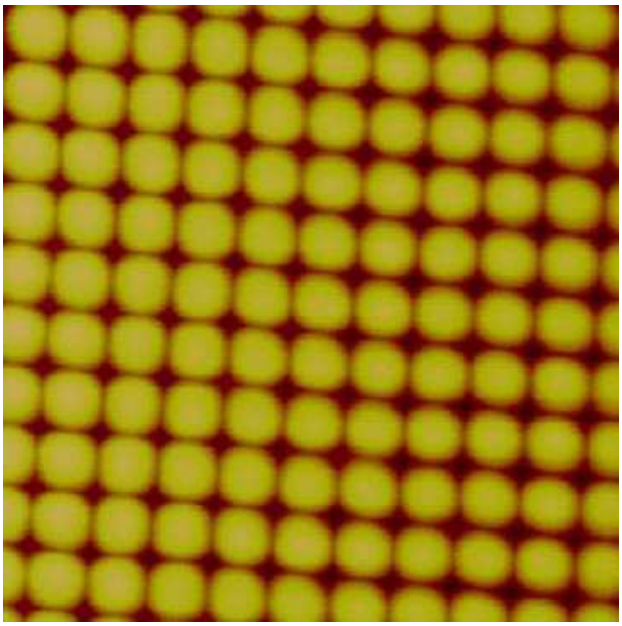

(a) AFM image of an e-beam pattern specimen

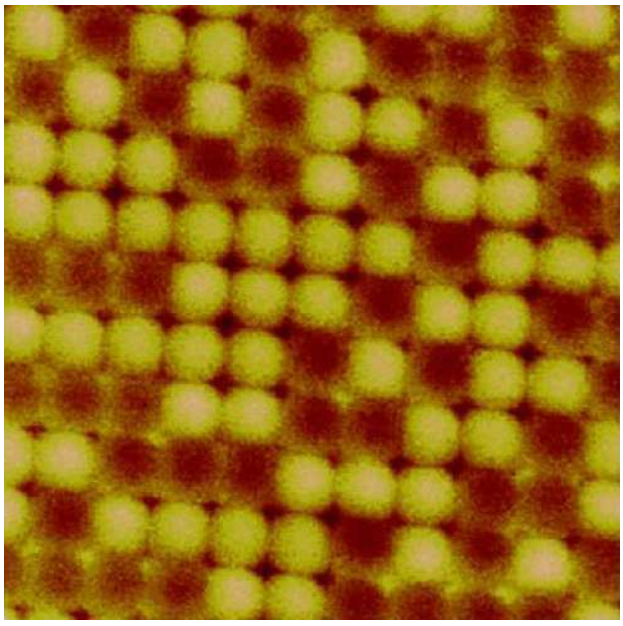

(b) MFM image of an e-beam pattern specimen

Figure 2.3 AFM and MFM images of e-beam pattern specimen with dimension of 1 μm.

2.3 Writing Process: Servo and Timing Recovery

During the fabrication process of continuous media, servo markers are recorded around each track for the purpose of successful write synchronization. Tight write synchronization is

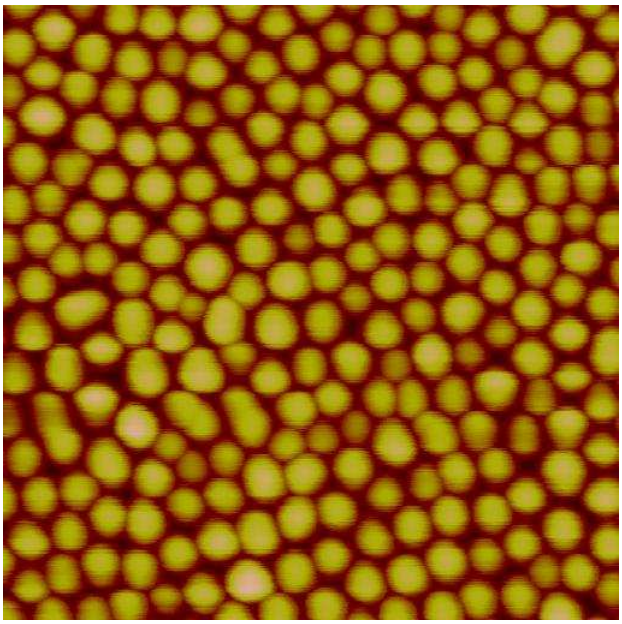

(a) AFM image of a self-assembled pattern specimen

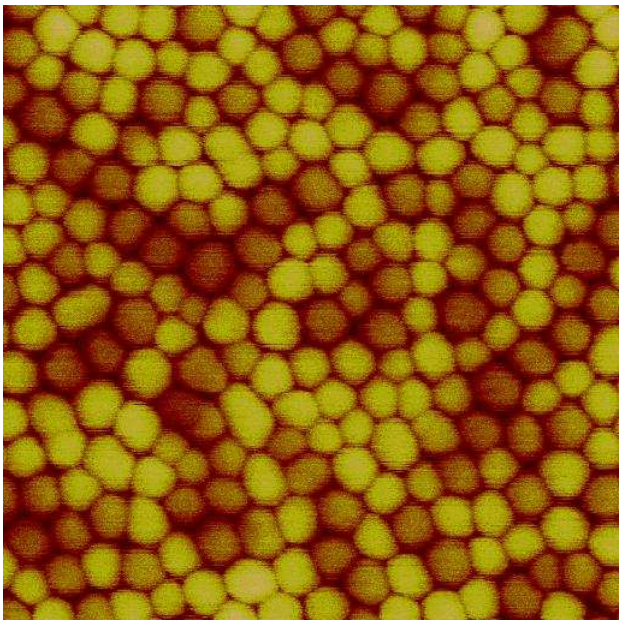

(b) MFM image of a self-assembled pattern specimen

Figure 2.4 AFM and MFM images of a self-assembled pattern specimen with dimension of $1\ \mu m$.

not required in continuous media since the entire film is available for recording. The main difference between the writing process in continuous media and BPM is the necessity of tight

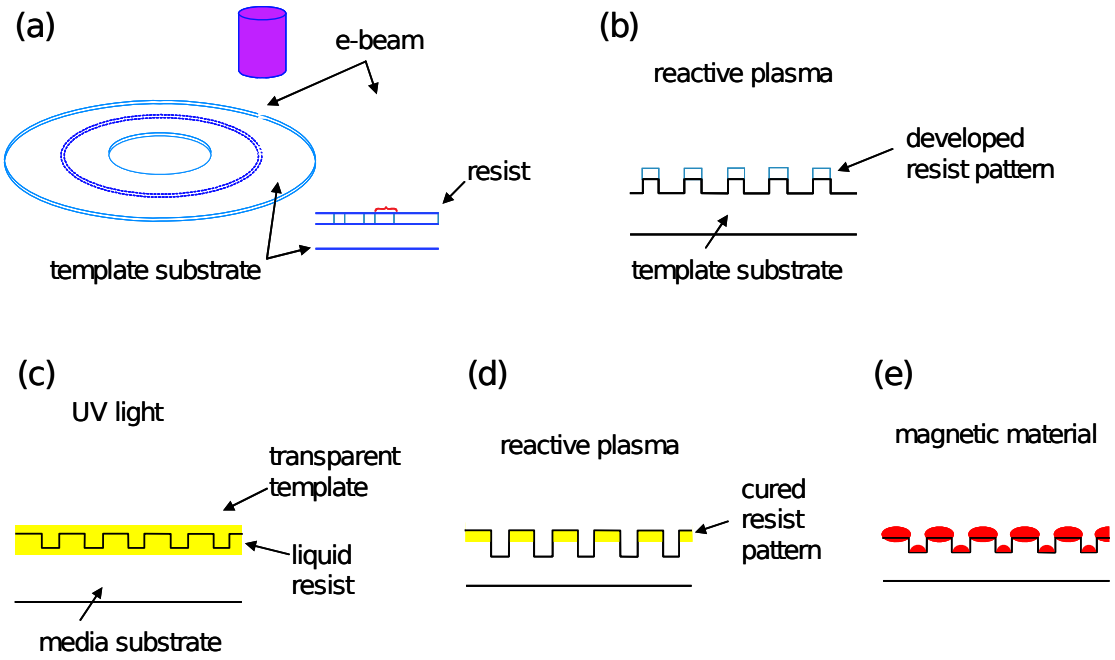

Figure 2.5 Fabrication process of patterned disk through a master pattern. Taken from [9] with permission.

writing synchronization in BPM. In BPM, islands are located at specific places which need to be known by the write head for proper synchronization during the recording process [6].

The location of each island can be determined by a read sensor. The frequency and phase of the write clock can then be updated for successful recording. However, a major interference in the readback signal coming from the large currents applied to the write element degrades the signal level coming from the read sensor. To overcome this effect, other techniques are proposed such as usage of an independent sensor [9]. On the other hand, such new techniques can be prohibitively complex and costly.

One successful method for write synchronization would be the using of sector synchronization system which does not require simultaneous sensing and recording. In this system, with sector headers, successful update in frequency and phase is possible. The major drawback of such a system is that there is no write synchronization control between sectors. For sector synchronization in BPM, advanced servo patterns for frequency and phase update are studied in [11]-[14]. The comparison of servo performance of these patterns in the presence of media noise, signal sampling, and timing jitter is presented in [14].

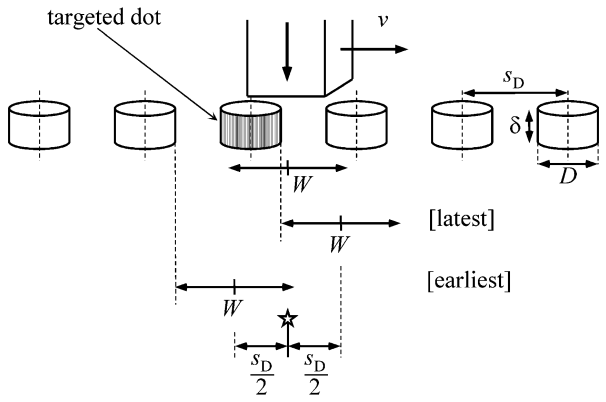

Figure 2.6 Illustration of timing window where W represents the write width and s_D represents the writing window. Taken from [15] with permission.

2.4 Written-in Errors

The recording performance of BPM will largely be dominated by errors that occur in the writing process [15]. The errors in the writing process can arise from imperfect write synchronization or from imperfections in the fabrication process. In the fabrication process, the imperfections might be due to the fluctuations in magnetic properties of the media or in island size, shape, and location.

The location width of the write head where a successful recording is possible for a specified island is defined as the "writing window" [16]. In BPM recording, the write head needs to be synchronized by the targeted island. This is illustrated in Fig. 2.6. There could be scenarios where the head might not move to the writing window of the current island, instead being in the writing window of the previous or the next island. Even when the write head is in the writing window of the island desired to be magnetized, the write field should be larger than the magnetic switching field of that island for successful magnetization. Therefore, successful recording of an island is determined by many factors including, but not limited to, the randomness in the island size, shape, and location, the switching field distribution of the islands, and the write field distribution of the write head.

In [17], the writing failure is modeled by a simple model where only substitution errors are assumed to be present. A substitution error refers to the opposite polarity compared to the desired polarity. In [18], a more general notion for successful recording, called “addressability,” which refers to successful magnetization of a targeted island without detrimentally affecting the

neighboring islands is defined. If the write head changes the magnetization of the previous island due to the write mis-synchronization, then the previous island is overwritten. Such a writing failure introduces a deletion error. Moreover, there could be scenarios where an insertion error can also occur.

2.5 Signal Processing and Coding

From the read channel aspect, several models as well as signal processing techniques for BPM recording are studied in the literature. Due to smaller island separation in the down-track and cross-track directions for high recording densities, the read channel experiences of inter-symbol interference (ISI) and intertrack interference (ITI). Two-dimensional as well as one-dimensional equalization and detection techniques are studied to combat the effects of ISI and ITI. Channel models incorporating the media noise arising from the imperfections in the fabrication process such as the fluctuations in island size and shape are also considered. Another natural step would be to consider applying error correction codes for channel models with ISI and ITI.

As we have discussed above, the performance of BPM recording channels is largely dominated by written-in errors, i.e. substitution, insertion, and deletion errors. In [17], a channel model combining the write and read process with several detection schemes is presented. It has been assumed that only substitution errors occur in the write process and the read channel is modeled as an ISI channel. However, it is crucial to design write channel models with insertion/deletion errors in addition to substitution errors. Advanced signal processing and coding techniques are required for such channels with written-in errors. In the literature, several error correction codes are designed for channels with insertion/deletion errors [19]-[24]. Such codes can be applicable to BPM recording channels.

Information theoretical limits for write/read channels are important from the aspect of code design that can correct the errors that occur in the write and read process. Information rates of the composite channel with different written-in error parameters and read channel models are presented in [17]. Bounds for the capacity and symmetric information rate are presented for a new channel model incorporating insertion/deletion errors in [25].

2.6 Dissertation Overview

Integration of BPM to a functional recording system requires overcoming many challenges. In this dissertation, we are interested in the signal processing aspect of this new recording system from the read channel point of it.

In Chapter 3, we introduce a read channel model with ISI and ITI which arise from the readback signal of islands in the down-track and cross-track directions, respectively. We assume that additive white Gaussian noise (AWGN) occurs due to the electronics noise. We also consider media noise whose major component arises from the island location fluctuations. We model the location fluctuations in the down-track and cross-track directions with independent Gaussian random variables. Later, we show that media noise is non-Gaussian and pattern dependent.

In Chapter 4, we study equalization and detection techniques for the read channel model with AWGN noise that we introduced in Chapter 3. We compare the detection performance of several schemes with different equalization and detection techniques where only the bit sequence on the main track is detected in the presence of ITI. We propose the use of joint-track equalization which was previously introduced in the literature in the context of a single interfering track [26]. Simulation results show that for certain recording densities, the scheme with joint-track equalization and maximum-likelihood sequence detection has performance similar to that of an optimal detection scheme and outperforms another low-complexity detection scheme introduced in the literature [27].

In the last chapter of this thesis, we present a parametric study of ITI for BPM recording channels. Simulation results for optimal bit detection show that increasing ITI level does not necessarily degrade the performance. In contrast, for a certain range of ITI levels, increasing the ITI level improves the performance. This interesting phenomenon arises in the absence as well as in the presence of ISI and track misregistration (TMR). By exact analysis of bit error rates in the absence of ISI, we explain this phenomenon. In the presence of ISI, since the analysis of bit error rates for optimal bit detection in the presence of ITI is difficult, we explain the effect of different levels of ITI by analysis of the dominant error events of another detector called a punctured maximum-likelihood (ML) joint-track detector. The performance of this detector is virtually identical to the optimal bit detector.

Bibliography

[1] J. M. Ruigrok, R. Coehoorn, S. R. Cumpson, and H. W. Kesteren, "Disk recording beyond 100 Gb/in2: Hybrid recording?," *Journal of Applied Physics*, vol. 87, pp. 5398–5403, May 2000.

[2] H. N. Bertram, *Theory of Magnetic Recording*. Cambridge University Press, 1994.

[3] L. F. Shew, "Discrete tracks for saturation magnetic recording," *IEEE Trans. Electronic Computers*, vol. 12, pp. 383–387, Aug. 1963.

[4] Y. Soeno, M. Moriya, K. Ito, K. Hattori, A. Kaizu, T. Aoyama, M. Matsuzaki, and H. Sakai, "Feasibility of discrete track perpendicular media for high track density recording," *IEEE Trans. Magn.*, vol. 39, pp. 1967–1971, July 2003.

[5] K. Hattori, K. Ito, Y. Soeno, M. Takai, and M. Matsuzaki, "Fabrication of discrete track perpendicular media for high recording density," *IEEE Trans. Magn.*, vol. 40, pp. 2510–2515, July 2004.

[6] R. L. White, R. M. H. New, and R. F. W. Pease, "Patterned media: A viable route to 50 Gbit/in^2 and up for magnetic recording?," *IEEE Trans. Magn.*, vol. 33, pp. 990–995, Jan. 1997.

[7] G. F. Hughes, "Patterned media recording systems - the potential and the problems," *Intermag Dig. of Tech. Papers*, p. GA6, Apr. 2002.

[8] B. Terris and T. Thomson, "Nanofabricated and self-assembled magnetic structures as data storage media," *Journal of Physics D*, vol. 38, pp. R199–222, 2005.

[9] T. R. Albrecht, O. Hellwig, R. Ruiz, M. E. Schabes, B. D. Terris, and X. Z. Wu, "Bit patterned magnetic recording, nanoscale magnetic islands for data storage." *Nanoscale Magnetic Materials and Applications*, J.P. Liu., E. Fullerton, O. Gutfleisch, and D. J. Sellmyer, Springer, 2009.

[10] X. Yang, S. Xiao, W. Wu, Y. Xu, K. Mountfield, R. Rottmayer, D. K. Kim Lee, and D. Weller, "Challenges in 1 Teradot / in2 dot patterning using electron beam lithography for bit-patterned media," *J. Vac. Sci. Technol.*, vol. 25, pp. 2202–2209, 2007.

[11] X. Lin, J. Zhu, and W. Messner, "Investigation of advanced position error signal patterns in patterned media," *Journal of Applied Physics*, vol. 87, pp. 5117–5119, May 2000.

[12] E. Hughes and W. Messner, "New servo pattern for hard disk storage using pattern media," *Journal of Applied Physics*, vol. 93, pp. 7002–7004, May 2003.

[13] E. Hughes and W. Messner, "Characterization of three servo patterns for position error signal generation in hard drives," *Proc. American Control Conference*, vol. 5, pp. 4317–4322, June 2003.

[14] Y. Han and R. de Callafon, "Evaluating track-following servo performance of high-density hard disk drives using patterned media," *IEEE Trans. Magn.*, vol. 45, pp. 5352–5359, Dec. 2009.

[15] H. J. Richter, A. Y. Dobin, O. Heinonen, K. Z. Gao, R. J. M. v. d. Veerdonk, R. T. Lynch, J. Xue, D. Weller, P. Asselin, M. F. Erden, and R. M. Brockie, "Recording on bit-patterned media at densities of 1Tb/in^2 and beyond," *IEEE Trans. Magn.*, vol. 42, pp. 2255–2260, Oct. 2006.

[16] B. Livshitz, A. Inomata, H. Bertram, and V. Lomakin, "Semi-analytical approach for analysis of BER in conventional and staggered bit patterned media," *IEEE Trans. Magn.*, vol. 45, pp. 3519–3522, Oct. 2009.

[17] J. Hu, T. Duman, E. Kurtas, and M. Erden, "Bit-patterned media with written-in errors: Modeling, detection, and theoretical limits," *IEEE Trans. Magn.*, vol. 43, pp. 3517–3524, Aug. 2007.

[18] M. E. Schabes, "The write process and thermal stability in bit-patterned recording media," *Joint MMM/Intermag Dig. of Tech. Papers*, p. DA05, Jan. 2007.

[19] J. Sellers, F., "Bit loss and gain correction code," *IRE Trans. Inform. Theory*, vol. 8, pp. 35–38, Jan. 1962.

[20] V. I. Levenshtein, "Binary codes capable of correcting deletions, insertions and reversals," *Sov. Phys. Dokl.*, vol. 10, pp. 707–710, Feb. 1966.

[21] L. Calabi and W. Hartnett, "A family of codes for the correction of substitution and synchronization errors," *IEEE Trans. Inform. Theory*, vol. 15, pp. 102–106, Jan. 1969.

[22] E. Tanaka and T. Kasai, "Synchronization and substitution error-correcting codes for the Levenshtein metric," *IEEE Trans. Inform. Theory*, vol. 22, pp. 156–162, Mar. 1976.

[23] M. Davey and D. MacKay, "Reliable communication over channels with insertions, deletions, and substitutions," *IEEE Trans. Inform. Theory*, vol. 47, pp. 687–698, Feb. 2001.

[24] H. Ferreira, K. Abdel-Ghaffar, L. Cheng, T. Swart, and K. Ouahada, "Moment balancing templates: Constructions to add insertion/deletion correction capability to error correcting or constrained codes," *IEEE Trans. Inform. Theory*, vol. 55, pp. 3494–3500, Aug. 2009.

[25] A. R. Iyengar, P. H. Siegel, and J. K. Wolf, "Data-dependent write channel model for magnetic recording," *accepted to the IEEE International Symposium on Inform. Theory*, June 2010.

[26] B. G. Roh, S. U. Lee, J. Moon, and Y. Chen, "Single-head/single-track detection in interfering tracks," *IEEE Trans. Magn.*, vol. 38, pp. 1830–1838, July 2002.

[27] S. Nabavi and B. V. K. V. Kumar, "Modifying Viterbi algorithm to mitigate inter-track interference in bit-patterned media," *IEEE Trans. Magn.*, vol. 43, pp. 2274–2276, June 2007.

Chapter 3

A New Read Channel Model for Bit Patterned Media Recording

3.1 Introduction

For bit patterned media (BPM) recording, several read channel models taking into account such properties of this new recording media as its geometry are introduced in the literature [1]-[2]. In this chapter, we introduce a technique to compute the output of BPM recording channels with read heads whose dimensions are larger than an island of magnetization. This technique allows the signal contribution due to the inter-track interference (ITI) from adjacent tracks to be evaluated.

Reading is accomplished with a finite track-width magnetoresistive (MR) head with infinitely wide shields. The head potential distribution is obtained using reciprocity calculations and is modified for the presence of a soft underlayer (SUL) using the method of multiple images [3]. The contribution of a magnetized island to the readback signal is evaluated as the integral of the head potential distribution over that island.

In the read channel model, the readback signal is passed through a low-pass filter, followed by a sampler with a sampling interval corresponding to the down-track island separation. Electronics noise, modeled as additive white Gaussian noise (AWGN), is assumed to corrupt the output of the read head. In the model, it is assumed that the main component of the media noise arises from the location fluctuations of islands. This noise source is called “island jitter.” Island position shift in the down-track and cross-track directions is modeled with two independent Gaussian random variables and a second-order model for the approximation to the

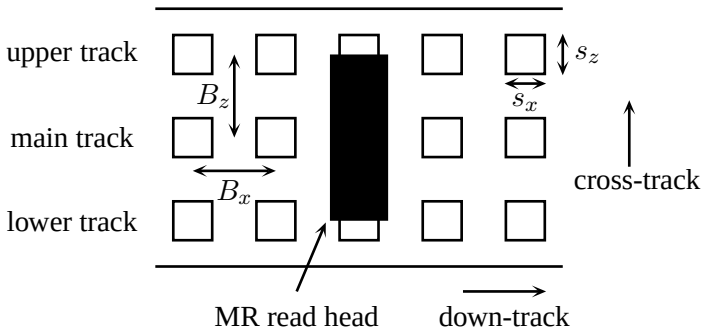

Figure 3.1 Schematic of the magnetoresistive head and patterned magnetic medium.

jitter-induced readback voltage is introduced. The numerically calculated probability density functions indicate that this noise source is data-dependent and non-Guassian.

3.2 Head/Media Configurations

In the read channel model, the islands are arranged in a rectangular array with dimension s_x in the down-track direction and with dimension s_z in the cross-track direction. The islands have a film thickness of h. Center to center island distances in the down-track and cross-track directions, respectively, are equal to B_x and B_z. This is shown schematically in Fig. 3.1. The recording density is determined by the parameters B_x and B_z. Table 3.1 shows media configurations as an example for recording densities between 1 Tb/in^2 and 2 Tb/in^2. In the table, the parameter B_z which determines the track period is set to 25 nm whereas the parameter B_x is scaled down to obtain higher recording densities. In order to obtain higher recording densities, either one or both of the center to center island distances in the down-track and cross-track directions can be reduced.

Table 3.1 Media configurations for recording densities between 1 Tb/in^2 and 2 Tb/in^2.

Recording Density	s_x	s_z	B_x	B_z
1 Tb/in^2	12.5 nm	12.5 nm	25 nm	25 nm
1.2 Tb/in^2	11 nm	12.5 nm	21.5 nm	25 nm
1.4 Tb/in^2	9 nm	12.5 nm	18.4 nm	25 nm
1.75 Tb/in^2	7 nm	12.5 nm	14.7 nm	25 nm
2 Tb/in^2	6 nm	12.5 nm	12.9 nm	25 nm

Reading is accomplished with a finite track-width shielded magnetoresistive (MR) head with infinitely wide shields. The top view of such a shielded MR head is shown in Fig. 3.2. In the figure, W stands for the head width, t stands for the thickness of the MR element, and g stands for the gap from shield to the MR element. The read head centered over the main track spans a specified fraction of the outer tracks (*upper track* and *lower track*, respectively) as shown in Fig. 3.1.

3.3 Head Potential Distribution and Readback Voltage

In the absence of a soft underlayer (SUL), the head potential distribution $\Psi(x, y, z)$ of the MR head is obtained by means of reciprocity calculations [3]:

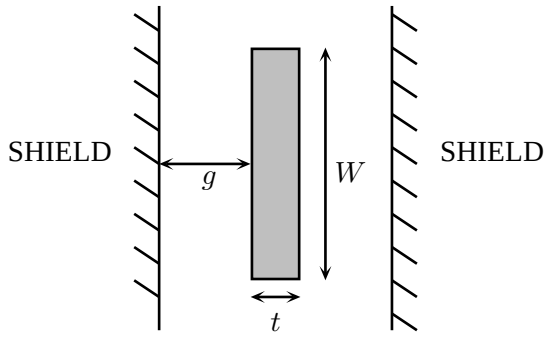

Figure 3.2 Top view of a shielded MR head.

$$
\begin{aligned}
\Psi(x,y,z) &= \left(\left\{ \frac{y}{4\pi g} log \left[\frac{R+(z-z')}{R-(z-z')} \right] + \frac{g+\frac{t}{2}+x}{2\pi g} \right. \right. \\
&\quad \left. \left. \cdot \quad \tan^{-1} \left[\frac{(z-z')(x-x')}{yR} \right] \right\} \Bigg|_{x'=-g-t/2}^{-t/2} \right. \\
&+ \quad \frac{1}{2\pi} \tan^{-1} \left[\frac{(z-z')(x-x')}{yR} \right] \Bigg|_{x'=-t/2}^{t/2} \\
&+ \quad \left\{ -\frac{y}{4\pi g} log \left[\frac{R+(z-z')}{R-(z-z')} \right] + \frac{g+\frac{t}{2}-x}{2\pi g} \right. \\
&\quad \left. \left. \cdot \quad \tan^{-1} \left[\frac{(z-z')(x-x')}{yR} \right] \right\} \Bigg|_{x'=t/2}^{t/2+g} \right) \Bigg|_{z'=-W/2}^{W/2}
\end{aligned} \tag{3.1}
$$

where $R = \sqrt{(x-x')^2 + y^2 + (z-z')^2}$.

At a flying height $y = 5$ nm, the surface plot of the head potential distribution of an MR head with dimensions $W = 35$ nm, $t = 5$ nm, and $g = 25$ nm is shown in Fig. 3.3. Note that the head potential distribution decreases with increasing distance in the down-track and cross-track directions.

In the presence of an SUL, the head potential distribution is obtained by means of reciprocity and multiple images calculations. For a given thickness of SUL ℓ, choose the smallest positive integer N such that for a given ϵ,

$$
|\Psi(x, 2(N+1)\ell + y, z) - \Psi(x, 2(N+1)\ell - y, z))| < \epsilon. \tag{3.2}
$$

The head potential distribution $\Psi_{\text{SUL}}(x,y,z)$, then, is

$$
\Psi_{\text{SUL}}(x,y,z) = \sum_{i=1}^{N} \Big(\Psi(x, 2i\ell + y, z) - \Psi(x, 2i\ell - y, z) \Big) + \Psi(x,y,z). \tag{3.3}
$$

The readback signal produced by a head centered at $(0,0)$ from an island centered at (x_0, z_0) is the integral of the head potential distribution over that island

$$
V(x_0, z_0) = \int_{x_0 - s_x/2}^{x_0 + s_x/2} \int_{z_0 - s_z/2}^{z_0 + s_z/2} \Big(\Psi(x,d,z) - \Psi(x, d+h, z) \Big) dx dz. \tag{3.4}
$$

Here, d represents the flying height of the MR head from the surface of the media. To obtain the readback signal in the presence of an SUL, the head potential distribution $\Psi(x,y,z)$ in (3.4) should be replaced with $\Psi_{\text{SUL}}(x,y,z)$ defined in (3.3).

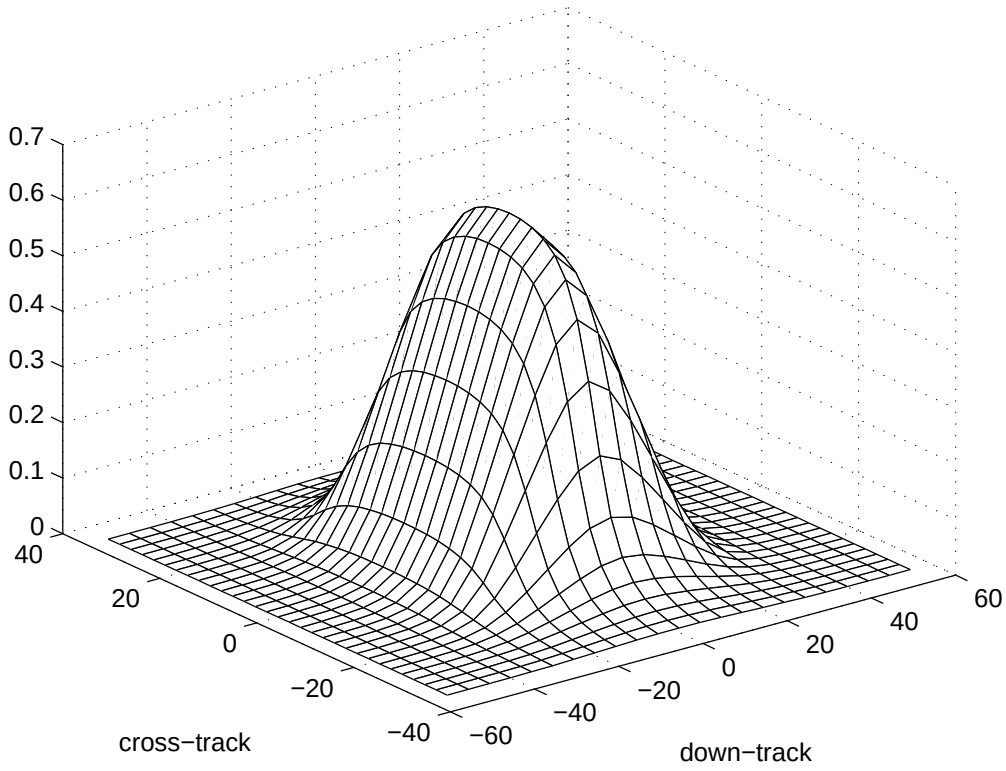

Figure 3.3 Surface plot of the head potential distribution versus down-track and cross-track distance for a shielded MR head.

For a recording density of 1 Tb/in^2 with the media configuration shown in Table 3.1, the normalized readback signals of isolated islands without SUL centered at $(0, 0)$ and $(0, B_z)$ versus down-track distance x are shown in Fig 3.4. This figure shows the change in the readback signal the head senses when the center of the head whose nominal position is $(0, 0)$ moves in the down-track direction. Fig. 3.5 shows the normalized readback signals versus down-track distance x in the presence of SUL. In the absence of SUL, a negative undershoot is observed whereas in the presence of SUL, such a negative undershoot is absent. It is also known that SUL helps the writing process by enhancing the recording field [4].

When the readback signal from the islands at distances of comparable to the island separation in the down-track direction is not negligible, intersymbol interference (ISI) is observed. Similarly, the readback signal from the islands in adjacent tracks introduces inter-track interference (ITI) into the model. For specific media configurations, the ITI level increases by

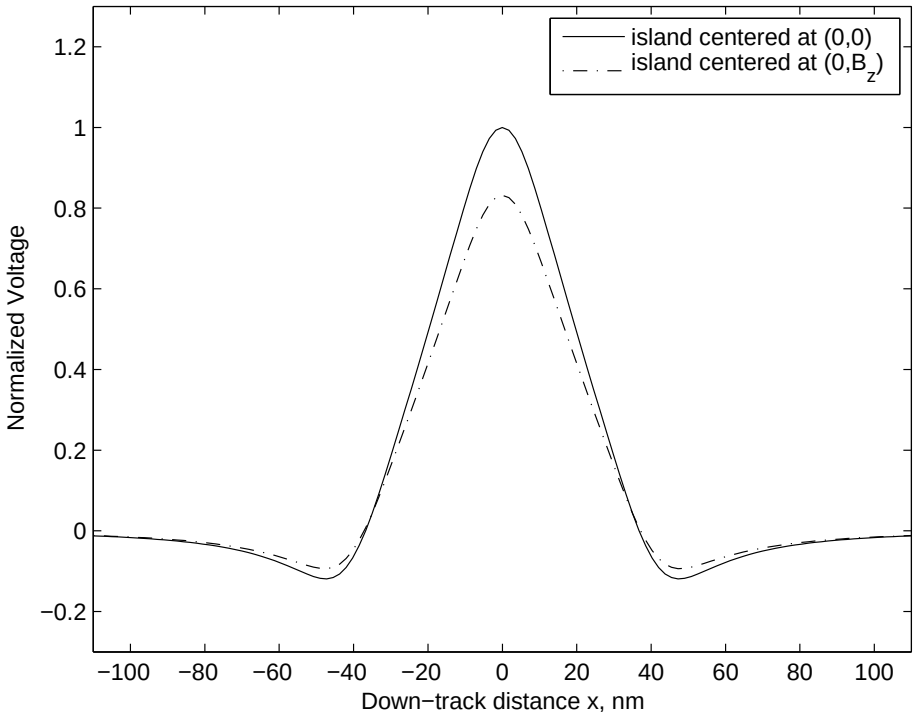

Figure 3.4 The normalized readback voltage from islands centered at $(0, 0)$ and $(0, B_z)$ in the absence of SUL.

increasing the width W of the head and the ISI level increases by increasing the gap g from the MR element to the shield. However, decreasing the island separations in the down-track and cross-track directions, respectively, increases the length and the level of ISI and ITI in the channel for a specific head configuration. Therefore, both head and media configurations determine the ISI and ITI levels in the channel.

3.4 Discrete-time Channel Model

When the head senses signals from m and n islands in the cross-track and down-track directions, respectively, the discrete-time readback model obtained by the sampling distance corresponding to the down-track island separation can be represented by an $m \times n$ channel response matrix. Without loss of generality, we focus on channel responses matrices where $m = 3$ and $n = 3$. The channel inputs are assumed to be independent identically distributed (i.i.d.) equiprobable binary sequences $\{u_{i,-1}\}$, $\{u_{i,0}\}$, and $\{u_{i,1}\}$ recorded on the upper, main,

and lower tracks, respectively and $u_{i,-1},\ u_{i,0},\ u_{i,1} \in \{1, -1\}$. If binary data is recorded on each track, the triplet of islands represents one of 8 possible recorded “symbols" listed in Table 3.2. That is, each symbol represents three independent bits stored on the upper, main, and lower track.

For certain recording densities, the noiseless sampled discrete-time readback model

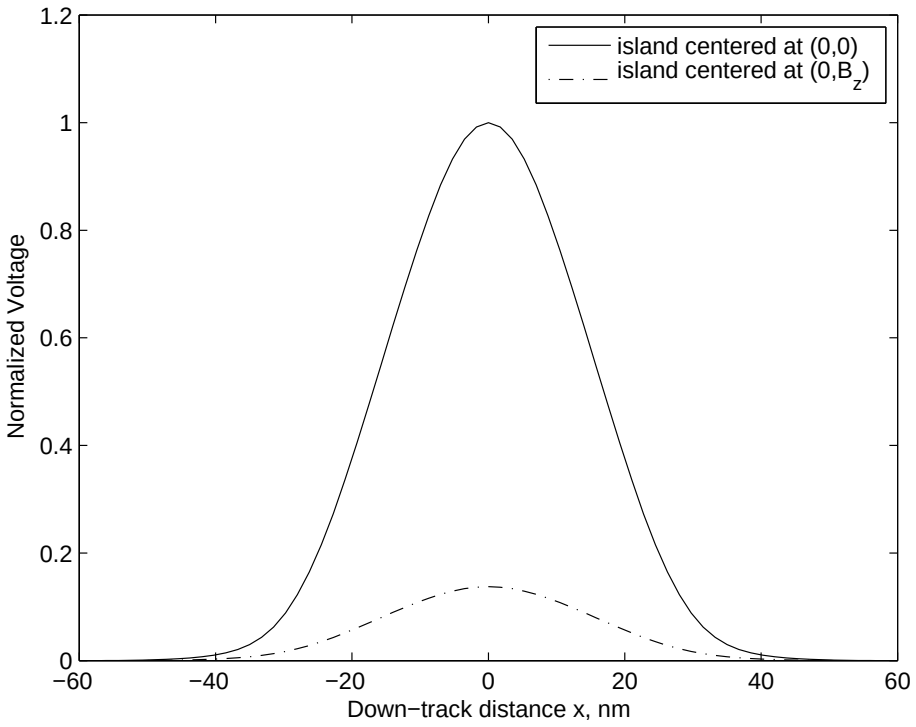

Figure 3.5 The normalized readback voltage from islands centered at $(0, 0)$ and $(0, B_z)$ with SUL.

Table 3.2 Symbols

upper track	$-$	$+$	$-$	$-$	$+$	$+$	$-$	$+$
main track	$-$	$-$	$+$	$-$	$+$	$-$	$+$	$+$
lower track	$-$	$-$	$-$	$+$	$-$	$+$	$+$	$+$

can be represented by a 3×3 channel response matrix H

$$H = \begin{pmatrix} h_{0,-1} & h_{1,-1} & h_{2,-1} \\ h_{0,0} & h_{1,0} & h_{2,0} \\ h_{0,1} & h_{1,1} & h_{2,1} \end{pmatrix} \tag{3.5}$$

where the ISI is limited to 2 symbols. Fig. 3.6 shows the discrete noiseless channel model where the noiseless readback signal v_i at time i is

$$v_i = \quad \sum_{k=0}^{2} h_{k,-1} u_{i-k,-1} + \sum_{k=0}^{2} h_{k,0} u_{i-k,0} + \sum_{k=0}^{2} h_{k,1} u_{i-k,1}.$$

3.5 Noise Modeling

In the read channel model, we consider AWGN and media noise. The replay transducer and the readback circuitry generate the stationary electronics noise. We model the samples of this noise source by independent, zero-mean Gaussian random variables $\{w_i\}$ with variance σ^2. In the presence of AWGN, the readback signal y_i at time i is

$$y_i = \quad \sum_{k=0}^{2} h_{k,-1} u_{i-k,-1} + \sum_{k=0}^{2} h_{k,0} u_{i-k,0} + \sum_{k=0}^{2} h_{k,1} u_{i-k,1} + w_i \ . \tag{3.6}$$

Fig. 3.7 illustrates the discrete-time readback model with AWGN.

The island size and island location fluctuations are expected to be the source of media noise in BPM recording channels [5]-[8]. Here, we assume that the dominant component of the media noise arises from the randomness of the island locations. This non-stationary component is referred to as “jitter noise." Let us assume that an island can be shifted from its ideal location both in the down-track and cross-track direction as shown in Fig. 3.8. We model these shifts

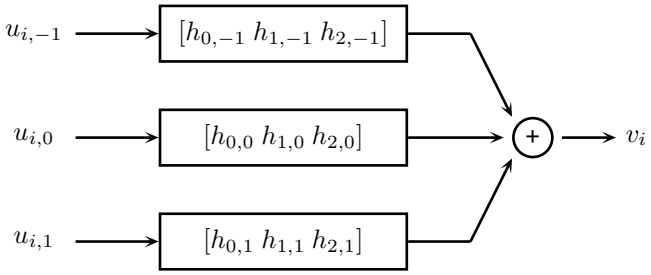

Figure 3.6 The discrete-time noiseless channel model.

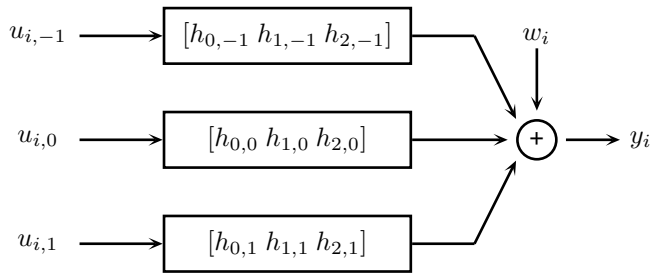

Figure 3.7 The discrete-time channel model with AWGN.

as independent, zero-mean Gaussian random variables δx and δz, with variances $\sigma^2_{\delta x}$ and $\sigma^2_{\delta z}$, respectively.

The jitter-induced readback voltage in a head centered at $(0, 0)$ from an island whose nominal position is (x, z) is defined as

$$v_{\mathrm{j}}(x, z) \stackrel{\mathrm{def}}{=} v(x + \delta x, z + \delta z) - v(x, z). \tag{3.7}$$

Fig. 3.9 shows that the numerically calculated probability density function $f_{V_{\mathrm{j}}}(v)$ of the jitter-induced readback voltage from an island with a nominal position $(0, 0)$ for the recording density of 1 Tb/in^2 and $\sigma_{\delta x} = \sigma_{\delta z} = 2.5$ nm. Note that the probability density function is not Gaussian.

The computational complexity of calculating an exact description of the probability density function $f_{V_{\mathrm{j}}}(v)$ is high. Therefore, we introduce a second-order approximation where we express the readback voltage induced in a head centered at $(0, 0)$ by an island centered at

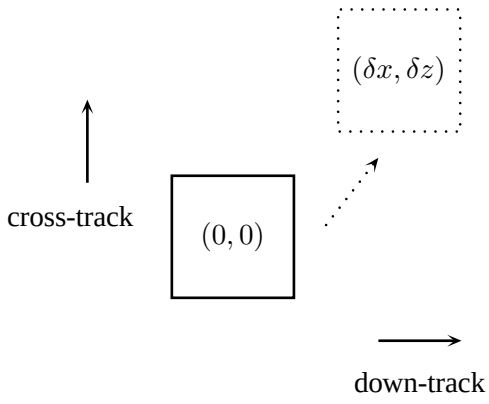

Figure 3.8 A shifted island in the down-track and cross-track directions with δx and δz, respectively.

$(x+\delta x, z+\delta z)$ using a Taylor series expansion

$$\begin{aligned} v(x+\delta x, z+\delta z) =& v(x,z) + \delta x\, v_x(x,z) + \delta z\, v_z(x,z) + \\ & \frac{1}{2}[(\delta x)^2\, v_{xx}(x,z) + 2\delta x\, \delta z\, v_{xz}(x,z) + (\delta z)^2 v_{zz}(x,z)] + \xi(x,z) \\ =& v(x,z) + \xi(x,z) + e(x,z). \end{aligned} \tag{3.8}$$

Here, $\xi(x,z)$ denotes the second-order approximation to the jitter-induced readback voltage

$$\begin{aligned} \xi(x,z) =& \delta x\, v_x(x,z) + \delta z\, v_z(x,z) + \\ & \frac{1}{2}[(\delta x)^2\, v_{xx}(x,z) + 2\delta x\, \delta z\, v_{xz}(x,z) + (\delta z)^2\, v_{zz}(x,z)] \end{aligned} \tag{3.9}$$

and $e(x,z)$ represents the modeling error due to approximating the shifted readback voltage with the first-order and second-order derivative terms. If a first-order approximation were utilized, the jitter-induced readback voltage would be approximated by a Gaussian function which contradicts the non-Gaussian nature of the jitter-induced readback voltage.

Fig. 3.10 shows the numerically calculated probability density function $f_\xi(v)$ of the second-order approximation to the jitter-induced readback voltage. It is seen that the probability density function of the second-order approximation and the actual probability density function of the jitter-induced readback voltage have the similar non-Gaussian form. Note also that the second-order approximation is computationally less complex since derivatives in (3.9) are computed only once. Fig 3.10 shows us that a higher order approximation for the jitter-induced readback voltage should be utilized to be able to capture the statistical properties of this noise source. We also note that this noise source is symbol dependent and it consists of contributions from adjacent islands in the presence of inter-island interference.

Acknowledgment

Portions of this chapter appear in the paper: S. Karakulak, P. H. Siegel, J. K. Wolf, and H. N. Bertram, "A new read channel model for patterned media storage," *IEEE Trans. Magn.*, vol. 44, pp. 193-197, Jan. 2008.

Bibliography

[1] G. F. Hughes, "Read channels for patterned media," *IEEE Trans. Magn.*, vol. 35, pp. 2310–2312, Sept. 1999.

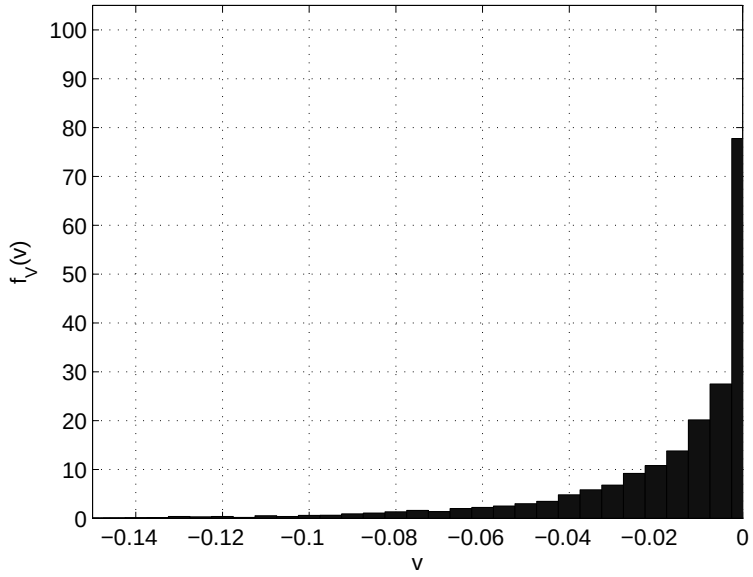

Figure 3.9 The probability density function of the jitter-induced readback voltage.

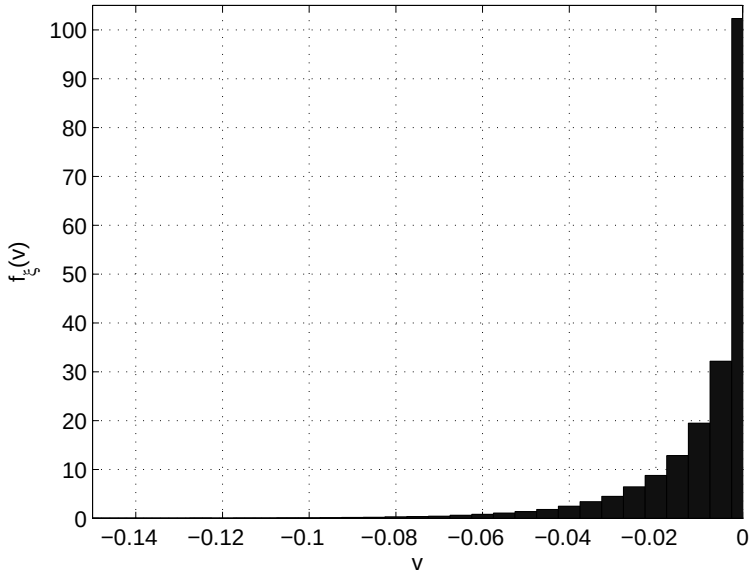

Figure 3.10 The probability density function of the second-order approximation to the jitter-induced readback voltage.

[2] P. W. Nutter, I. T. Ntokas, and B. K. Middleton, “An investigation of the effects of media characteristics on read channel performance for patterned media storage,” *IEEE Trans.*

Magn., vol. 41, pp. 4327–4334, Nov. 2005.

[3] S. W. Yuan and H. N. Bertram, "Off-track spacing loss of shielded MR heads," *IEEE Trans. Magn.*, vol. 30, pp. 1267–1273, May 1994. Correction to "Off-track spacing loss of shielded MR heads", *IEEE Trans. Magn.* vol. 32, pp. 3334, Jul. 1996.

[4] S. Khizroev, Y. Liu, K. Mountfield, M. H. Kryder, and D. Litvinov, "Physics of perpendicular magnetic recording: writing process," *Journal of Magnetism and Magnetic Materials*, vol. 246, pp. 335–344, 2002.

[5] M. M. Aziz, C. D. Wright, B. K. Middleton, H. Du, and P. W. Nutter, "Signal and noise characteristics of patterned media," *IEEE Trans. Magn.*, vol. 38, pp. 1964–1966, Sept. 2002.

[6] H. J. Richter, A. Y. Dobin, O. Heinonen, K. Z. Gao, R. J. M. v. d. Veerdonk, R. T. Lynch, J. Xue, D. Weller, P. Asselin, M. F. Erden, and R. M. Brockie, "Recording on bit-patterned media at densities of 1Tb/in^2 and beyond," *IEEE Trans. Magn.*, vol. 42, pp. 2255–2260, Oct. 2006.

[7] I. T. Ntokas, P. W. Nutter, C. J. Tjhai, and M. Z. Ahmed, "Improved data recovery from patterned media with inherent jitter noise using Low-Density Parity-Check codes," *IEEE Trans. Magn.*, vol. 43, pp. 3925–3929, Oct. 2007.

[8] P. W. Nutter, Y. Shi, B. D. Belle, and J. J. Miles, "Understanding sources of errors in bit-patterned media to improve read channel performance," *IEEE Trans. Magn.*, vol. 44, pp. 3797–3800, Nov. 2008.

Chapter 4

Equalization and Detection

4.1 Introduction

In this chapter, we study equalization and detection techniques for bit-patterned media (BPM) recording channels. The proposed BPM recording channel in Chapter 3 includes intersymbol interference (ISI) and inter-track interference (ITI) due to the high recording densities. Several detection and equalization methods have been proposed for channels with ITI. The performance of the read channel in the presence of additive white Gaussian noise (AWGN) was analyzed under maximum-likelihood (ML) symbol sequence detection in [1]. The complexity of an ML detector for the bit sequence written on the main track is substantial in the presence of ITI. In [2], a detector that utilizes ML symbol sequence detection and outputs the middle bit of each detected symbol in the ML symbol sequence was introduced. To reduce the detection complexity, in [3], a decision feedback equalizer (DFE) that uses the previously detected upper track data was proposed. In [4], ML symbol sequence detection with joint-track equalization was described. A maximum *a posteriori* (MAP) bit detector was derived in [5]. In [6], a one-dimensional (1-D) equalizer was designed where a partial-response (PR) target was chosen to match the channel response of the main track. For detection, the Viterbi algorithm was utilized on a modified trellis where the number of states corresponded to the PR target. The modified trellis was obtained by adding branches to take into account the ITI from immediately adjacent bits on the outer tracks.

In [7] and [8], a two-dimensional (2-D) generalized partial-response (GPR) equalizer that eliminates the ITI followed by a Viterbi detector was introduced. In [8], the use of iterative decision feedback detection (IDFD) was proposed. For IDFD or 2-D equalization, multiple

1-D waveforms were required as inputs rather than a single 1-D waveform as in the methods described above. These multiple 1-D waveforms might be obtained by reading multiple adjacent tracks or by utilizing multi-head read elements.

In Section 4.2, we first review the read channel model described in Chapter 3. In Section 4.3, we consider the trellis representation of channel input/output sequences. In Section 4.4, we study ML symbol sequence detection, ML bit sequence detection, and MAP bit detection. In Section 4.5, we review briefly several previously designed 1-D and 2-D equalizers. We adapt a joint-track equalizer introduced in [4] to BPM recording channels. In Section 4.6, we propose a scheme that utilizes the joint-track equalizer followed by a Viterbi detector. We compare the performance and the complexity of this scheme with schemes that utilize optimal bit detection or optimal symbol sequence detection, and the scheme introduced in [6]. The latter scheme consists of 1-D equalization with a PR target followed by the Viterbi algorithm that works on the modified trellis as described above.

4.2 Review of the Read Channel Model

In this section, we mainly concentrate on a read channel model with a 3×3 channel response matrix. The detection and equalization methods discussed in this chapter are general, however, and can be applied without loss of generality to any BPM channel model with different lengths of ISI and ITI.

In the read channel, we assume that the read head centered over the main track spans a specified fraction of the outer tracks (*upper track* and *lower track*, respectively). This was shown schematically in Fig. 3.1. The read channel response matrix is

$$H = \begin{pmatrix} h_{0,-1} & h_{1,-1} & h_{2,-1} \\ h_{0,0} & h_{1,0} & h_{2,0} \\ h_{0,1} & h_{1,1} & h_{2,1} \end{pmatrix} \tag{4.1}$$

where the first and third row vectors represent the channel responses of the upper and lower tracks, respectively, and the middle row vector represents the channel response of the main track. The channel inputs are assumed to be independent, identically distributed (i.i.d.), equiprobable binary sequences $\{u_{i,-1}\}$, $\{u_{i,0}\}$, and $\{u_{i,1}\}$, where $u_{i,-1}$, $u_{i,0}$, $u_{i,1} \in \{1, -1\}$. The noise samples $\{w_i\}$ are assumed to be independent, zero-mean Gaussian random variables with variance

σ^2. Then, the readback signal y_i at time i is

$$\begin{aligned} y_i &= \sum_{k=0}^{2} h_{k,-1} u_{i-k,-1} + \sum_{k=0}^{2} h_{k,0} u_{i-k,0} + \sum_{k=0}^{2} h_{k,1} u_{i-k,1} + w_i \\ &\stackrel{\text{def}}{=} v_i + w_i \end{aligned} \tag{4.2}$$

where v_i is the noiseless output signal. The read channel model was illustrated in Fig. 3.7.

As described in the previous section, the triplet of islands represents one of 8 possible recorded “symbols" which consist of three independent bits stored on the upper, main, and lower track.

4.3 Trellis Representation of Noiseless Channel Output Sequences

The channel given in (4.1) has a memory of 2 symbols. The input and output sequences of this channel can then be described by a trellis with $8^2 = 64$ states. Each state at time i is labeled with the symbols at time $i-2$ and $i-1$, respectively. From each state at time i, there are 8 outgoing branches to 8 different states at time $i+1$. The branches emanating from the state at time i are labeled by the input symbol at time i and the noiseless output v_i corresponding to this state transition. This is shown in Fig. 4.1.

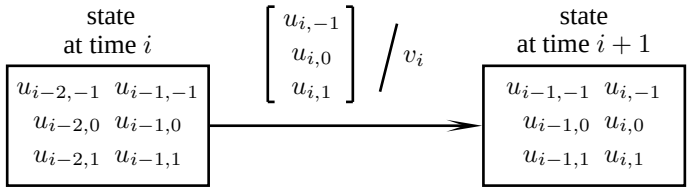

Figure 4.1 State and branch labeling for the channel response matrix H.

4.3.1 Channel Response with Cross-track Symmetry

When the channel response matrix has a cross-track symmetry such that $h_{0,-1} = h_{0,1}$, $h_{1,-1} = h_{1,1}$, and $h_{2,-1} = h_{2,1}$, the noiseless channel output sequences can be represented with a trellis that has $6^2 = 36$ states. For convenience, we define a channel response matrix H_c with

this cross-track symmetry as follows

$$H_c = \begin{pmatrix} m & p & n \\ r & q & t \\ m & p & n \end{pmatrix}. \tag{4.3}$$

For this channel, the noiseless channel output v_i at time i is

$$\begin{aligned} v_i &= n(u_{i-2,-1} + u_{i-2,1}) + p(u_{i-1,-1} + u_{i-1,1}) + m(u_{i,-1} + u_{i,1}) \\ &\quad + t(u_{i-2,0}) + q(u_{i-1,0}) + r(u_{i,0}). \end{aligned} \tag{4.4}$$

We label each state at time i with 4 quantities: the sum of the bits on the upper and lower track at time $i-2$, the sum of the bits on the upper and lower track at time $i-1$, the bit on the main track at time $i-2$, and the bit on the main track at time $i-1$. Each branch is labeled in a manner similar to the case of channel response H in (4.1). This is shown in Fig. 4.2.

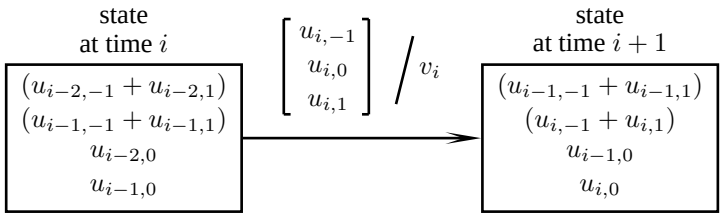

Figure 4.2 State and branch labeling for the channel response matrix H_c.

The sum of the bits written on the upper and lower track at time i takes 3 different values as follows

$$(u_{i,-1} + u_{i,1}) = \begin{cases} -2, & \text{if } u_{i,-1} = -1 \text{ and } u_{i,1} = -1 \\ 0, & \text{if } u_{i,-1} = -1 \text{ and } u_{i,1} = 1 \\ 0, & \text{if } u_{i,-1} = 1 \text{ and } u_{i,1} = -1 \\ +2, & \text{if } u_{i,-1} = 1 \text{ and } u_{i,1} = 1 \end{cases}. \tag{4.5}$$

Therefore, the trellis representing the noiseless channel output sequences has $(3 \times 3 \times 2 \times 2) = 6^2 = 36$ different states. If we denote the noiseless channel outputs at time i for the input $\{u_{i,-1} = 1,\ u_{i,1} = -1\}$ by $v_i^{(1)}$ and for the input $\{u_{i,-1} = -1,\ u_{i,1} = 1\}$ by $v_i^{(2)}$, we find that

$$\begin{aligned} v_i^{(1)} &= n(u_{i-2,-1} + u_{i-2,1}) + p(u_{i-1,-1} + u_{i-1,1}) + m(0) \\ &\quad + t(u_{i-2,0}) + q(u_{i-1,0}) + r(u_{i,0}) \end{aligned} \tag{4.6}$$

$$\begin{aligned} v_i^{(2)} &= n(u_{i-2,-1} + u_{i-2,1}) + p(u_{i-1,-1} + u_{i-1,1}) + m(0) \\ &\quad + t(u_{i-2,0}) + q(u_{i-1,0}) + r(u_{i,0}). \end{aligned} \tag{4.7}$$

It is seen from (4.6) and (4.7) that $v_i^{(1)}$ and $v_i^{(2)}$ are equal. There are two such pairs of inputs for which the noiseless channel outputs are the same, i.e., one pair when $u_{i,0} = -1$ and one pair when $u_{i,0} = 1$. Therefore, in this trellis structure, more than one input symbol sequence may generate the same output sequence. When using this trellis as the basis for symbol detection, we may have to use a restricted input symbol alphabet as shown in Section 4.4.1. Such a restricted input symbol alphabet introduces rate loss to the channel. Alternatively, we may use the reduced-state trellis for detection of the binary data on the main track only.

4.3.2 Channel Response with Cross-track Symmetry and Zero Corner Entries

If, in addition to the cross-track symmetry, the corner entries $h_{0,-1}$, $h_{0,1}$, $h_{2,-1}$, and $h_{2,1}$ are equal to zero, we can represent the noiseless channel output sequences with a 4-state trellis. For convenience, we define a channel response matrix H_+ having the cross-track symmetry and the corner entries equal to zero as follows

$$H_+ = \begin{pmatrix} 0 & p & 0 \\ r & q & t \\ 0 & p & 0 \end{pmatrix}. \tag{4.8}$$

For this channel, the noiseless channel output v_i at time i is

$$v_i = p(u_{i-1,-1} + u_{i-1,1}) + t(u_{i-2,0}) + q(u_{i-1,0}) + r(u_{i,0}).$$

Here, each state at time i is labeled with the bits written on the main track at time $i-2$ and $i-1$. Each branch has a label of the form a/b where a equals $[u_{i-1,-1}\ u_{i,0}\ u_{i-1,1}]$, namely the channel input bit on the upper track at time $i-1$, the channel input bit on the main track at time i, and the channel input bit on the lower track at time $i-1$, and b equals v_i, namely the noiseless channel output that corresponds to this state transition. This is shown in Fig. 4.3. There are 8 branches emanating from each state forming 4 parallel branches between each pair of connected states.

If we denote the noiseless channel outputs at time i for the input $\{u_{i-1,-1} = 1,\ u_{i-1,1} = -1\}$ by $v_i^{(3)}$ and for the input $\{u_{i-1,-1} = -1,\ u_{i-1,1} = 1\}$ by $v_i^{(4)}$, we find that

$$v_i^{(3)} = p(0) + t(u_{i-2,0}) + q(u_{i-1,0}) + r(u_{i,0}) \tag{4.9}$$

$$v_i^{(4)} \quad = \quad p(0) + t(u_{i-2,0}) + q(u_{i-1,0}) + r(u_{i,0}). \tag{4.10}$$

It is seen from (4.9) and (4.10) that $v_i^{(3)}$ and $v_i^{(4)}$ are equal. Therefore, two of the 4 parallel branches between each pair of connected states have the same output labels. This trellis is shown in Fig. 4.4. For convenience, the branch labels are not included in the figure. This 4-state trellis was introduced by Nabavi et al. [6] where two of the 4 parallel branches between each connected pair of states that have the same output labels were combined into one branch, resulting in 3 parallel branches between each pair of connected states. In this trellis structure, similar to the case of channel response H_c, more than one input symbol sequence may generate the same output sequence. Hence, the discussion in Section 4.3.1 on symbol versus bit detection applies here, too.

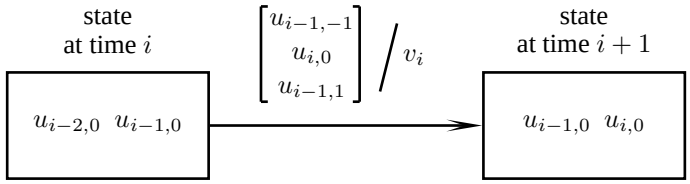

Figure 4.3 State and branch labeling for the channel response matrix H_+.

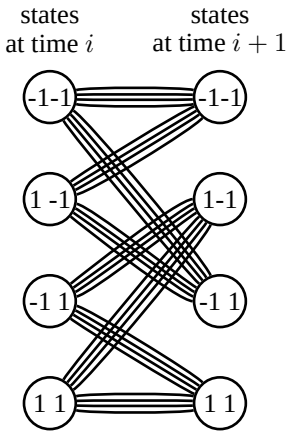

Figure 4.4 Trellis diagram for the channel response matrix H_+.

4.4 Detection

In this section, we study different detection methods including ML symbol sequence detection, ML bit sequence detection, and MAP bit detection. The ML symbol sequence detector minimizes the probability that a symbol sequence is in error, whereas the ML bit sequence detector minimizes the probability that a bit sequence is in error. Both detectors are based on Viterbi algorithm. On the other hand, the MAP bit detector is optimum in the sense of minimizing the probability of a bit error.

4.4.1 ML Symbol Sequence Detection

The ML symbol sequence can be obtained by utilizing the Viterbi algorithm that is matched to the trellis representing the channel input and noiseless channel output sequences. The ML symbol sequence is the sequence that maximizes $p(\underline{y}|\underline{u}_{-1}, \underline{u}_0, \underline{u}_1)$, i.e.,

$$\underline{\hat{u}}_{-1}, \underline{\hat{u}}_0, \underline{\hat{u}}_1 \quad = \quad \arg \max_{\underline{u}_{-1}, \underline{u}_0, \underline{u}_1} p(\underline{y}|\underline{u}_{-1}, \underline{u}_0, \underline{u}_1)$$

where $\underline{y}$ represents the detector input samples, $\underline{u}_{-1}, \underline{u}_0, \underline{u}_1$ represent the bit sequences recorded on the upper, main, and lower tracks, respectively. When the channel has cross-track symmetry, since more than one input symbol sequence may generate the same output sequence, there may be more than one ML symbol sequence. To resolve such a detection tie, one might choose to utilize a restricted input alphabet. Consider channel H_c defined in (4.3). When the parameters $p = q$, $m = r$, and $n = t$, we obtain the channel $\widehat{H}_c$

$$\widehat{H}_c = \begin{pmatrix} r & q & t \\ r & q & t \\ r & q & t \end{pmatrix}. \tag{4.11}$$

For this channel, the symbols with the same number of $+$ and $-$ bits are indistinguishable. Therefore, the restricted input alphabet, shown in Table 4.1, has 4 elements which results in a rate of $2/3$ bits per island. We define a channel $\widetilde{H}_c$ where the parameters $p = q/2$, $m = r/2$, and $n = t/2$ in (4.3)

$$\widetilde{H}_c = \begin{pmatrix} r/2 & q/2 & t/2 \\ r & q & t \\ r/2 & q/2 & t/2 \end{pmatrix}. \tag{4.12}$$

For channel $\widetilde{H}_c$, there are 5 elements in the restricted input alphabet since the symbols $\{[-,+,+], [+,+,-]\}$, $\{[-,-,+],[+,-,-]\}$, and $\{[-,+,-],[+,-,+]\}$ are indistinguishable. Table 4.2 shows an example of a restricted input alphabet for channel $\widetilde{H}_c$ with rate $\log_2(5)/3$ bits per island. For channel H_c defined in (4.3), the restricted input alphabet has at most 6 elements as shown in Table 4.3. Therefore, the rate of such a channel is at most $\log_2(6)/3$ bits per island.

Table 4.1 Restricted symbol alphabet for $\widehat{H}_c$.

upper track	$-$	$+$	$+$	$+$
main track	$-$	$-$	$+$	$+$
lower track	$-$	$-$	$-$	$+$

Table 4.2 Restricted symbol alphabet for $\widetilde{H}_c$.

upper track	$-$	$+$	$+$	$+$	$+$
main track	$-$	$-$	$+$	$-$	$+$
lower track	$-$	$-$	$-$	$+$	$+$

Table 4.3 Restricted symbol alphabet with six elements.

upper track	$-$	$+$	$-$	$+$	$+$	$+$
main track	$-$	$-$	$+$	$+$	$-$	$+$
lower track	$-$	$-$	$-$	$-$	$+$	$+$

4.4.2 ML Bit Sequence Detection

The ML bit sequence written on the main track is the sequence $\underline{\hat{u}}_0$ that maximizes $P(\underline{y}|\underline{u}_0)$, i.e.,

$$\begin{aligned}
\underline{\hat{u}}_0 &= \arg\max_{\underline{u}_0} p(\underline{y}|\underline{u}_0) \\
&= \arg\max_{\underline{u}_0} \Big[\sum_{\underline{u}_{-1}}\sum_{\underline{u}_1} p(\underline{y},\ \underline{u}_{-1},\ \underline{u}_1|\underline{u}_0)\Big] \\
&= \arg\max_{\underline{u}_0} \Big[\sum_{\underline{u}_{-1}}\sum_{\underline{u}_1} p(\underline{y}|\underline{u}_0,\ \underline{u}_{-1},\ \underline{u}_1)P(\underline{u}_{-1},\ \underline{u}_1)\Big] \qquad (4.13)
\end{aligned}$$

where $\underline{y}$ represents the detector input samples and $P(\underline{u}_{-1},\ \underline{u}_1)$ represents the joint *a priori* probability of the bit sequences $\underline{u}_{-1}$ and $\underline{u}_1$. Since the sequences $\underline{u}_{-1}$ and $\underline{u}_1$ are i.i.d. equiprobable,

$$\hat{\underline{u}}_0 \quad = \quad \arg \max_{\underline{u}_0} \Big[\sum_{\underline{u}_{-1}} \sum_{\underline{u}_1} p(\underline{y}|\underline{u}_0,\ \underline{u}_{-1},\ \underline{u}_1) \Big]. \tag{4.14}$$

The complexity involved in the maximization of $p(\underline{y}|\underline{u}_0)$ is proportional to the number of distinct pairs $(\underline{u}_{-1},\ \underline{u}_1)$. Therefore, it is substantial. As stated in [4], if at a high signal-to-noise ratio (SNR), the conditional densities involved in (5.7) are dominated by one particular pair $(\underline{u}_{-1},\ \underline{u}_1)$, the following approximation can be made

$$\begin{aligned} &\max_{\underline{u}_0} \Big[\sum_{\underline{u}_{-1}} \sum_{\underline{u}_1} p(\underline{y}|\underline{u}_0,\ \underline{u}_{-1},\ \underline{u}_1) \Big] \\ &\qquad \approx \max\nolimits_{\underline{u}_0,\ \underline{u}_{-1},\ \underline{u}_1} \ p(\underline{y}|\underline{u}_0,\ \underline{u}_{-1},\ \underline{u}_1). \end{aligned} \tag{4.15}$$

The right hand side of (5.8) corresponds to joint ML sequence detection for $\underline{u}_{-1}$, $\underline{u}_0$, and $\underline{u}_1$, i.e. ML symbol sequence detection. Thus, a detection scheme, based on the Viterbi algorithm, that outputs the middle bit of each detected symbol in the ML symbol sequence can be viewed as a high SNR approximation for ML bit sequence detection. For channels with a cross-track symmetry, the ML symbol sequence detector works on the 36-state trellis described in the previous section.

Viterbi Algorithm with a Modified Branch Metric

When the channel response matrix is equal to H_+ as defined in (4.8), the ML bit sequence can be obtained using the Viterbi algorithm with a modified branch metric on a 4-state trellis with 4 parallel branches between each connected pair of states as shown in Fig. 4.4.

Each branch is labeled by the channel input bit on the upper track at time $i-1$, the channel input bit on the main track at time i, the channel input bit on the lower track at time $i-1$, and the noiseless channel output v_i. This is shown in Fig. 4.3. We represent each state at time i with s_i where

$$s_i \stackrel{\text{def}}{=} (u_{i-2,0},\ u_{i-1,0}). \tag{4.16}$$

Let N denote the length of the input bit sequence $\underline{u}_0$. We assume that the initial and final states s_0 and s_N are known. There is a one-to-one correspondence between state sequences $\underline{s} = \{s_0,\ s_1,\ \ldots,\ s_N\}$ and input bit sequences $\underline{u}_0 = \{u_{0,0},\ \ldots,\ u_{N-1,0}\}$ written on the main track. Therefore, the ML bit sequence detector finds the state sequence $\hat{\underline{s}}$ that maximizes $p(\underline{y}|\underline{s})$,

i.e.,

$$\begin{aligned}\hat{\underline{s}} &= \arg \max_{\underline{s}} p(\underline{y}|\underline{s}) \\ &= \arg \max_{\underline{s}} \prod_{i=0}^{N-1} p(y_i|s_i,\ s_{i+1}). \end{aligned} \tag{4.17}$$

Define

$$\lambda(s_i,\ s_{i+1}) \stackrel{\text{def}}{=} -\ln p(y_i|s_i,\ s_{i+1}). \tag{4.18}$$

Maximizing $p(\underline{y}|\underline{s})$ is the same as minimizing $-\ln p(\underline{y}|\underline{s})$ and the latter can be expressed as

$$-\ln p(\underline{y}|\underline{s}) = \sum_{i=0}^{N-1} \lambda(s_i,\ s_{i+1}). \tag{4.19}$$

The detector can be implemented using the Viterbi algorithm with a modified branch metric equal to $\lambda(s_i,\ s_{i+1})$. We can express $\lambda(s_i,\ s_{i+1})$ as follows

$$\lambda(s_i,\ s_{i+1}) = -\ln p(y_i|s_i,\ s_{i+1}) \tag{4.20}$$

$$= -\ln \Big[\sum_{u_{i-1,-1}} \sum_{u_{i-1,1}} p(y_i,\ u_{i-1,-1},\ u_{i-1,1}|s_i,\ s_{i+1}) \Big] \tag{4.21}$$

$$\begin{aligned} = -\ln \Big[& p(y_i|s_i,\ s_{i+1},\ u_{i-1,-1}=-1,\ u_{i-1,1}=-1) \\ & \cdot P(u_{i-1,-1}=-1,\ u_{i-1,1}=-1) + \\ & + p(y_i|s_i,\ s_{i+1},\ u_{i-1,-1}=-1,\ u_{i-1,1}=1) \\ & \cdot P(u_{i-1,-1}=-1,\ u_{i-1,1}=1) \\ & + p(y_i|s_i,\ s_{i+1},\ u_{i-1,-1}=1,\ u_{i-1,1}=-1) \\ & \cdot P(u_{i-1,-1}=1,\ u_{i-1,1}=-1) \\ & + p(y_i|s_i,\ s_{i+1},\ u_{i-1,-1}=1,\ u_{i-1,1}=1) \\ & \cdot P(u_{i-1,-1}=1,\ u_{i-1,1}=1) \Big]. \end{aligned} \tag{4.22}$$

The detection algorithm based upon (4.22) can be thought of in terms of the Viterbi algorithm operating on a 4-state trellis where a single branch replaces the 4 parallel branches between connected states. The branch metric for this single branch is given by (4.22). This detector is an ML detector for the bit sequence written on the middle track.

Another detector which operates on a 4-state trellis which has 3 parallel branches between connected states was described in [6]. As stated in [6], that detector first finds the best

branch out of the parallel branches between connected states. The two detectors are not the same in that there are situations where for a given noisy output sequence they will choose different input sequences. Since our detector is an ML detector, it follows that the detector described in [6] is not truly an ML detector.

4.4.3 MAP Bit Detection

The MAP bit detector outputs the estimated bit $\hat{u}_{i,0}$ on the main track at time i

$$\hat{u}_{i,0} = \arg \max_{\tau \in \{-1,+1\}} P(u_{i,0} = \tau | \underline{y}) \tag{4.23}$$

given the channel output sequence $\underline{y}$. For MAP bit detection, the *a posteriori* probability (APP) for each bit at time i, $P(u_{i,0} = \tau|\underline{y})$ $\tau \in \{-1, +1\}$, can be calculated by a modification to the Bahl-Cocke-Jelinek-Raviv (BCJR) algorithm which outputs the APP for each symbol at time i [9]. This modification was derived in [5].

The modified BCJR algorithm outputs

$$P(u_{i,0} = -1|\underline{y}) = \sum_{\phi \in U_i^{-1}} P(\underline{u}_i = \phi|\underline{y}) \tag{4.24}$$

and

$$P(u_{i,0} = 1|\underline{y}) = \sum_{\phi \in U_i^{+1}} P(\underline{u}_i = \phi|\underline{y}). \tag{4.25}$$

Here, $\underline{u}_i$ denotes the symbol at time i, U_i^{-1} and U_i^{+1} denote the set of symbols ϕ at time i where $u_{i,0}$ equals -1 and 1, respectively.

The BCJR algorithm operates on the trellis representing the channel input and noiseless channel output sequences. It recursively computes the forward state metrics and the backward state metrics, which are combined with the branch metrics to produce the APP of each symbol $P(\underline{u}_i = \phi|\underline{y})$. The APP of the symbol $\underline{u}_i = \phi$, i.e. the conditional probability of the symbol $\underline{u}_i = \phi$ given the channel output $\underline{y}$, can be written as

$$P(\underline{u}_i = \phi|\underline{y}) = P(\underline{u}_i = \phi,\ \underline{y})/P(\underline{y}) \tag{4.26}$$

$$= \frac{1}{P(\underline{y})} \sum_{k=0}^{M-1} \sum_{j=0}^{M-1} P(\underline{u}_i = \phi,\ s_{i-1} = k,\ s_i = j,\ \underline{y}). \tag{4.27}$$

Here, s_i represents the state at time i and M represents the number of states in the trellis.

The forward state metric and the backward state metric for state j at time i and the branch metric from state k at time $i-1$ to state j at time i with the input symbol ϕ, respectively, are defined as

$$\alpha_i(j) = P(s_i = j,\ \underline{y}_0^i), \tag{4.28}$$

$$\beta_i(j) = P(\underline{y}_{i+1}^{N-1} | s_i = j), \tag{4.29}$$

and

$$\gamma_i^{\phi}(k,j) = P(\underline{u}_i = \phi,\ s_i = j,\ y_i | s_{i-1} = k) \tag{4.30}$$

where $\underline{y}_i^{i'}$ denotes the sequence $\{y_i, y_{i+1}, \cdots, y_{i'}\}$. In terms of the forward state metrics, the backward state metrics, and the branch metrics, the APP of each symbol can be expressed as

$$P(\underline{u}_i = \phi | \underline{y}) = \frac{1}{P(\underline{y})} \sum_{k=0}^{M-1} \sum_{j=0}^{M-1} \alpha_{i-1}(k) \gamma_i^{\phi}(k,j) \beta_i(j). \tag{4.31}$$

The forward state metrics and the backward state metrics are obtained by means of forward recursion and backward recursion with the initial conditions $\alpha_0(0) = 1$, $\alpha_0(j) = 0$ for $j \neq 0$ and terminal conditions $\beta_{N-1}(0) = 1$, $\beta_{N-1}(j) = 0$ for $j \neq 0$.

Forward recursion

$$\alpha_i(j) = P(s_i = j,\ \underline{y}_0^i) \tag{4.32}$$

$$\stackrel{(1)}{=} \sum_{k=0}^{M} P(s_{i-1} = k,\ s_i = j,\ \underline{y}_0^{i-1}, y_i) \tag{4.33}$$

$$\stackrel{(2)}{=} \sum_{k=0}^{M} P(s_i = j,\ y_i | s_{i-1} = k,\ \underline{y}_0^{i-1}) P(s_{i-1} = k,\ \underline{y}_0^{i-1}) \tag{4.34}$$

$$\stackrel{(3)}{=} \sum_{k=0}^{M} P(s_i = j,\ y_i | s_{i-1} = k) P(s_{i-1} = k,\ \underline{y}_0^{i-1}) \tag{4.35}$$

$$= \sum_{k=0}^{M} P(s_i = j,\ y_i | s_{i-1} = k) \alpha_{i-1}(k) \tag{4.36}$$

$$\stackrel{(4)}{=} \sum_{k=0}^{M} \alpha_{i-1}(k) \sum_{\phi \in \Phi} P(\underline{u}_i = \phi,\ s_i = j,\ y_i | s_{i-1} = k) \tag{4.37}$$

$$= \sum_{k=0}^{M} \alpha_{i-1}(k) \sum_{\phi \in \Phi} \gamma_i^{\phi}(k,j) \tag{4.38}$$

Backward recursion

$$\beta_i(j) = P(\underline{y}_{i+1}^{N-1}|s_i = j) \tag{4.39}$$

$$\overset{(1')}{=} \sum_{j'=0}^{M} P(s_{i+1} = j',\ \underline{y}_{i+1}^{N-1}|s_i = j) \tag{4.40}$$

$$= \sum_{j'=0}^{M} P(s_{i+1} = j',\ y_{i+1},\ \underline{y}_{i+2}^{N-1}|s_i = j) \tag{4.41}$$

$$\overset{(2')}{=} \sum_{j'=0}^{M} P(\underline{y}_{i+2}^{N-1}|s_i = j,\ s_{i+1} = j',\ y_{i+1}) P(s_{i+1} = j',\ y_{i+1}|s_i = j) \tag{4.42}$$

$$\overset{(3')}{=} \sum_{j'=0}^{M} P(\underline{y}_{i+2}^{N-1}|s_{i+1} = j') P(s_{i+1} = j',\ y_{i+1}|s_i = j) \tag{4.43}$$

$$\overset{(4')}{=} \sum_{j'=0}^{M} \beta_{i+1}(j') \sum_{\phi \in \Phi} P(\underline{u}_i = \alpha,\ s_{i+1} = j',\ y_{i+1}|s_i = j) \tag{4.44}$$

$$= \sum_{j'=0}^{M} \beta_{i+1}(j') \sum_{\phi \in \Phi} \gamma_{i+1}^{\alpha}(j, j') \tag{4.45}$$

The equalities in (1), $(1')$, (4), and $(4')$ follow from the principle of total probability whereas equalities (2) and $(2')$ follow from Bayes' Rule. Since the conditional probability of being in a state at time i and the output y_i given the state at time $i-1$ and the channel outputs $\underline{y}_0^{i-1}$ only depends on the state at time $i-1$ due to the Markov property, the equalities in (3) and $(3')$ follow.

4.5 Equalization

In this section, we review several previously designed equalizers for BPM recording channels. We later adapt the use of a joint-track equalizer, introduced in [4] in the context of single-head/single-track detection for perpendicular recording channels, to BPM recording channels.

4.5.1 Related Equalization Techniques

In [10], 1-D *minimum mean-square error* (MMSE) finite impulse response (FIR) equalizers were discussed for BPM recording channels. A block diagram of this 1-D equalization, where the ITI was treated as noise, is shown in Fig. 4.5. The channel response can be

equalized to a desired target, $g(D)$, using an FIR filter, $f(D)$. Define $\varepsilon_i = z_i - d_i$ to be the difference between the equalized channel sample z_i and the desired target sample d_i at time i. The 1-D equalizer with FIR $f(D)$ minimizes the mean-square error (MSE), $E\{\varepsilon_i^2\}$. If a target $g(D)$ has not been specified, the FIR filter $f(D)$ and the target $g(D)$ are found simultaneously [11]. A 1-D MMSE FIR equalizer was also used in [6] where the FIR target was chosen to match the ISI of the main track.

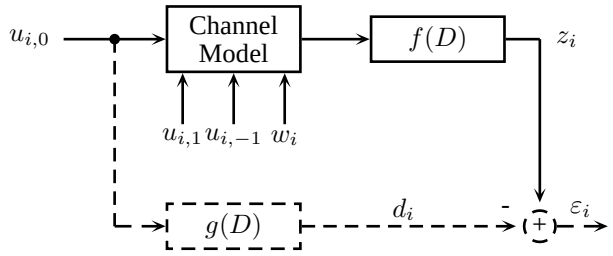

Figure 4.5 1-D MMSE equalizer design with FIR $f(D)$ and with a 1-D target $g(D)$ for BPM recording channels.

Two-dimensional (2-D) equalization techniques have been used to shape 2-D channels such as those used to model holographic storage systems. The use of a 2-D GPR equalizer was proposed for BPM recording channels in [7] and [8]. Since this study is constrained to single track detection with single 1-D waveform obtained by a single read head, we only briefly review this 2-D equalization method that requires multiple 1-D waveforms as inputs.

In [7] and [8], the inputs to the 2-D equalizer were multiple 1-D waveforms which were obtained by reading multiple adjacent tracks. A monic constraint on the target response of the main track was imposed as well as an additional constraint that forces the ITI to zero. This method offered performance improvement compared to the 1-D equalization techniques described above. In [8], a simplified 2-D equalization technique produced the same results as in [7].

4.5.2 Joint-track Equalization

In this study, we adapt the joint-track equalization technique introduced in [4] to BPM recording channels. The joint-track equalization technique consists of a 1-D equalizer shown in Fig. 4.6(a). This 1-D equalizer not only equalizes the main track to a 1-D target but also equalizes all three tracks to a 2-D target as shown in Fig. 4.6(b). In contrast, the previously designed 1-D equalizers described in [10] and [6] only equalize the main track to a 1-D target.

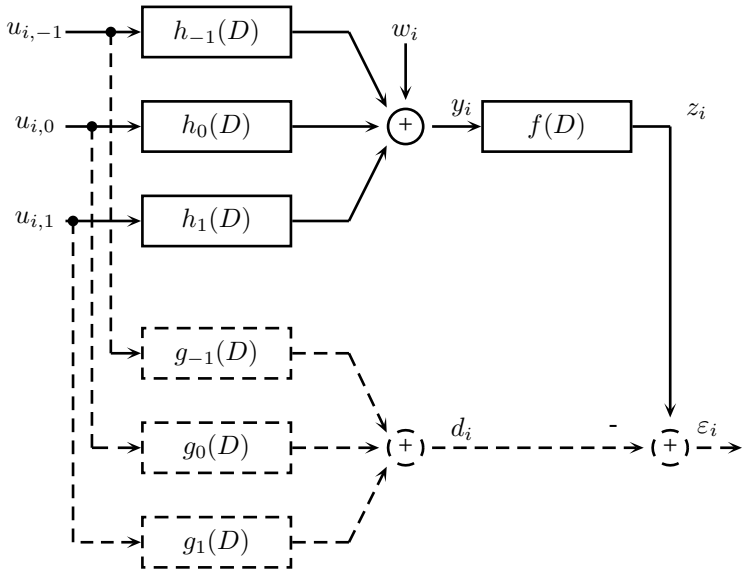

(a)

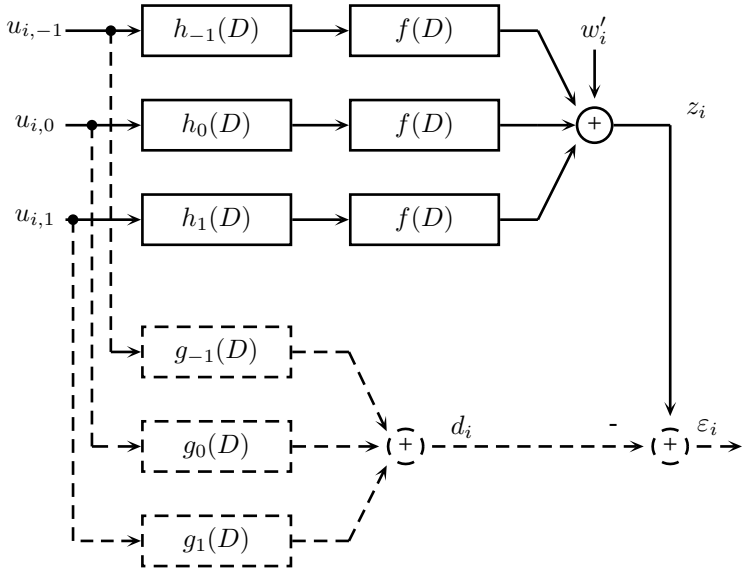

(b)

Figure 4.6 (a) Block diagram for joint-track equalizer design. (b) Equivalent block diagram where w_i' represents the colored noise sample after equalization.

In the joint-track equalization process, we design an MMSE equalizer with FIR $f(D) =$

$\sum_{k=-\ell}^{\ell} f_k D^k$ using an adaptation of the method in [11] but with a 3×3 target response G

$$G = \begin{pmatrix} g_{0,-1} & g_{1,-1} & g_{2,-1} \\ g_{0,0} & g_{1,0} & g_{2,0} \\ g_{0,1} & g_{1,1} & g_{2,1} \end{pmatrix}. \tag{4.46}$$

Let

$$g_{-1}(D) = \sum_{k=0}^{2} g_{k,-1} D^k, \tag{4.47}$$

$$g_0(D) = \sum_{k=0}^{2} g_{k,0} D^k, \tag{4.48}$$

and

$$g_1(D) = \sum_{k=0}^{2} g_{k,1} D^k \tag{4.49}$$

where $g_{-1}(D)$, $g_0(D)$, and $g_1(D)$ represent the targets for the upper, main, and lower track, respectively.

In [12], for a perpendicular magnetic recording channel with two interfering tracks, a joint-track equalizer with a monic constraint for the track to be detected was used. In contrast to the derivation in [12], by representing the 2-D data sequence and the 2-D target polynomial coefficients by vectors, the 2-D target design problem can be converted into a 1-D form. This method was used previously in [13], [7], and [8]. The joint-track equalizer can be obtained by setting the number of read heads to 1 and modifying the constraint matrix to incorporate the constraints on the target G in the equalization design of [7] and [8].

4.6 Simulation Results

In this section, we compare the performance and the complexity of several different schemes for recording densities of 1 Tb/in^2, 1.2 Tb/in^2, 1.4 Tb/in^2, 1.7 Tb/in^2, 1.75 Tb/in^2, and 2 Tb/in^2. We utilize a medium employing an SUL [1] with the media configurations shown in Table 4.4. For a recording density of 1 Tb/in^2, the extent of ISI is limited to 2 symbols. For higher recording densities, the extent of ISI becomes 4 symbols due to the decreasing island separation in the down-track direction.

4.6.1 Recording Density of 1Tb/in^2

For a recording density of 1 Tb/in^2, we utilize two different channel responses H_1 and H_2. Channel H_1 corresponds to the case with no SUL [6] whereas channel H_2 represents the case with an SUL [1]

$$H_1 = \begin{pmatrix} -0.023 & 0.264 & -0.023 \\ -0.087 & 1 & -0.087 \\ -0.023 & 0.264 & -0.023 \end{pmatrix} \tag{4.50}$$

$$H_2 = \begin{pmatrix} 0.0347 & 0.2297 & 0.0347 \\ 0.1277 & 1 & 0.1277 \\ 0.0347 & 0.2297 & 0.0347 \end{pmatrix}. \tag{4.51}$$

The negative entries in (4.50) are due to the absence of no SUL.

For channels H_1 and H_2, we compare five different schemes. The first scheme utilizes an optimal bit detector, i.e., a MAP bit detector. This scheme uses a reduced-state trellis with 36 states and 8 outgoing branches per state as described Section 4.2. The second scheme was introduced by Nabavi et al. [6]. Their scheme consists of a 1-D MMSE FIR equalizer with a PR target that closely matches the channel response of the main track. They represented their detector with a modified trellis that has 4 states with 3 parallel branches between each pair of connected states. Note that for the modified trellis, only the ITI from immediately adjacent bits is taken into account. The Viterbi algorithm with the squared-Euclidean metric is utilized to detect the symbol sequence. Since the detection of only the main track sequence is considered, the detected bits belonging to the outer tracks, obtained from the survivor branch among the parallel branches, are discarded. For channels H_1 and H_2, PR targets $[-0.,\ 1,\ -0.1]$ and $[0.1,\ 1,\ 0.1]$ are chosen, respectively.

Table 4.4 Media configurations

Recording density	s_x	s_z	B_x	B_z
1 Tb/in^2	12.5 nm	12.5 nm	25 nm	25 nm
1.2 Tb/in^2	11 nm	12.5 nm	21.5 nm	25 nm
1.4 Tb/in^2	9 nm	12.5 nm	18.4 nm	25 nm
1.75 Tb/in^2	7 nm	12.5 nm	14.7 nm	25 nm
2 Tb/in^2	6 nm	12.5 nm	12.9 nm	25 nm

Simulation results for these two schemes are shown in Fig. 4.7 and in Fig. 4.8. The numerical results for the second scheme were taken from [6] for channel H_1. The SNR is defined as follows

$$\text{SNR} = 10\log_{10}\left(\frac{V_p^2}{\sigma^2}\right) \tag{4.52}$$

where V_p is the peak value of the readback signal of an isolated island and σ^2 is the variance of the noise. Here, $V_p = 1$.

It can be seen from Fig. 4.7 and Fig. 4.8 that at a target bit error rate of 10^{-4}, for channels H_1 and H_2, the scheme that utilizes optimal bit detection provides gains of 1.5 dB and 0.6 dB as compared to the scheme that utilizes 1-D equalization with the specified PR targets, respectively. For channels H_1 and H_2, simulation results not shown here indicate that the scheme that utilizes an ML symbol sequence detector and outputs the middle bit of each detected symbol gives similar bit error rates compared to the scheme utilizing optimal bit detection.

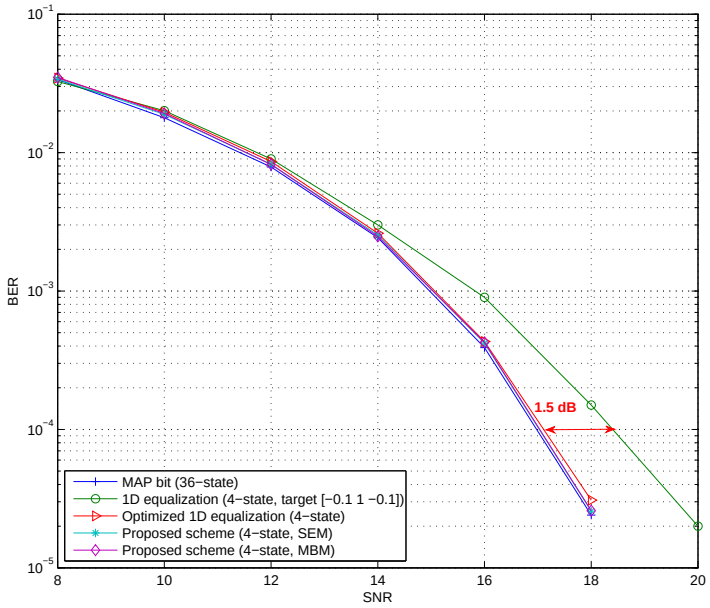

Figure 4.7 Simulation results for channel H_1 (no SUL, 1 Tb/in^2).

We propose another scheme that utilizes joint-track equalization technique described in Section 4.5.2. For certain head and media configurations, the contribution of the corner entries to the readback signal is close to zero. Therefore, our target is a 3×3 matrix G defined in (4.46) with the corner entries $g_{0,-1}$, $g_{0,1}$, $g_{2,-1}$, and $g_{2,1}$ set equal to zero and the middle entry $g_{1,0}$ set

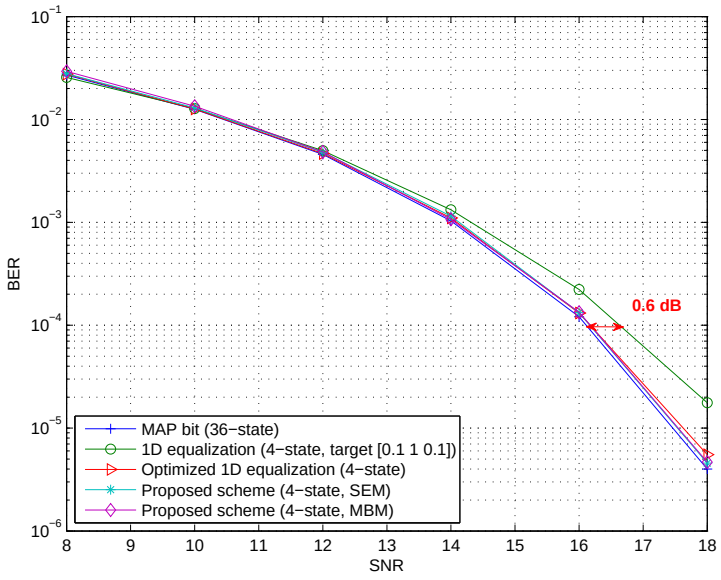

Figure 4.8 Simulation results for channel H_2 (SUL, 1 Tb/in^2).

equal to 1. The detector trellis has 4 states with 4 parallel branches between each connected pair of states as shown in Section 4.4.2. We use the Viterbi algorithm with the squared-Euclidean metric to detect the symbol sequence. The detector then outputs the middle bit of each detected symbol in this sequence. Since the equalizer colors the electronics noise, this detector is no longer ML. We also utilize the Viterbi algorithm with the modified branch metric defined by (4.22). This detector also does not output the ML bit sequence due to the noise coloration. Note that the difference between the proposed scheme with the squared-Euclidean metric and the scheme described in [6] is the equalization methods utilized. However, both schemes have the same detection method.

We also consider the scheme in [6] with optimized 1-D equalizer/target coefficients. For this, different target choices are utilized. Simulation results show that the scheme in [6] has the best performance when 1-D equalizer and target coefficients are obtained simultaneously in the MSE minimization process.

In all equalized systems, the FIR filters are limited to 11 taps. Simulation results indicate that the proposed scheme with the squared-Euclidean metric or with the modified branch metric give virtually the same results. For the performance curves, we utilize the acronyms SEM and MBM for the squared-Euclidean metric and the modified branch metric, respectively. Note

that computation of the modified branch metric is more complicated than computation of the squared-Euclidean metric. Simulation results in Fig. 4.7 and Fig. 4.8 show that the proposed scheme with joint-track equalization and the scheme with optimized 1-D equalizer/target coefficients essentially have the same performance as the scheme utilizing optimal bit detection.

4.6.2 Higher Recording Densities

For recording densities of 1.2 Tb/in^2, 1.4 Tb/in^2, 1.75 Tb/in^2, and 2 Tb/in^2, we have the following channel responses, respectively,

$$H_3 = \begin{pmatrix} 0 & 0.0572 & 0.2295 & 0.0572 & 0 \\ 0.003 & 0.2232 & 1 & 0.2232 & 0.003 \\ 0 & 0.0572 & 0.2295 & 0.0572 & 0 \end{pmatrix}, \tag{4.53}$$

$$H_4 = \begin{pmatrix} 0.0035 & 0.0835 & 0.2294 & 0.0835 & 0.0035 \\ 0.01 & 0.3393 & 1 & 0.3393 & 0.01 \\ 0.0035 & 0.0835 & 0.2294 & 0.0835 & 0.0035 \end{pmatrix}, \tag{4.54}$$

$$H_5 = \begin{pmatrix} 0.0136 & 0.1211 & 0.2293 & 0.1211 & 0.0136 \\ 0.0426 & 0.5080 & 1 & 0.5080 & 0.0426 \\ 0.0136 & 0.1211 & 0.2293 & 0.1211 & 0.0136 \end{pmatrix}, \tag{4.55}$$

and

$$H_6 = \begin{pmatrix} 0.0257 & 0.1402 & 0.2292 & 0.1402 & 0.0257 \\ 0.0886 & 0.5937 & 1 & 0.5937 & 0.0886 \\ 0.0257 & 0.1402 & 0.2292 & 0.1402 & 0.0257 \end{pmatrix}. \tag{4.56}$$

These channels have memory of 4 symbols, so the schemes that utilize optimal bit detection or ML symbol sequence detection require only a reduced-state trellis with $6^4 = 36^2$ states. The computational complexity for optimal bit detection is very high. Therefore, we utilize only the ML symbol sequence detector that outputs the middle bit of each detected symbol. Note that this scheme can be viewed as a high SNR approximation for ML bit sequence detection as discussed in Section 4.4.2.

In all equalized systems, the target length is limited to 3. For channel H_3, we choose a PR target $[0.2,\ 1,\ 0.2]$ that closely matches the channel response of the main track. In channels H_4, H_5, and H_6, in addition to the ITI from immediately adjacent bits on the outer tracks, the ITI from other bits is also significant. The performance curves not shown here indicate that the scheme using 1-D equalization with a PR target has poor performance for channels H_4, H_5, and H_6.

Simulation results for channel H_3 are shown in Fig. 4.9. It is seen that the scheme that utilizes ML symbol sequence detection offers 1.8 dB gain compared to the scheme that utilizes 1-D equalization with the PR target $[0.2,\ 1,\ 0.2]$. Simulation results also show that the proposed scheme with joint-track equalization and the scheme with optimized 1-D equalizer/target coefficients have the same performance as the scheme utilizing ML symbol sequence detection.

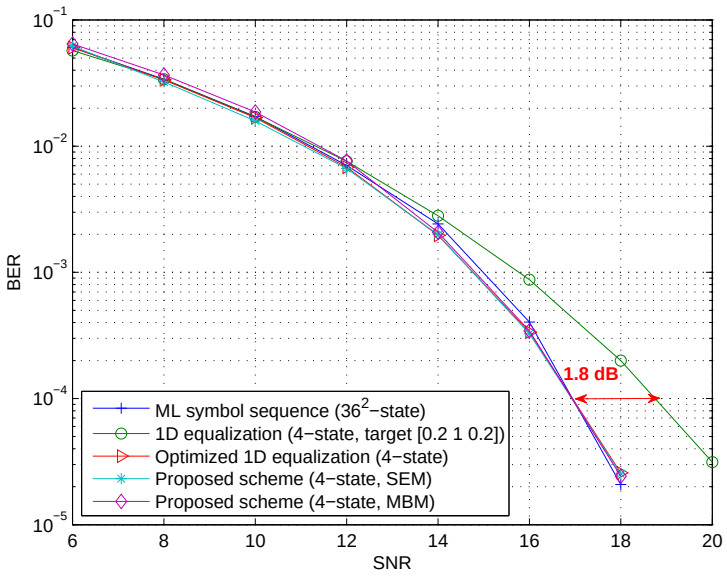

Figure 4.9 Simulation results for channel H_3 (SUL, 1.2 Tb/in^2).

Simulation results are shown in Fig. 4.10, Fig. 4.11, and Fig. 4.12 for channels H_4, H_5, and H_6, respectively. For channels H_4 and H_5, the scheme that utilizes ML symbol sequence detection offers 0.5 dB and 5 dB gain as compared to the proposed scheme with joint-track equalization at a target bit error rate of 10^{-4}. For channels H_5 and H_6, the proposed scheme with joint-track equalization performs poorly as compared to the scheme that utilizes ML symbol sequence detection. This is due to severe noise coloration. This suggests choosing targets, such

as a longer target, which introduce less noise coloration or a noise whitening process before detection.

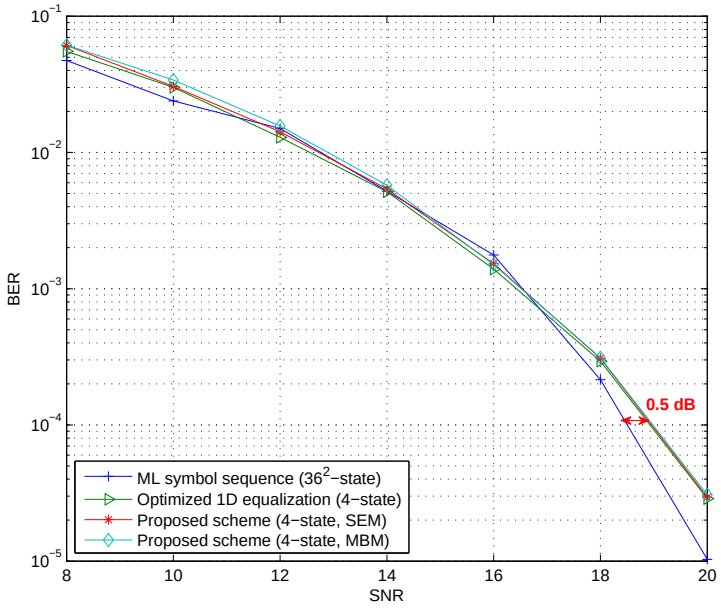

Figure 4.10 Simulation results for channel H_4 (SUL, 1.4 Tb/in^2).

Simulation results show that for the channels considered above, the proposed scheme with joint-track equalization does not provide any gain compared to the scheme with optimized 1-D equalizer/target coefficients. We observe that the channels considered above have similar levels of ITI. Therefore, we study channels which have higher levels of ITI compared to the channels above. For this, consider channels H_7 and H_8

$$H_7 = \begin{pmatrix} 0.0037 & 0.1232 & 0.3813 & 0.1232 & 0.0037 \\ 0.0079 & 0.3133 & 1 & 0.3133 & 0.0079 \\ 0.0037 & 0.1232 & 0.3813 & 0.1232 & 0.0037 \end{pmatrix} \tag{4.57}$$

$$H_8 = \begin{pmatrix} 0.0038 & 0.1322 & 0.4118 & 0.1322 & 0.0038 \\ 0.0079 & 0.3135 & 1 & 0.3135 & 0.0079 \\ 0.0038 & 0.1322 & 0.4118 & 0.1322 & 0.0038 \end{pmatrix}. \tag{4.58}$$

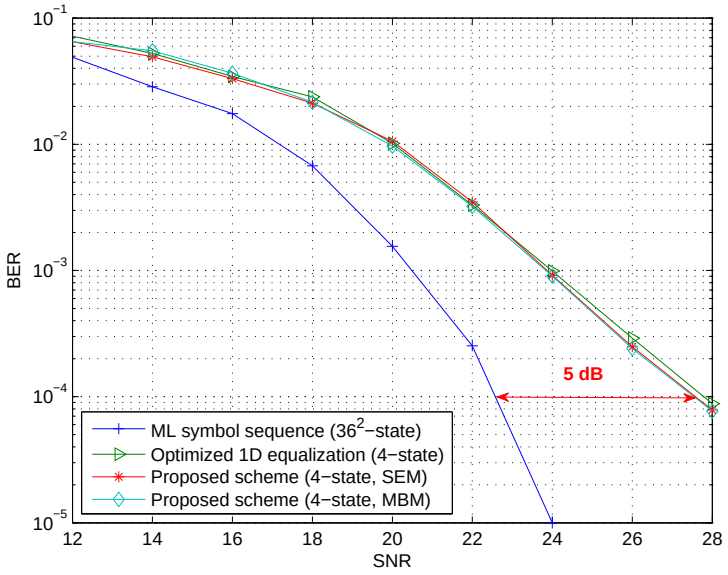

Figure 4.11 Simulation results for channel H_5 (SUL, 1.75 Tb/in^2).

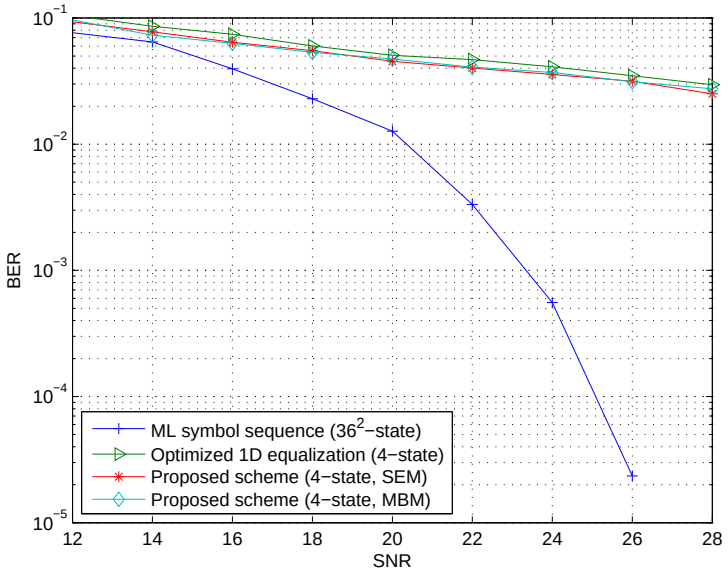

Figure 4.12 Simulation results for channel H_6 (SUL, 2 Tb/in^2).

Channels H_7 and H_8 are obtained for the media configurations where $s_x = 9$ nm, $s_z = 11$ nm, $B_x = 19$ nm, and $B_z = 22$ nm corresponding to 1.7 Tb/in^2. The MR head with the same parameters considered above is utilized for channel H_7 whereas only the width of the MR element is raised to 41 nm from 40 nm to obtain channel H_8.

For channel H_7, BER curves in Fig. 4.13 show that there is performance difference which is 0.6 dB at a target BER 10^{-5} between the proposed scheme with joint-track equalization and the scheme with optimized 1-D equalizer/target coefficients. However, for channel H_8, the proposed scheme with joint-track equalization outperforms the scheme with optimized 1-D equalizer/target coefficients with 1.8 dB at a target BER 10^{-4} as shown in Fig. 4.14 . Note also that the scheme that outputs the middle bit sequence in the ML symbol sequence outperforms the proposed scheme with joint-track equalization with close to 3.7 dB difference at a target BER 10^{-5} and BER 10^{-4} for channels H_7 and H_8, respectively. This is an expected result since equalization introduces noise coloration which is not taken into account in the detection process.

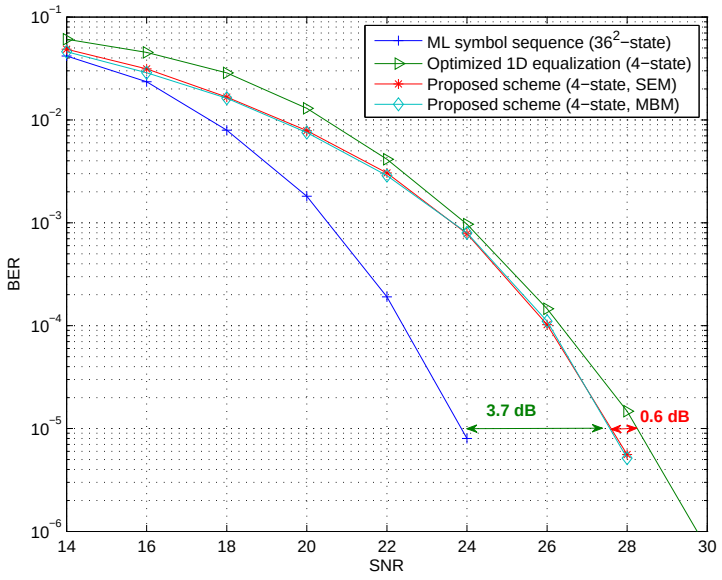

Figure 4.13 Simulation results for channel H_7 (SUL, 1.7 Tb/in^2).

Note that 2-D equalization techniques that eliminate the ITI as described in [7] and [8] would offer performance improvement compared to the schemes as described above. Nevertheless, as inputs, multiple 1-D waveforms rather than a single 1-D waveform are required for 2-D equalization.

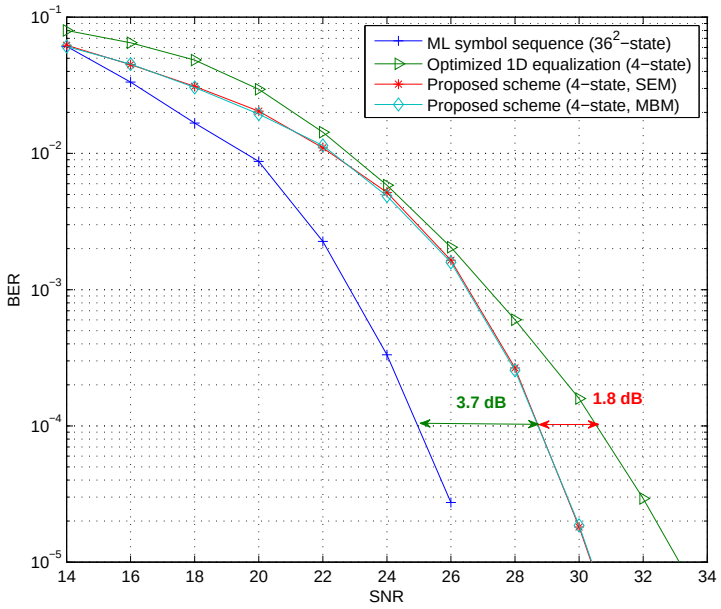

Figure 4.14 Simulation results for channel H_8 (SUL, 1.7 Tb/in^2).

4.6.3 Computational Complexity

Here, we compare the detection complexity of the schemes discussed above. The branch metric computations for the modified BCJR algorithm are more complex than the branch metric computations for the Viterbi algorithm. Therefore, the computational complexity of the scheme that utilizes the modified BCJR algorithm for optimal bit detection is substantially higher than the scheme that utilizes the Viterbi algorithm if both schemes work on the same trellis. For the recording density of 1 Tb/in^2, the scheme that utilizes optimal bit detection and the scheme that utilizes ML symbol sequence detection that outputs the middle bit in each detected symbol work on the same 36-state trellis. Hence, the latter scheme has less computational complexity.

The schemes that utilize a fixed PR target or optimized 1-D equalizer/target coefficients and the proposed scheme with joint-track equalization and the squared-Euclidean metric work on a 4-state trellis. It is seen that these schemes have the same total number of branches between all connected pairs of states when the branches between each connected pair of states that have the same noiseless channel outputs are merged. In these schemes, one comparison is made to select one branch that has the largest branch metric among parallel branches between each pair of connected states. The branch metric of the selected branch is added to the metric of

the state from which the selected branch stems. Then, among the paths starting at different states, the path with the largest accumulated metric is selected for every state. Note that the proposed scheme with joint-track equalization and the squared-Euclidean metric and the schemes that utilize a fixed PR target or optimized 1-D equalizer/target coefficients require the same number of arithmetic operations. Therefore these schemes have the same computational complexity.

The scheme that utilizes ML symbol sequence detection that outputs the middle bit in each detected symbol works on the 36-state trellis or on the 36^2-state trellis depending on the recording density. This scheme requires a substantially higher number of arithmetic operations compared to the schemes that utilize a 4-state trellis, namely the proposed scheme with joint-track equalization and the schemes that utilize a fixed PR target or optimized 1-D equalizer/target coefficients. Thus, the scheme that utilizes ML symbol sequence detection that outputs the middle bit in each detected symbol has higher computational complexity compared to the proposed scheme with joint-track equalization and the schemes that utilize a fixed PR target or optimized 1-D equalizer/target coefficients.

The proposed scheme with joint-track equalization and the modified branch metric also works on a 4-state trellis. Note that the proposed scheme with joint-track equalization and the modified branch metric has a smaller number of branches between all pairs of connected states than the proposed scheme with joint-track equalization and the squared-Euclidean metric and the schemes that utilize a fixed PR target or optimized 1-D equalizer/target coefficients. However, the proposed scheme with joint-track equalization and the modified branch metric requires more arithmetic operations for the total number of branch metric calculations. Overall, it has higher computational complexity compared to the proposed scheme with joint-track equalization and the squared-Euclidean metric and the schemes that utilize a fixed PR target or with optimized 1-D equalizer/target coefficients.

4.7 Conclusion

We considered a joint-track equalization procedure and compared several different detection and equalization methods for bit patterned media (BPM) recording channels. For the special case of a symmetric channel response matrix, we presented a maximum-likelihood (ML) bit sequence detector using the Viterbi algorithm with the modified branch metric. We proposed a scheme that utilizes the joint-track equalization technique followed by the Viterbi detector. The proposed scheme with a 3×3 target choice where the corner entries set equal to zero and

the middle entry set equal to 1 outperforms the scheme of the same complexity that utilizes one-dimensional (1-D) equalization with a fixed partial-response (PR) target [6]. Furthermore, the performance of the proposed scheme with joint-track equalization and the scheme with optimized 1-D equalizer/target coefficients is comparable to that of the much more complex schemes utilizing optimal bit detection or optimal symbol sequence detection for recording densities of 1 Tb/in^2 and 1.2 Tb/in^2. However, the proposed scheme with joint-track equalization performs significantly better compared to the scheme with optimized 1-D equalizer/target coefficients in the presence of high level of inter-track interference (ITI). With increasing recording densities, the performance gap between the scheme that utilizes optimal symbol sequence detection and the schemes with equalization increases due to the noise coloration after equalization. Therefore, a noise whitening process or targets that introduce less noise coloration before detection are required.

Acknowledgment

Portions of this chapter appear in the papers: S. Karakulak, P. H. Siegel, J. K. Wolf, and H. N. Bertram, "A new read channel model for patterned media storage," *IEEE Trans. Magn.*, vol. 44, pp. 193-197, Jan. 2008, S. Karakulak, P. H. Siegel, J. K. Wolf, and H. N. Bertram, "Equalization and detection in patterned media recording," *Intermag Dig. of Tech. Papers*, p. HT10, May 2008, and S. Karakulak, P. H. Siegel, J. K. Wolf, and H. N. Bertram, "Joint-track equalization and detection in patterned media recording," submitted to *IEEE Trans. Magn.*, 2008.

Bibliography

[1] S. Karakulak, P. H. Siegel, J. K. Wolf, and H. N. Bertram, "A new read channel model for patterned media storage," *IEEE Trans. Magn.*, vol. 44, no. 1, pp. 193–197, Jan. 2008.

[2] H. Burkhardt, "Optimal data retrieval for high density storage," *Proc. CompEuro '89., VLSI and Computer Peripherals. VLSI and Microelectronic Applications in Intelligent Peripherals and their Interconnection Networks*, pp. 43–48, May 1989.

[3] J. F. Heanue, K. Gurkan, and L. Hesselink, "Signal detection for page-access optical memories with intersymbol interference," *Applied Optics*, pp. 2341–2348, May 1996.

[4] B. G. Roh, S. U. Lee, J. Moon, and Y. Chen, "Single-head/single-track detection in interfering tracks," *IEEE Trans. Magn.*, vol. 38, no. 4, pp. 1830–1838, Jul. 2002.

[5] W. Tan and J. R. Cruz, “Evaluation of detection algorithms for perpendicular recording channels with inter-track interference,” *Journal of Magnetism and Magnetic Materials*, vol. 287, pp. 397–404, 2005.

[6] S. Nabavi, B. V. K. V. Kumar, and J.-G. Zhu, “Modifying Viterbi algorithm to mitigate inter-track interference in bit-patterned media,” *IEEE Trans. Magn.*, vol. 43, no. 6, pp. 2274–2276, Jun. 2007.

[7] S. Nabavi and B. V. K. V. Kumar, “Two-dimensional generalized partial response equalizer for bit-patterned media,” *Proc. IEEE International Conf. on Communications (ICC’07)*, pp. 6249–6254, Jun. 2007.

[8] M. Keskinoz, “Two-dimensional equalization/detection for patterned media storage,” *IEEE Trans. Magn.*, vol. 44, no. 4, pp. 533–539, Apr. 2008.

[9] L. Bahl, J. Cocke, F. Jelinek, and J. Raviv, “Optimal decoding of linear codes for minimizing symbol error rate,” *IEEE Trans. Inform. Theory*, vol. IT-20, pp. 284–287, Mar. 1974.

[10] P. W. Nutter, I. T. Ntokas, and B. K. Middleton, “An investigation of the effects of media characteristics on read channel performance for patterned media storage,” *IEEE Trans. Magn.*, vol. 41, no. 11, pp. 4327–4334, Nov. 2005.

[11] J. Moon and W. Zeng, “Equalization for maximum likelihood detectors,” *IEEE Trans. Magn.*, vol. 31, no. 2, pp. 1083–1088, Mar. 1995.

[12] W. Tan and J. R. Cruz, “Signal processing for perpendicular recording channels with inter-track interference,” *IEEE Trans. Magn.*, vol. 41, no. 2, pp. 730–735, Feb. 2005.

[13] L. Huang, G. Mathew, and T. C. Chong, “Channel modeling and target design for two-dimensional optical storage systems,” *IEEE Trans. Magn.*, vol. 41, no. 8, pp. 2414–2424, Aug. 2005.

Chapter 5

A Parametric Study of Inter-Track Interference in Bit Patterned Media Recording

5.1 Introduction

Decreasing island separation in the cross-track direction to increase the recording density introduces higher levels of inter-track interference (ITI) to the bit patterned media (BPM) recording channels. In this chapter, we present a parametric study of ITI for BPM recording channels. We choose a parametric form of a channel response matrix for a range of relevant head and media configurations discussed in Chapter 3. We first review the read channel model in Section 5.2. In Section 5.3, for channels both with and without intersymbol interference (ISI), we show bit error rate (BER) curves obtained by performance simulation of an optimal bit detector as a function of ITI level at specific values of signal-to-noise ratio (SNR). The performance results indicate that a higher level of ITI does not necessarily degrade the BER in a certain range of ITI. In fact, for a pair of channels with the same ISI level, we demonstrate that the channel with the higher level of ITI can perform better than the channel with the lower level of ITI over a large range of SNR values. Such a phenomenon is also observed in the presence of read head offset or track misregistration (TMR).

In Section 5.5, we provide insight into this somewhat surprising phenomenon. We first examine in Section 5.5.1 the BER for optimal bit detection as a function of ITI level in the absence of ISI. We determine the exact analytical expression for the BER as a function of ITI,

and we use this to explain the observed characteristics of the simulated BER curve.

In Section 5.5.2, we consider channels with ISI. Noting that the performance of the optimal bit detector is virtually identical to that of a joint-track maximum-likelihood (ML) sequence detector with respect to the main track sequence, we apply error event analysis techniques to the latter in order to understand the observed effects of ITI on system performance.

5.2 Review of the Read Channel Model

In this study, we consider a read channel model with a square array of islands. We represent the noiseless sampled discrete-time readback model by a 3×3 channel response matrix H with a cross-track symmetry [1]

$$H = \begin{pmatrix} ab & b & ab \\ a & 1 & a \\ ab & b & ab \end{pmatrix}. \tag{5.1}$$

In the channel response matrix H, the first, the second, and the third row vectors represent the response to the islands in the upper, main, and lower tracks, respectively. The parameter a denotes the ISI level and the parameter b denotes the ITI level in the channel. This parametric form of the channel response matrix H was found to be reasonable for a range of relevant head and media configurations. Of course, another parametric model might be more appropriate for significantly different head geometries and patterned island configurations.

A schematic of the sampled read channel model is shown in Fig. 3.7. The channel inputs recorded on the upper, main, and lower tracks at time index i, denoted by $\{u_{i,-1}\}$, $\{u_{i,0}\}$, and $\{u_{i,1}\}$, respectively, are mutually independent and, on each track, the recorded bits are assumed to be independent, equiprobable binary values over the alphabet $\{1, -1\}$. There are 8 different equiprobable symbols which represent the bits recorded on the upper, main, and lower tracks at time index i. Electronics noise is assumed to corrupt the output of the read head. We model the noise terms $\{w_i\}$ as samples of independent, zero-mean Gaussian random variables with variance σ^2. Then, the readback signal y_i at time index i is

$$\begin{aligned} y_i = {} & abu_{i,-1} + bu_{i-1,-1} + abu_{i-2,-1} \\ & + au_{i,0} + u_{i-1,0} + au_{i-2,0} \\ & + abu_{i,1} + bu_{i-1,1} + abu_{i-2,1} + w_i. \end{aligned} \tag{5.2}$$

The SNR is defined as

$$\text{SNR} = 10\log_{10}(\frac{1}{\sigma^2}). \tag{5.3}$$

5.2.1 Detection Techniques

In general, a BPM recording channel represented by a 3×3 channel response matrix has memory equal to 2 symbols, so the noiseless channel input-output relationship can be represented by a trellis using $8^2 = 64$ states, each with 8 outgoing branches. However, the particular matrix H in (5.1) has cross-track symmetry, which allows us to describe the channel with a smaller trellis having only $6^2 = 36$ states as shown in Section 4.3.2. This simplified trellis representation can offer reduced detection complexity.

We will make reference to three algorithms used to detect the data recorded on the main track: a maximum *a posteriori* (MAP) bit detector, a maximum-likelihood (ML) bit sequence detector, and a punctured ML symbol sequence detector that outputs the middle bit of each detected symbol in the ML symbol sequence [2]. Although we have presented these algorithms in Section 4.4 in detail, for completeness, we review them here.

The MAP bit detector is optimal, and it provides the MAP estimate of each bit on the main track. The detection algorithm is based upon the Bahl-Cocke-Jelinek-Raviv (BCJR) algorithm, details of which can be found in [3]. For this setting, the BCJR algorithm is easily adapted to produce joint-track or symbol MAP estimates based upon the *a posteriori* probability (APP) for each recorded symbol value. A straightforward extension of the results in [4], where only a single interfering track was considered, shows that the APP for a value of the bit on the main track is obtained simply by summing the APPs of the symbols sharing the specified middle bit value.

More precisely, if $u_{i,0}$ represents a recorded bit on the main track at time index i and $\underline{y}$ represents the detector input samples, the optimal bit detector outputs

$$P[u_{i,0} = -1|\underline{y}] = \sum_{U_i^{-1}} P[u_{i,-1}, u_{i,0}, u_{i,1}|\underline{y}] \tag{5.4}$$

$$P[u_{i,0} = 1|\underline{y}] = \sum_{U_i^{1}} P[u_{i,-1}, u_{i,0}, u_{i,1}|\underline{y}] \tag{5.5}$$

where U_i^{-1} and U_i^1 are the sets of symbols at time index i where $u_{i,0}$ equals -1 and 1, respectively.

As described in [5], the ML bit sequence for the main track is the sequence $\underline{\hat{u}}_0$ that

maximizes $p(\underline{y}|\underline{u}_0)$, i.e.,

$$\begin{aligned}\hat{\underline{u}}_0 &= \arg \max_{\underline{u}_0} \; p(\underline{y}|\underline{u}_0) \\ &= \arg \max_{\underline{u}_0} \; \Big[\sum_{\underline{u}_{-1}} \sum_{\underline{u}_1} p(\underline{y},\ \underline{u}_{-1},\ \underline{u}_1|\underline{u}_0)\Big] \\ &= \arg \max_{\underline{u}_0} \; \Big[\sum_{\underline{u}_{-1}} \sum_{\underline{u}_1} p(\underline{y}|\underline{u}_0,\ \underline{u}_{-1},\ \underline{u}_1) \\ &\qquad\qquad \cdot P(\underline{u}_{-1},\ \underline{u}_1)\Big] \end{aligned} \tag{5.6}$$

where $\underline{y}$ represents the detector input samples and $P(\underline{u}_{-1},\ \underline{u}_1)$ represents the joint *a priori* probability of the bit sequences $\underline{u}_{-1}$ and $\underline{u}_1$. Since the bit sequences $\underline{u}_{-1}$ and $\underline{u}_1$ are mutually independent and contain independent, equiprobable binary values,

$$\hat{\underline{u}}_0 = \arg \max_{\underline{u}_0} \; \Big[\sum_{\underline{u}_{-1}} \sum_{\underline{u}_1} p(\underline{y}|\underline{u}_0,\ \underline{u}_{-1},\ \underline{u}_1)\Big]. \tag{5.7}$$

The complexity involved in the maximization of $p(\underline{y}|\underline{u}_0)$ is proportional to the number of distinct pairs $(\underline{u}_{-1},\ \underline{u}_1)$. As stated in [5], for a high SNR, if the conditional densities involved in (5.7) are dominated by one particular pair $(\underline{u}_{-1},\ \underline{u}_1)$, one can make the following approximation

$$\begin{aligned}&\max_{\underline{u}_0} \; \Big[\sum_{\underline{u}_{-1}} \sum_{\underline{u}_1} p(\underline{y}|\underline{u}_0,\ \underline{u}_{-1},\ \underline{u}_1)\Big] \\ &\qquad \approx \max_{\underline{u}_0,\, \underline{u}_{-1},\, \underline{u}_1} \; p(\underline{y}|\underline{u}_0,\ \underline{u}_{-1},\ \underline{u}_1). \end{aligned} \tag{5.8}$$

The right hand side of (5.8) corresponds to joint ML sequence detection for $\underline{u}_{-1}$, $\underline{u}_0$, and $\underline{u}_1$, i.e., ML symbol sequence detection. Thus, a detection scheme, based on the Viterbi algorithm, that computes the ML symbol sequence and outputs the middle bit of each detected symbol can be viewed as a high SNR approximation for ML bit sequence detection. We refer to this detector as a punctured ML symbol sequence detector since it only outputs the detected sequence on the main track while discarding the detected sequences on the outer tracks.

Both the MAP bit detector and the punctured ML symbol detector can be implemented by algorithms working on the 36-state trellis [6], [7]. We have found in our simulation studies that these two detectors give virtually the same BER performance on channels with moderate to high SNR.

5.3 BER Performance Simulation Results

In this section, we present simulated BER curves obtained for the MAP bit detector as a function of the ITI level $b \in (0, 1]$. Results corresponding to channels with SNR $= 16$ dB and ISI levels $a = 0, 0.125$, and 0.2 are shown in Fig. 5.1. For the highest ISI level, $a = 0.2$, we also show results corresponding to a higher SNR level of 18 dB.

Somewhat contrary to intuition, we see that in all four scenarios, for ITI parameter values b roughly in the interval $[0.5,\ 0.65]$, increasing the level of ITI leads to improved BER performance.

We also examined the simulated BER for MAP bit detection over a wide range of SNR for two channels H_1 and H_2 with the same ISI level $a = 0.2$ and with the ITI levels $b = 0.55$ and $b = 0.6$

$$H_1 = \begin{pmatrix} 0.11 & 0.55 & 0.11 \\ 0.2 & 1 & 0.2 \\ 0.11 & 0.55 & 0.11 \end{pmatrix} \tag{5.9}$$

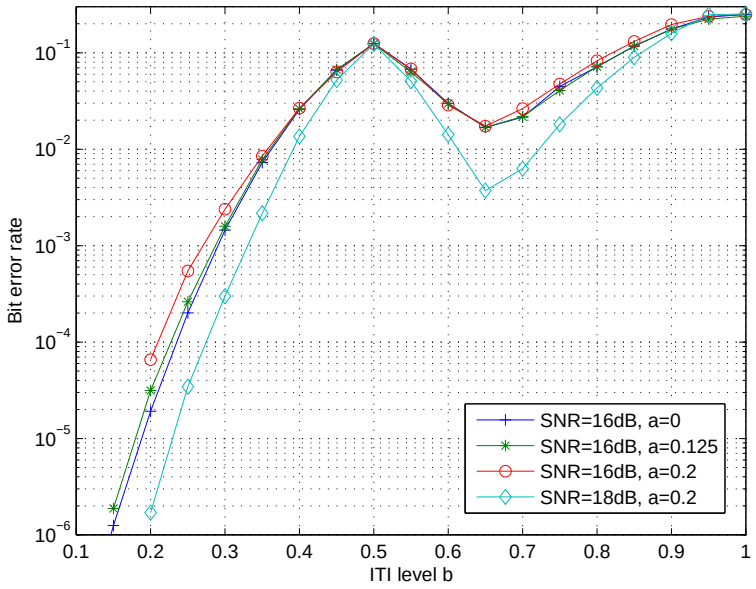

Figure 5.1 Bit error rates as a function of ITI level for MAP bit detection.

$$H_2 = \begin{pmatrix} 0.12 & 0.6 & 0.12 \\ 0.2 & 1 & 0.2 \\ 0.12 & 0.6 & 0.12 \end{pmatrix}. \tag{5.10}$$

The results are shown in Fig. 5.2. Although channel H_2 has a higher level of ITI, it performs significantly better than channel H_1 over the entire range of SNR considered. Note that at a 10^{-4} target BER, there is a 6 dB performance difference between these channels. We also simulated the BER performance of the punctured ML symbol sequence detector for these two channels. The results were indistinguishable from those produced by the MAP bit detector. We will make use of this fact in Section 5.5.2 when we use analytical methods to try to explain the observed performance.

We remark that channels H_1 and H_2 have high levels of ITI, as might arise when the read head is significantly wider than the track pitch. This situation could be applicable to early generations of BPM recording technology [1]. The use of wide read heads also has been proposed for improved timing and position error detection in the context of BPM recording [8].

In the presence of read head offset, the contributions of islands in the upper and lower tracks to the readback signal are no longer equal. The parametric model of the channel response

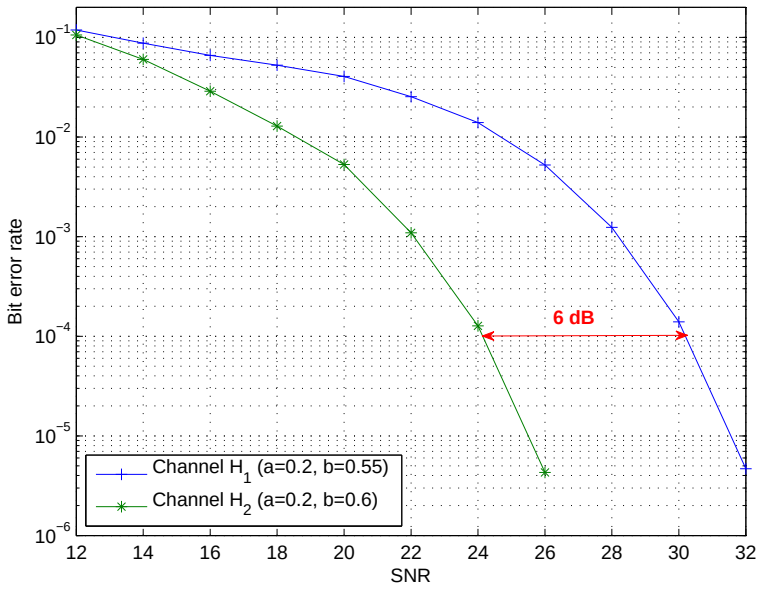

Figure 5.2 Simulated bit error rates for channels H_1 and H_2 for MAP bit detection.

matrix takes the form

$$H^* = \begin{pmatrix} ac & c & ac \\ a & 1 & a \\ ad & d & ad \end{pmatrix}. \tag{5.11}$$

For such a channel, the noiseless channel input-output relationship can be represented by a 64-state trellis as shown in Section 4.3.

We define TMR arising from the read head offset as

$$\text{TMR} = \frac{\text{Read head offset}}{\text{Track pitch}} \times 100\%. \tag{5.12}$$

To determine the parameters c and d in (5.11) as a function of TMR, we consider specific geometries for the read head and island configuration. The areal density is 1 Tb/in^2, with a regular array of square islands having side dimension 12.5 nm and center-to-center spacing of 25 nm. The magnetoresistive (MR) read sensor has thickness 5 nm. For a given level b of ontrack ITI and a specified TMR value, we determine the corresponding read head width and offtrack position. The resulting contributions of islands in the upper and lower tracks to the readback signal are then computed, yielding the ITI parameters c and d [1]. Fig. 5.3 shows the simulated BER curves for MAP bit detection as a function of ITI level b for channels with 10% and 15% TMR, ISI levels $a = 0$ and $a = 0.2$, and SNR equal to 20 dB. These results show that the non-monotonic relationship between the BER and ITI level that was observed when the head is ontrack also arises in the presence of TMR.

5.4 Error event characterization

In this Section, we introduce a modification to the standard error event analysis developed for ML bit sequence detection for conventional ISI channels that can be applied to the error event analysis of the punctured ML symbol sequence detector. We refer, in particular, to the analysis of partial-response maximum-likelihood (PRML) channel performance in [9] and [10].

Denote an input error sequence on the main track by

$$\varepsilon_{u_0}(D) = u_0(D) - u_0'(D), \tag{5.13}$$

and the input error sequences on the outer tracks by

$$\varepsilon_{u_{-1}}(D) = u_{-1}(D) - u_{-1}'(D) \tag{5.14}$$

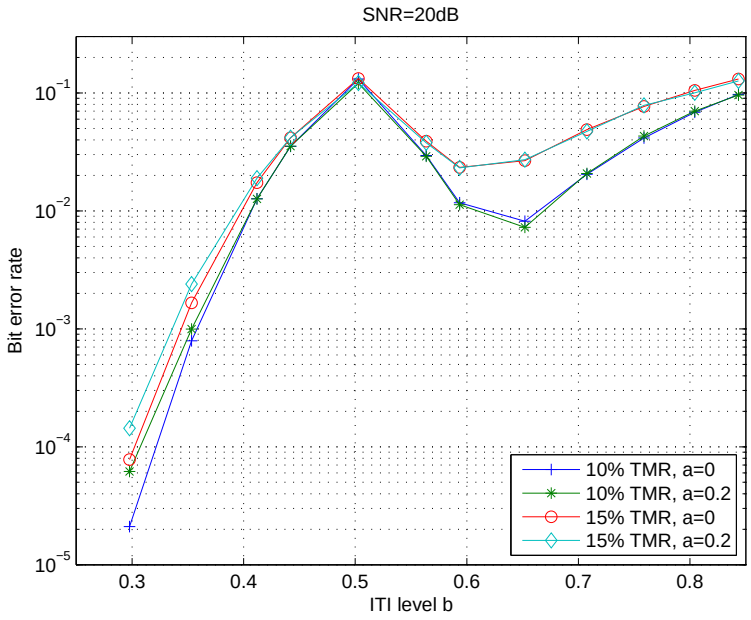

Figure 5.3 Bit error rates as a function of ITI level for MAP bit detection in the presence of TMR.

and

$$\varepsilon_{u_1}(D) = u_1(D) - u_1'(D) \tag{5.15}$$

where D denotes the delay operator. Here, $u_{-1}'(D)$, $u_0'(D)$, and $u_1'(D)$ represent the estimates of the sequences written on the upper, main, and lower tracks produced by the ML symbol sequence detector. Note that the punctured detector produces an error only when there is an error in $u_0'(D)$, regardless of the correctness of $u_{-1}'(D)$ and $u_1'(D)$. The input symbol error sequence

$$\varepsilon_u(D) = \begin{bmatrix} \varepsilon_{u_{-1}}(D) \\ \varepsilon_{u_0}(D) \\ \varepsilon_{u_1}(D) \end{bmatrix} \tag{5.16}$$

is a sequence of input symbol differences $[i, j, k]^T$ where $i,\ j,\ k \in \{0, 2, -2\}$ and T denotes matrix transpose.

The corresponding output symbol error sequence is

$$\varepsilon_v(D) = h_{-1}(D)\varepsilon_{u_{-1}}(D) + h_0(D)\varepsilon_{u_0}(D) + h_1(D)\varepsilon_{u_1}(D) \tag{5.17}$$

where $h_{-1}(D)$, $h_0(D)$, and $h_1(D)$ represent the channel responses of the upper, main, and lower tracks.

An error event λ extends from time k_1 to k_2 where $\varepsilon_{u,k_1-k} = \underline{0}$ for all $0 < k \leq \nu$, $\varepsilon_{u,k_1} \neq \underline{0}$, and k_2 is the smallest value of $k \geq k_1$ where $\varepsilon_{u,k_2-\nu} \neq \underline{0}$ and $\varepsilon_{u,k_2} = \varepsilon_{u,k_2-1} = \ldots = \varepsilon_{u,k_2-\nu+1} = \underline{0}$. Here, ν represents the memory in the channel. The squared-Euclidean distance of the error event λ is

$$d^2(\lambda) = \sum_{k=k_1}^{k_2} \varepsilon_{v,k}^2. \tag{5.18}$$

5.4.1 Error State Diagram

In this section, we discuss the error state diagram for the punctured ML symbol sequence detector. The error state diagram represents the input error sequences and their corresponding output symbol error sequences. Denote the alphabet of the input error symbols by $\mathcal{B}$. The initial state in the error state diagram is denoted by the input error symbols $\varepsilon_{u,k-2}$ and $\varepsilon_{u,k-1}$ from the alphabet $\mathcal{B}$. Each edge is labeled with an input error symbol $\varepsilon_{u,k}$ and the corresponding squared Euclidean distance $\varepsilon_{v,k}^2$.

For an alphabet $\mathcal{A} = \{-1, +1\}$ of input bits for each track, the alphabet for the track input errors is $\mathcal{C} = \{-2, 0, +2\}$ resulting in an alphabet with the size $|\mathcal{C}|^3 = 3^3 = 27$ for the input error symbols. In the presence of symmetry in the channel response, the expression for the output symbol error consists of the sum of input errors for the outer tracks. Therefore, by invoking the alphabet $\mathcal{D} = \{-4, -2, -0, 2, 4\}$ corresponding to the sum of input errors for the outer tracks, the size of the alphabet for the input error symbols $\mathcal{B}$ can be reduced to $|\mathcal{D}| \times |\mathcal{A}| = 5 \times 3 = 15$. With such a reduction in the size of the alphabet for the input error symbols, the number of states in the error state diagram can be reduced from 27^2 to 15^2.

We will use the notation $\underline{\alpha}$ to represent each element from the reduced alphabet $\mathcal{B}$. Note that some of the elements of the alphabet $\mathcal{B}$ for the reduced error state diagram may consist of a set of input error symbols from the input error symbol alphabet for the original error state diagram. Denote the input errors on the upper, main, and lower tracks by c_1, c_2, and c_3, respectively. Then, each element of the alphabet $\mathcal{B}$ is represented by $\underline{\alpha}$ where $\alpha = c_2 + 3(c_1 + c_3)/2$. For example, $\underline{5}$ denotes the set of input error symbols $[0, 2, 2]^T$ and $[2, 2, 0]^T$. The pairs of input symbols that generate the input error symbols in $\underline{5}$ are given in Table 5.1.

The probability of each element $\underline{\alpha}$ in the alphabet $\mathcal{B}$ is shown in Table 5.1. For example, the element $\underline{5}$ has the probability of $3/8$ since it can only occur if, out of the 8 possible input symbols, one of the 3 symbols shown in the first column of Table 5.1 is recorded. Table 5.2 lists the probabilities for all set of differences $\underline{\alpha}$.

Table 5.1 The set of input error symbols $\underline{5}$

recorded symbol	detected symbol	input error symbol
$[+,+,-]^T$	$[-,-,-]^T$	$[2,2,0]^T$
$[+,+,+]^T$	$[-,-,+]^T$ $[+,-,-]^T$	$[2,2,0]^T$ $[0,2,2]^T$
$[-,+,+]^T$	$[-,-,-]^T$	$[0,2,2]^T$

Table 5.2 Probabilities for the sets of input symbol differences

$\underline{\alpha}$	$P(\underline{\alpha})$
$\underline{1}, -\underline{1}$	$3/8$
$\underline{2}, -\underline{2}$	$1/2$
$\underline{3}, -\underline{3}$	$3/4$
$\underline{4}, -\underline{4}$	$1/8$
$\underline{5}, -\underline{5}$	$3/8$
$\underline{6}, -\underline{6}$	$1/4$
$\underline{8}, -\underline{8}$	$1/8$

Denote the number of bit errors in the bit sequence recorded on the main track for the error event λ by $w_{u_0}(\lambda)$

$$w_{u_0}(\lambda) = \sum_{k=k_1}^{k_2} \frac{|\varepsilon_{u_0,k}|}{2} \tag{5.19}$$

and the number of occurrences of $\underline{\alpha}$ in the error event λ by $w_{\underline{\alpha}}(\lambda)$. Let D^* denote the set of all possible error event distances d and let Λ_d denote the set of all error events with Euclidean distance d. Define N_d as the average multiplicity of bit errors resulting from error events with the Euclidean distance d

$$N_d = \sum_{\lambda \in \Lambda_d} w_{u_0}(\lambda) \prod_{\underline{\alpha}} P(\underline{\alpha})^{w_{\underline{\alpha}}(\lambda)}. \tag{5.20}$$

Then, the probability of a bit error P_e can be bounded from above by means of the union bound [11]

$$P_e \leq \sum_{d \in D^*} N_d Q(d/2\sigma). \tag{5.21}$$

At moderate-to-high SNR, we have the approximation

$$P_e \approx N_{d_{\min}} Q(d_{\min}/2\sigma) \tag{5.22}$$

where $d_{\min}$ represents the minimum Euclidean distance. An error event with the minimum Euclidean distance $d_{\min}$ is called a dominant error event.

5.5 Performance Analysis

In this section, we use analytical methods to provide insight into the performance curve characteristics described in the previous section. We first address the channel with no ISI, where an exact performance analysis for the MAP bit detector can be carried out. We then turn to the more difficult case of channels with ISI, where an error event analysis of the punctured ML symbol sequence detector is used to shed light on the simulated BER results for the two channels H_1 and H_2.

5.5.1 No-ISI case

Consider a channel with no ISI where the channel output at time index i is

$$y_i = bu_{i,-1} + u_{i,0} + bu_{i,1} + w_i. \tag{5.23}$$

Under the assumption that the recorded bits are independent and equiprobable binary values, the decision rule at time index i that minimizes the probability of a bit error is

$$\begin{aligned} \hat{u}_{i,0} &= -1 \qquad && \text{if } p(y_i|u_{i,0} = -1) > p(y_i|u_{i,0} = 1) \\ \hat{u}_{i,0} &= +1 && \text{otherwise} \end{aligned}$$

where $\hat{u}_{i,0}$ represents the estimated channel input recorded on the main track at time index i. Here, $p(y_i|u_{i,0} = -1)$ represents the conditional probability density function (cpdf) of the channel output y_i given that channel input $u_{i,0} = -1$. Similarly, $p(y_i|u_{i,0} = 1)$ represents the cpdf of the channel output y_i given that channel input $u_{i,0} = 1$. The cpdf's $p(y_i|u_{i,0} = -1)$ and $p(y_i|u_{i,0} = 1)$, respectively, take the form

$$\begin{aligned} p(y_i|u_{i,0} = -1) &= \sum_{u_{i,-1}} \sum_{u_{i,1}} p(y_i,\ u_{i,-1},\ u_{i,1}|u_{i,0} = -1) \\ &= \sum_{u_{i,-1}} \sum_{u_{i,1}} p(y_i|u_{i,0} = -1,\ u_{i,-1},\ u_{i,1}) \\ &\qquad \cdot P(u_{i,-1},\ u_{i,1}) \end{aligned} \tag{5.24}$$

$$\begin{aligned} p(y_i|u_{i,0} = +1) &= \sum_{u_{i,-1}} \sum_{u_{i,1}} p(y_i,\ u_{i,-1},\ u_{i,1}|u_{i,0} = +1) \\ &= \sum_{u_{i,-1}} \sum_{u_{i,1}} p(y_i|u_{i,0} = +1,\ u_{i,-1},\ u_{i,1}) \\ &\qquad \cdot P(u_{i,-1},\ u_{i,1}) \end{aligned} \tag{5.25}$$

where $P(u_{i,-1},\ u_{i,1})$ represents the joint *a priori* probability of the bits $u_{i,-1}$ and $u_{i,1}$. As seen from (5.24) and (5.25), these cpdf's depend on the channel inputs of the three tracks. The probability of a bit error P_e is

$$\begin{aligned} P_e = {} & P(u_{i,0} = -1)P(\hat{u}_{i,0} = +1 | u_{i,0} = -1) \\ & + P(u_{i,0} = +1)P(\hat{u}_{i,0} = -1 | u_{i,0} = +1). \end{aligned}$$

When the ITI parameter satisfies $b \in (0,\ 0.5]$, the decision rule is

$$\begin{aligned} \hat{u}_{i,0} &= -1 && \text{if } y_i < 0 \\ \hat{u}_{i,0} &= +1 && \text{otherwise.} \end{aligned}$$

The probability of a bit error P_e then takes the simple form

$$P_e = \frac{1}{4}Q\left(\frac{2-4b}{2\sigma}\right) + \frac{1}{2}Q\left(\frac{2}{2\sigma}\right) + \frac{1}{4}Q\left(\frac{2+4b}{2\sigma}\right) \tag{5.26}$$

where $Q(t) = \frac{1}{\sqrt{2\pi}}\int_t^\infty e^{-x^2/2}\,dx$. Note that $Q(t)$ is a decreasing function of t. At moderate-to-high SNR, the dominant term in (5.26) is $\frac{1}{4}Q\left(\frac{2-4b}{2\sigma}\right)$ which results from the distance $2-4b$. This corresponds to the distance between the nearest pair of noiseless channel outputs corresponding to main track inputs $u_{i,0} = -1$ and $u_{i,0} = 1$, respectively, as illustrated in Fig. 5.4. Since the minimum distance is a decreasing function of b, the performance degrades with increasing b.

When the ITI parameter satisfies $b \in (0.5,\ 1]$, the decision rule is

$$\begin{aligned} \hat{u}_{i,0} &= -1 && \text{if } -\infty < y_i < -e \text{ or } 0 < y_i < e \\ \hat{u}_{i,0} &= +1 && \text{otherwise} \end{aligned}$$

where e represents the positive value of y_i for which the two cpdf's are equal. The cpdf's for this region are illustrated in Fig. 5.5. At moderate-to-high SNR, $e \approx b$. If the parameter e is chosen to be b, the probability of a bit error P_e is given by

$$\begin{aligned} P_e = {} & \frac{1}{4}\Big[Q\left(\frac{2+2b}{2\sigma}\right) - Q\left(\frac{2+4b}{2\sigma}\right) + Q\left(\frac{2+6b}{2\sigma}\right)\Big] \\ & + \frac{1}{2}\Big[Q\left(\frac{2-2b}{2\sigma}\right) - Q\left(\frac{2}{2\sigma}\right) + Q\left(\frac{2+2b}{2\sigma}\right)\Big] \\ & + \frac{1}{4}\Big[Q\left(\frac{-2+4b}{2\sigma}\right) - Q\left(\frac{-2+6b}{2\sigma}\right) \\ & \quad + Q\left(\frac{2-2b}{2\sigma}\right)\Big]. \end{aligned} \tag{5.27}$$

When the ITI parameter $b \in (0.5, 2/3)$, the dominant term in (5.27) is $\frac{1}{4}Q\left(\frac{-2+4b}{2\sigma}\right)$ which results from the minimum distance $-2+4b$. Note that since the minimum distance in this region increases with increasing b, the performance improves with increasing minimum distance. When the ITI parameter satisfies $b \in (2/3, 1]$, the dominant term in (5.27) is $\frac{3}{4}Q\left(\frac{2-2b}{2\sigma}\right)$. This results from the minimum distance $2-2b$ which is again a decreasing function of b. Therefore, the performance degrades in this region with decreasing minimum distance.

5.5.2 ISI case

For the ISI case, the analysis of the MAP bit detector is more difficult. Therefore, recalling that the performance of the punctured ML symbol sequence detector was found to be effectively the same as that of the optimal bit detector, we use the error event analysis for punctured ML symbol sequence detector discussed in Section 5.4.

By means of a depth first search, the input symbol error events with small output distances can be listed. In Table 5.3, we list all input symbol error events with output squared-Euclidean distances up to 0.1 on channel H_1 defined in (5.9) and, in Table 5.4, we list all input symbol error events with output squared-Euclidean distances up to 0.4 on channel H_2 defined

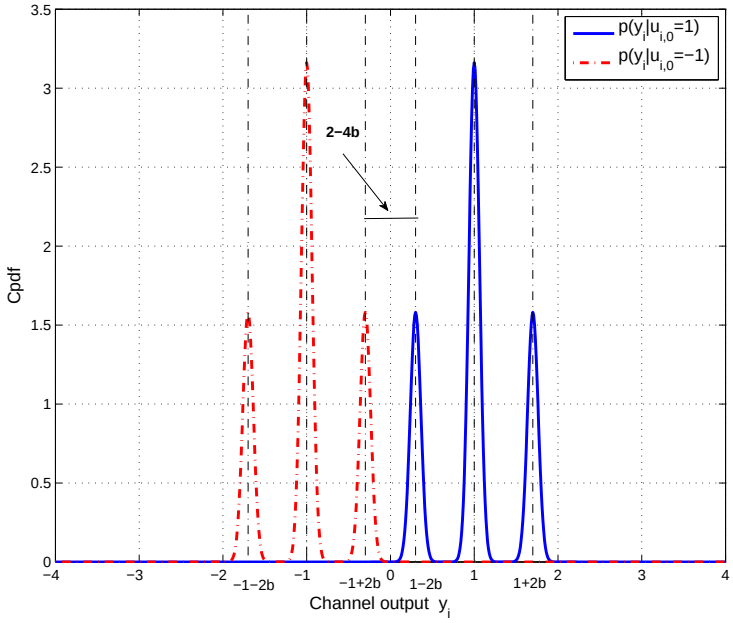

Figure 5.4 Conditional probability density functions when the ITI parameter satsifies $b \in (0, 0.5]$.

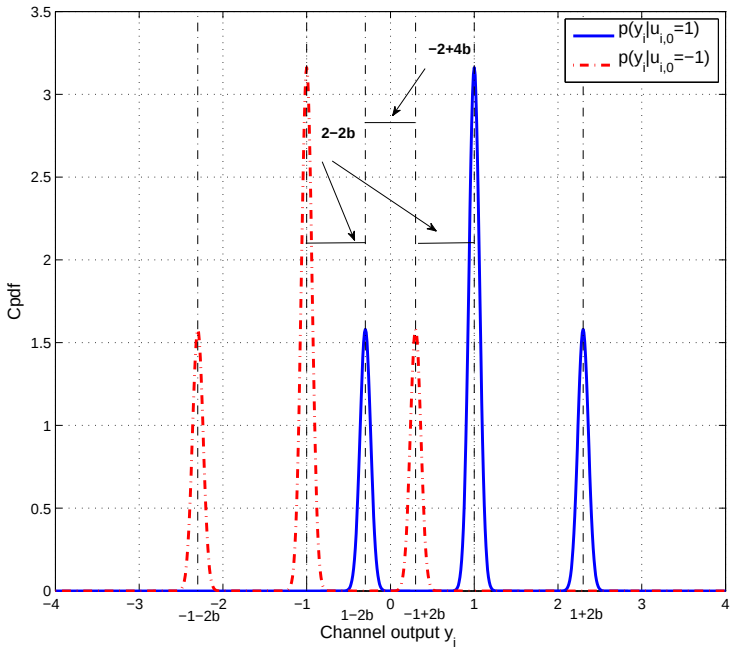

Figure 5.5 Conditional probability density functions when the ITI parameter $b \in (0.5, 1]$.

in (5.10). For convenience, only the error events which begin with a negative input symbol difference are listed. Note that for channel H_2, the channel corresponding to ITI level $b = 0.6$, the squared-Euclidean distance of the dominant error event is 4 times that of channel H_1, with ITI level $b = 0.55$, whereas the average multiplicities of bit errors resulting from the dominant error events for the two channels are the same. Therefore, at moderate-to-high SNR, we would expect a 6 dB performance advantage for channel H_2 compared to the channel H_1, despite the larger ITI level of channel H_2. This 6 dB performance advantage was indeed demonstrated in the simulated BER curves in Fig. 5.2.

Table 5.3: Error events for channel H_1 up to squared distance 0.15

Error Event, λ	$d^2(\lambda)$	N_d
$\underline{0}\,\underline{0}\,-\underline{4}\,\underline{0}\,\underline{0}$	0.0432	$1/8$
$\underline{0}\,\underline{0}\,-\underline{4}\,\underline{4}\,\underline{0}\,\underline{0}$	0.0544	$1/32$
$\underline{0}\,\underline{0}\,-\underline{4}\,\underline{4}\,-\underline{4}\,\underline{0}\,\underline{0}$	0.0688	$3/8^3$
$\underline{0}\,\underline{0}\,-\underline{4}\,\underline{0}\,\underline{4}\,\underline{0}\,\underline{0}$	0.0832	$1/32$

Table 5.3 – continued from previous page

Error Event, λ	$d^2(\lambda)$	N_d
$\underline{0}\,\underline{0}\,-\underline{4}\,\underline{4}\,-\underline{4}\,\underline{4}\,\underline{0}\,\underline{0}$	0.0832	$4/8^4$
$\underline{0}\,\underline{0}\,-\underline{4}\,\underline{0}\,-\underline{4}\,\underline{0}\,\underline{0}$	0.0896	$1/32$
$\underline{0}\,\underline{0}\,-\underline{4}\,\underline{0}\,\underline{4}\,-\underline{4}\,\underline{0}\,\underline{0}$	0.0944	$3/8^3$
$\underline{0}\,\underline{0}\,-\underline{4}\,\underline{4}\,\underline{0}\,-\underline{4}\,\underline{0}\,\underline{0}$	0.0944	$3/8^3$
$\underline{0}\,\underline{0}\,-\underline{4}\,\underline{4}\,-\underline{4}\,\underline{4}\,-\underline{4}\,\underline{0}\,\underline{0}$	0.0976	$5/8^5$
$\underline{0}\ \underline{0}\ -\underline{4}\ \underline{0}\ -\underline{4}\ \underline{4}\ \underline{0}\ \underline{0}$	0.1008	$3/8^3$
$\underline{0}\ \underline{0}\ -\underline{4}\ \underline{4}\ \underline{0}\ \underline{4}\ \underline{0}\ \underline{0}$	0.1008	$3/8^3$
$\underline{0}\ \underline{0}\ -\underline{4}\ \underline{4}\ \underline{0}\ -\underline{4}\ \underline{4}\ \underline{0}\ \underline{0}$	0.1056	$4/8^4$
$\underline{0}\ \underline{0}\ -\underline{4}\ \underline{4}\ -\underline{4}\ \underline{0}\ \underline{4}\ \underline{0}\ \underline{0}$	0.1088	$4/8^4$
$\underline{0}\ \underline{0}\ -\underline{4}\ \underline{0}\ \underline{4}\ -\underline{4}\ \underline{4}\ \underline{0}\ \underline{0}$	0.1088	$4/8^4$
$\underline{0}\ \underline{0}\ -\underline{4}\ \underline{4}\ \underline{0}\ \underline{4}\ -\underline{4}\ \underline{0}\ \underline{0}$	0.1120	$4/8^4$
$\underline{0}\ \underline{0}\ -\underline{4}\ \underline{4}\ -\underline{4}\ \underline{4}\ -\underline{4}\ \underline{4}\ \underline{0}\ \underline{0}$	0.1120	$6/8^6$
$\underline{0}\ \underline{0}\ -\underline{4}\ \underline{0}\ -\underline{4}\ \underline{4}\ -\underline{4}\ \underline{0}\ \underline{0}$	0.1152	$4/8^4$
$\underline{0}\ \underline{0}\ -\underline{4}\ \underline{4}\ -\underline{4}\ \underline{0}\ -\underline{4}\ \underline{0}\ \underline{0}$	0.1152	$4/8^4$
$\underline{0}\ \underline{0}\ -\underline{4}\ -\underline{4}\ \underline{0}\ \underline{0}$	0.1184	$2/8^2$
$\underline{0}\ \underline{0}\ -\underline{4}\ \underline{4}\ \underline{0}\ -\underline{4}\ \underline{4}\ -\underline{4}\ \underline{0}\ \underline{0}$	0.1200	$5/8^5$
$\underline{0}\ \underline{0}\ -\underline{4}\ \underline{4}\ -\underline{4}\ \underline{0}\ \underline{4}\ -\underline{4}\ \underline{0}\ \underline{0}$	0.1200	$5/8^5$
$\underline{0}\ \underline{0}\ -\underline{4}\ \underline{4}\ -\underline{4}\ \underline{4}\ \underline{0}\ -\underline{4}\ \underline{0}\ \underline{0}$	0.1232	$5/8^5$
$\underline{0}\ \underline{0}\ -\underline{4}\ \underline{0}\ \underline{4}\ -\underline{4}\ \underline{4}\ -\underline{4}\ \underline{0}\ \underline{0}$	0.1232	$5/8^5$
$\underline{0}\ \underline{0}\ -\underline{4}\ \underline{0}\ \underline{4}\ \underline{0}\ -\underline{4}\ \underline{0}\ \underline{0}$	0.1232	$3/8^3$
$\underline{0}\ \underline{0}\ -\underline{4}\ -\underline{4}\ \underline{4}\ \underline{0}\ \underline{0}$	0.1264	$3/8^3$
$\underline{0}\ \underline{0}\ -\underline{4}\ \underline{4}\ \underline{4}\ \underline{0}\ \underline{0}$	0.1264	$3/8^3$
$\underline{0}\ \underline{0}\ -\underline{4}\ \underline{4}\ -\underline{4}\ \underline{4}\ -\underline{4}\ \underline{4}\ -\underline{4}\ \underline{0}\ \underline{0}$	0.1264	$7/8^7$
$\underline{0}\ \underline{0}\ -\underline{4}\ \underline{4}\ \underline{0}\ \underline{4}\ -\underline{4}\ \underline{4}\ \underline{0}\ \underline{0}$	0.1264	$5/8^5$
$\underline{0}\ \underline{0}\ -\underline{4}\ \underline{4}\ -\underline{4}\ \underline{0}\ -\underline{4}\ \underline{4}\ \underline{0}\ \underline{0}$	0.1264	$5/8^5$
$\underline{0}\ \underline{0}\ -\underline{4}\ \underline{0}\ -\underline{4}\ \underline{0}\ \underline{4}\ \underline{0}\ \underline{0}$	0.1296	$3/8^3$
$\underline{0}\ \underline{0}\ -\underline{4}\ \underline{0}\ -\underline{4}\ \underline{4}\ -\underline{4}\ \underline{4}\ \underline{0}\ \underline{0}$	0.1296	$5/8^5$
$\underline{0}\ \underline{0}\ -\underline{4}\ \underline{4}\ -\underline{4}\ \underline{4}\ \underline{0}\ \underline{4}\ \underline{0}\ \underline{0}$	0.1296	$5/8^5$
$\underline{0}\ \underline{0}\ -\underline{4}\ \underline{0}\ \underline{4}\ \underline{0}\ \underline{4}\ \underline{0}\ \underline{0}$	0.1296	$3/8^3$
$\underline{0}\ \underline{0}\ -\underline{4}\ \underline{0}\ \underline{4}\ -\underline{4}\ \underline{0}\ \underline{4}\ \underline{0}\ \underline{0}$	0.1344	$4/8^4$
$\underline{0}\ \underline{0}\ -\underline{4}\ \underline{4}\ -\underline{4}\ \underline{4}\ \underline{0}\ -\underline{4}\ \underline{4}\ \underline{0}\ \underline{0}$	0.1344	$6/8^6$

Table 5.3 – continued from previous page

Error Event, λ	$d^2(\lambda)$	N_d
$\underline{0}\ \underline{0}\ \underline{-4}\ \underline{4}\ \underline{4}\ \underline{-4}\ \underline{0}\ \underline{0}$	0.1344	$4/8^4$
$\underline{0}\ \underline{0}\ \underline{-4}\ \underline{4}\ \underline{0}\ \underline{-4}\ \underline{4}\ \underline{-4}\ \underline{4}\ \underline{0}\ \underline{0}$	0.1344	$6/8^6$
$\underline{0}\ \underline{0}\ \underline{-4}\ \underline{4}\ \underline{0}\ \underline{-4}\ \underline{0}\ \underline{4}\ \underline{0}\ \underline{0}$	0.1344	$4/8^4$
$\underline{0}\ \underline{0}\ \underline{-4}\ \underline{0}\ \underline{4}\ \underline{0}\ \underline{-4}\ \underline{4}\ \underline{0}\ \underline{0}$	0.1344	$4/8^4$
$\underline{0}\ \underline{0}\ \underline{-4}\ \underline{4}\ \underline{-4}\ \underline{0}\ \underline{4}\ \underline{-4}\ \underline{4}\ \underline{0}\ \underline{0}$	0.1344	$6/8^6$
$\underline{0}\ \underline{0}\ \underline{-4}\ \underline{0}\ \underline{-4}\ \underline{0}\ \underline{-4}\ \underline{0}\ \underline{0}$	0.1360	$3/8^3$
$\underline{0}\ \underline{0}\ \underline{-4}\ \underline{0}\ \underline{4}\ \underline{-4}\ \underline{4}\ \underline{-4}\ \underline{4}\ \underline{0}\ \underline{0}$	0.1376	$6/8^6$
$\underline{0}\ \underline{0}\ \underline{-4}\ \underline{4}\ \underline{-4}\ \underline{4}\ \underline{-4}\ \underline{0}\ \underline{4}\ \underline{0}\ \underline{0}$	0.1376	$6/8^6$
$\underline{0}\ \underline{0}\ \underline{-4}\ \underline{-4}\ \underline{4}\ \underline{-4}\ \underline{0}\ \underline{0}$	0.1408	$4/8^4$
$\underline{0}\ \underline{0}\ \underline{-4}\ \underline{0}\ \underline{-4}\ \underline{0}\ \underline{4}\ \underline{-4}\ \underline{0}\ \underline{0}$	0.1408	$4/8^4$
$\underline{0}\ \underline{0}\ \underline{-4}\ \underline{0}\ \underline{-4}\ \underline{4}\ \underline{-4}\ \underline{0}\ \underline{0}$	0.1408	$4/8^4$
$\underline{0}\ \underline{0}\ \underline{-4}\ \underline{0}\ \underline{4}\ \underline{-4}\ \underline{0}\ \underline{-4}\ \underline{0}\ \underline{0}$	0.1408	$4/8^4$
$\underline{0}\ \underline{0}\ \underline{-4}\ \underline{4}\ \underline{0}\ \underline{4}\ \underline{-4}\ \underline{4}\ \underline{-4}\ \underline{0}\ \underline{0}$	0.1408	$6/8^6$
$\underline{0}\ \underline{0}\ \underline{-4}\ \underline{4}\ \underline{0}\ \underline{4}\ \underline{0}\ \underline{-4}\ \underline{0}\ \underline{0}$	0.1408	$4/8^4$
$\underline{0}\ \underline{0}\ \underline{-4}\ \underline{0}\ \underline{4}\ \underline{0}\ \underline{4}\ \underline{-4}\ \underline{0}\ \underline{0}$	0.1408	$4/8^4$
$\underline{0}\ \underline{0}\ \underline{-4}\ \underline{4}\ \underline{-4}\ \underline{0}\ \underline{-4}\ \underline{4}\ \underline{-4}\ \underline{0}\ \underline{0}$	0.1408	$6/8^6$
$\underline{0}\ \underline{0}\ \underline{-4}\ \underline{4}\ \underline{-4}\ \underline{-4}\ \underline{0}\ \underline{0}$	0.1408	$4/8^4$
$\underline{0}\ \underline{0}\ \underline{-4}\ \underline{4}\ \underline{-4}\ \underline{4}\ \underline{-4}\ \underline{4}\ \underline{-4}\ \underline{4}\ \underline{0}\ \underline{0}$	0.1408	$8/8^8$
$\underline{0}\ \underline{0}\ \underline{-4}\ \underline{4}\ \underline{-4}\ \underline{4}\ \underline{0}\ \underline{4}\ \underline{-4}\ \underline{0}\ \underline{0}$	0.1408	$6/8^6$
$\underline{0}\ \underline{0}\ \underline{-4}\ \underline{4}\ \underline{0}\ \underline{-4}\ \underline{0}\ \underline{-4}\ \underline{0}\ \underline{0}$	0.1408	$4/8^4$
$\underline{0}\ \underline{0}\ \underline{-4}\ \underline{0}\ \underline{-4}\ \underline{4}\ \underline{-4}\ \underline{4}\ \underline{-4}\ \underline{0}\ \underline{0}$	0.1440	$6/8^6$
$\underline{0}\ \underline{0}\ \underline{-4}\ \underline{4}\ \underline{-4}\ \underline{4}\ \underline{-4}\ \underline{0}\ \underline{-4}\ \underline{0}\ \underline{0}$	0.1440	$6/8^6$
$\underline{0}\ \underline{0}\ \underline{-4}\ \underline{4}\ \underline{0}\ \underline{-4}\ \underline{0}\ \underline{4}\ \underline{-4}\ \underline{0}\ \underline{0}$	0.1456	$5/8^5$
$\underline{0}\ \underline{0}\ \underline{-4}\ \underline{4}\ \underline{0}\ \underline{-4}\ \underline{4}\ \underline{0}\ \underline{-4}\ \underline{0}\ \underline{0}$	0.1456	$5/8^5$
$\underline{0}\ \underline{0}\ \underline{-4}\ \underline{0}\ \underline{4}\ \underline{-4}\ \underline{0}\ \underline{4}\ \underline{-4}\ \underline{0}\ \underline{0}$	0.1456	$5/8^5$
$\underline{0}\ \underline{0}\ \underline{-4}\ \underline{4}\ \underline{0}\ \underline{4}\ \underline{0}\ \underline{4}\ \underline{0}\ \underline{0}$	0.1472	$4/8^4$
$\underline{0}\ \underline{0}\ \underline{-4}\ \underline{0}\ \underline{-4}\ \underline{0}\ \underline{-4}\ \underline{4}\ \underline{0}\ \underline{0}$	0.1472	$4/8^4$
$\underline{0}\ \underline{0}\ \underline{-4}\ \underline{0}\ \underline{-4}\ \underline{4}\ \underline{0}\ \underline{4}\ \underline{0}\ \underline{0}$	0.1472	$4/8^4$
$\underline{0}\ \underline{0}\ \underline{-4}\ \underline{4}\ \underline{0}\ \underline{-4}\ \underline{4}\ \underline{-4}\ \underline{4}\ \underline{-4}\ \underline{0}\ \underline{0}$	0.1488	$7/8^7$
$\underline{0}\ \underline{0}\ \underline{-4}\ \underline{4}\ \underline{-4}\ \underline{4}\ \underline{0}\ \underline{-4}\ \underline{4}\ \underline{-4}\ \underline{0}\ \underline{0}$	0.1488	$7/8^7$
$\underline{0}\ \underline{0}\ \underline{-4}\ \underline{4}\ \underline{4}\ \underline{-4}\ \underline{4}\ \underline{0}\ \underline{0}$	0.1488	$5/8^5$

Table 5.3 – continued from previous page

Error Event, λ	$d^2(\lambda)$	N_d
$\underline{0}\ \underline{0}\ -\underline{4}\ \underline{4}\ -\underline{4}\ \underline{4}\ -\underline{4}\ \underline{0}\ \underline{4}\ -\underline{4}\ \underline{0}\ \underline{0}$	0.1488	$7/8^7$
$\underline{0}\ \underline{0}\ -\underline{4}\ \underline{0}\ \underline{4}\ -\underline{4}\ \underline{4}\ \underline{0}\ -\underline{4}\ \underline{0}\ \underline{0}$	0.1488	$5/8^5$
$\underline{0}\ \underline{0}\ -\underline{4}\ \underline{0}\ \underline{4}\ \underline{0}\ -\underline{4}\ \underline{4}\ -\underline{4}\ \underline{0}\ \underline{0}$	0.1488	$5/8^5$
$\underline{0}\ \underline{0}\ -\underline{4}\ \underline{4}\ -\underline{4}\ -\underline{4}\ \underline{4}\ \underline{0}\ \underline{0}$	0.1488	$5/8^5$
$\underline{0}\ \underline{0}\ -\underline{4}\ \underline{4}\ -\underline{4}\ \underline{0}\ \underline{4}\ -\underline{4}\ \underline{4}\ -\underline{4}\ \underline{0}\ \underline{0}$	0.1488	$7/8^7$
$\underline{0}\ \underline{0}\ -\underline{4}\ \underline{4}\ -\underline{4}\ \underline{0}\ \underline{4}\ \underline{0}\ -\underline{4}\ \underline{0}\ \underline{0}$	0.1488	$5/8^5$

Table 5.4: Error events for channel H_2 up to squared distance 0.6

Error Event, λ	$d^2(\lambda)$	N_d
$\underline{0}\,\underline{0}\,-\underline{4}\,\underline{0}\,\underline{0}$	0.1728	$1/8$
$\underline{0}\,\underline{0}\,-\underline{4}\,\underline{4}\,\underline{0}\,\underline{0}$	0.2176	$1/32$
$\underline{0}\,\underline{0}\,-\underline{4}\,\underline{4}\,-\underline{4}\,\underline{0}\,\underline{0}$	0.2752	$3/8^3$
$\underline{0}\,\underline{0}\,-\underline{4}\,\underline{0}\,\underline{4}\,\underline{0}\,\underline{0}$	0.3328	$1/32$
$\underline{0}\,\underline{0}\,-\underline{4}\,\underline{4}\,-\underline{4}\,\underline{4}\,\underline{0}\,\underline{0}$	0.3328	$4/8^4$
$\underline{0}\,\underline{0}\,-\underline{4}\,\underline{0}\,-\underline{4}\,\underline{0}\,\underline{0}$	0.3584	$1/32$
$\underline{0}\,\underline{0}\,-\underline{4}\,\underline{0}\,\underline{4}\,-\underline{4}\,\underline{0}\,\underline{0}$	0.3776	$3/8^3$
$\underline{0}\,\underline{0}\,-\underline{4}\,\underline{4}\,\underline{0}\,-\underline{4}\,\underline{0}\,\underline{0}$	0.3776	$3/8^3$
$\underline{0}\,\underline{0}\,-\underline{4}\,\underline{4}\,-\underline{4}\,\underline{4}\,-\underline{4}\,\underline{0}\,\underline{0}$	0.3904	$5/8^5$
$\underline{0}\ \underline{0}\ -\underline{4}\ \underline{4}\ \underline{0}\ \underline{4}\ \underline{0}\,\underline{0}$	0.4032	$3/8^3$
$\underline{0}\ \underline{0}\ -\underline{4}\ \underline{0}\,-\underline{4}\,\underline{4}\,\underline{0}\ \underline{0}$	0.4032	$3/8^3$
$\underline{0}\ \underline{0}\ -\underline{4}\ \underline{4}\ \underline{0}\ -\underline{4}\ \underline{4}\ \underline{0}\ \underline{0}$	0.4224	$4/8^4$
$\underline{0}\,\underline{0}\ -\underline{4}\ \underline{0}\ \underline{4}\ -\underline{4}\ \underline{4}\ \underline{0}\ \underline{0}$	0.4352	$4/8^4$
$\underline{0}\,\underline{0}\,-\underline{4}\ \underline{4}\,-\underline{4}\ \underline{0}\,\underline{4}\ \underline{0}\ \underline{0}$	0.4352	$4/8^4$
$\underline{0}\,\underline{0}\,-\underline{4}\ \underline{4}\ \underline{0}\ \underline{4}\ -\underline{4}\ \underline{0}\ \underline{0}$	0.4480	$4/8^4$
$\underline{0}\ \underline{0}\ -\underline{4}\ \underline{4}\,-\underline{4}\ \underline{4}\ -\underline{4}\ \underline{4}\ \underline{0}\ \underline{0}$	0.4480	$6/8^6$
$\underline{0}\ \underline{0}\,-\underline{4}\ \underline{0}\ -\underline{4}\ \underline{4}\,-\underline{4}\ \underline{0}\ \underline{0}$	0.4608	$4/8^4$
$\underline{0}\ \underline{0}\ -\underline{4}\ \underline{4}\ -\underline{4}\ \underline{0}\,-\underline{4}\ \underline{0}\ \underline{0}$	0.4608	$4/8^4$
$\underline{0}\ \underline{0}\ -\underline{4}\ -\underline{4}\ \underline{0}\ \underline{0}$	0.4736	$2/8^2$
$\underline{0}\ \underline{0}\ -\underline{4}\ \underline{4}\ \underline{0}\ -\underline{4}\ \underline{4}\ -\underline{4}\ \underline{0}\ \underline{0}$	0.4800	$5/8^5$

Table 5.4 – continued from previous page

Error Event, λ	$d^2(\lambda)$	N_d
$\underline{0}\ \underline{0}\ -\underline{4}\ \underline{4}\ -\underline{4}\ \underline{0}\ \underline{4}\ -\underline{4}\ \underline{0}\ \underline{0}$	0.4800	$5/8^5$
$\underline{0}\ \underline{0}\ -\underline{4}\ \underline{0}\ \underline{4}\ \underline{0}\ -\underline{4}\ \underline{0}\ \underline{0}$	0.4928	$3/8^3$
$\underline{0}\ \underline{0}\ -\underline{4}\ \underline{4}\ -\underline{4}\ \underline{4}\ \underline{0}\ -\underline{4}\ \underline{0}\ \underline{0}$	0.4928	$5/8^5$
$\underline{0}\ \underline{0}\ -\underline{4}\ \underline{0}\ \underline{4}\ -\underline{4}\ \underline{4}\ -\underline{4}\ \underline{0}\ \underline{0}$	0.4928	$5/8^5$
$\underline{0}\ \underline{0}\ -\underline{4}\ -\underline{4}\ \underline{4}\ \underline{0}\ \underline{0}$	0.5056	$3/8^3$
$\underline{0}\ \underline{0}\ -\underline{4}\ \underline{4}\ \underline{0}\ \underline{4}\ -\underline{4}\ \underline{4}\ \underline{0}\ \underline{0}$	0.5056	$5/8^5$
$\underline{0}\ \underline{0}\ -\underline{4}\ \underline{4}\ -\underline{4}\ \underline{4}\ -\underline{4}\ \underline{4}\ -\underline{4}\ \underline{0}\ \underline{0}$	0.5056	$6/8^6$
$\underline{0}\ \underline{0}\ -\underline{4}\ \underline{4}\ \underline{4}\ \underline{0}\ \underline{0}$	0.5056	$3/8^3$
$\underline{0}\ \underline{0}\ -\underline{4}\ \underline{4}\ -\underline{4}\ \underline{0}\ -\underline{4}\ \underline{4}\ \underline{0}\ \underline{0}$	0.5056	$5/8^5$
$\underline{0}\ \underline{0}\ -\underline{4}\ \underline{0}\ -\underline{4}\ \underline{4}\ -\underline{4}\ \underline{4}\ \underline{0}\ \underline{0}$	0.5184	$5/8^5$
$\underline{0}\ \underline{0}\ -\underline{4}\ \underline{0}\ \underline{4}\ \underline{0}\ \underline{4}\ \underline{0}\ \underline{0}$	0.5184	$3/8^3$
$\underline{0}\ \underline{0}\ -\underline{4}\ \underline{0}\ -\underline{4}\ \underline{0}\ \underline{4}\ \underline{0}\ \underline{0}$	0.5184	$3/8^3$
$\underline{0}\ \underline{0}\ -\underline{4}\ \underline{4}\ -\underline{4}\ \underline{4}\ \underline{0}\ \underline{4}\ \underline{0}\ \underline{0}$	0.5184	$5/8^5$
$\underline{0}\ \underline{0}\ -\underline{4}\ -\underline{1}\ -\underline{4}\ \underline{0}\ \underline{0}$	0.5376	$6/8^3$
$\underline{0}\ \underline{0}\ -\underline{4}\ \underline{4}\ \underline{4}\ -\underline{4}\ \underline{0}\ \underline{0}$	0.5376	$4/8^4$
$\underline{0}\ \underline{0}\ -\underline{4}\ \underline{4}\ \underline{0}\ -\underline{4}\ \underline{4}\ -\underline{4}\ \underline{4}\ \underline{0}\ \underline{0}$	0.5376	$6/8^6$
$\underline{0}\ \underline{0}\ -\underline{4}\ \underline{4}\ \underline{0}\ -\underline{4}\ \underline{0}\ \underline{4}\ \underline{0}\ \underline{0}$	0.5376	$4/8^4$
$\underline{0}\ \underline{0}\ -\underline{4}\ \underline{0}\ \underline{4}\ -\underline{4}\ \underline{0}\ \underline{4}\ \underline{0}\ \underline{0}$	0.5376	$4/8^4$
$\underline{0}\ \underline{0}\ -\underline{4}\ \underline{0}\ \underline{4}\ \underline{0}\ -\underline{4}\ \underline{4}\ \underline{0}\ \underline{0}$	0.5376	$4/8^4$
$\underline{0}\,\underline{0}\ -\underline{4}\ \underline{4}\ -\underline{4}\ \underline{0}\ \underline{4}\ -\underline{4}\ \underline{4}\ \underline{0}\ \underline{0}$	0.5376	$6/8^6$
$\underline{0}\ \underline{0}\ -\underline{4}\ \underline{4}\ -\underline{4}\ \underline{4}\ \underline{0}\ -\underline{4}\ \underline{4}\ \underline{0}\ \underline{0}$	0.5376	$6/8^6$
$\underline{0}\ \underline{0}\ -\underline{4}\ \underline{0}\ -\underline{4}\ \underline{0}\ -\underline{4}\ \underline{0}\ \underline{0}$	0.5440	$3/8^3$
$\underline{0}\,\underline{0}\ -\underline{4}\ \underline{0}\ \underline{4}\ -\underline{4}\ \underline{4}\ -\underline{4}\ \underline{4}\ \underline{0}\ \underline{0}$	0.5504	$6/8^6$
$\underline{0}\ \underline{0}\ -\underline{4}\ \underline{4}\ -\underline{4}\ \underline{4}\ -\underline{4}\ \underline{0}\ \underline{4}\ \underline{0}\ \underline{0}$	0.5504	$6/8^6$
$\underline{0}\ \underline{0}\ -\underline{4}\ -\underline{4}\ \underline{4}\ -\underline{4}\ \underline{0}\ \underline{0}$	0.5632	$4/8^4$
$\underline{0}\ \underline{0}\ -\underline{4}\ \underline{0}\ -\underline{4}\ \underline{0}\ \underline{4}\ -\underline{4}\ \underline{0}\ \underline{0}$	0.5632	$4/8^4$
$\underline{0}\ \underline{0}\ -\underline{4}\ \underline{0}\ -\underline{4}\ \underline{4}\ \underline{0}\,-\underline{4}\ \underline{0}\ \underline{0}$	0.5632	$4/8^4$
$\underline{0}\ \underline{0}\ -\underline{4}\ \underline{0}\ \underline{4}\ -\underline{4}\ \underline{0}\ -\underline{4}\ \underline{0}\ \underline{0}$	0.5632	$4/8^4$
$\underline{0}\ \underline{0}\ -\underline{4}\ \underline{4}\ -\underline{4}\ -\underline{4}\ \underline{0}\ \underline{0}$	0.5632	$4/8^4$
$\underline{0}\ \underline{0}\ -\underline{4}\ \underline{4}\ -\underline{4}\ \underline{0}\,-\underline{4}\ \underline{4}\ -\underline{4}\ \underline{0}\ \underline{0}$	0.5632	$6/8^6$
$\underline{0}\ \underline{0}\ -\underline{4}\ \underline{4}\ -\underline{4}\ \underline{4}\ \underline{0}\ \underline{4}\ -\underline{4}\ \underline{0}\ \underline{0}$	0.5632	$6/8^6$

Table 5.4 – continued from previous page

Error Event, λ	$d^2(\lambda)$	N_d
$\underline{0}\ \underline{0}\ -\underline{4}\ \underline{4}\ \underline{0}\ -\underline{4}\ \underline{0}\ -\underline{4}\ \underline{0}\ \underline{0}$	0.5632	$4/8^4$
$\underline{0}\ \underline{0}\ -\underline{4}\ \underline{0}\ \underline{4}\ \underline{0}\ \underline{4}\ -\underline{4}\ \underline{0}\ \underline{0}$	0.5632	$4/8^4$
$\underline{0}\ \underline{0}\ -\underline{4}\ \underline{4}\ -\underline{4}\ \underline{4}-\underline{4}\ \underline{4}\ -\underline{4}\ \underline{4}\ \underline{0}\ \underline{0}$	0.5632	$8/8^8$
$\underline{0}\ \underline{0}\ -\underline{4}\ \underline{4}\ \underline{0}\ \underline{4}\ -\underline{4}\ \underline{4}\ -\underline{4}\ \underline{0}\ \underline{0}$	0.5632	$6/8^6$
$\underline{0}\ \underline{0}\ -\underline{4}\ \underline{4}\ \underline{0}\ \underline{4}\ \underline{0}-\underline{4}\ \underline{0}\ \underline{0}$	0.5632	$4/8^4$
$\underline{0}\ \underline{0}\ -\underline{4}\ \underline{0}\ -\underline{4}\ \underline{4}\ -\underline{4}\ \underline{4}\ -\underline{4}\ \underline{0}\ \underline{0}$	0.5760	$6/8^6$
$\underline{0}\ \underline{0}\ -\underline{4}\ \underline{4}\ -\underline{4}\ \underline{4}-\underline{4}\ \underline{0}-\underline{4}\ \underline{0}\ \underline{0}$	0.5760	$6/8^6$
$\underline{0}\ \underline{0}\ -\underline{4}\ \underline{0}\ \underline{4}\ -\underline{4}\ \underline{0}\ \underline{4}\ -\underline{4}\ \underline{0}\ \underline{0}$	0.5824	$5/8^5$
$\underline{0}\ \underline{0}\ -\underline{4}\ \underline{4}\ \underline{0}\ -\underline{4}\ \underline{0}\ \underline{4}\ -\underline{4}\ \underline{0}\ \underline{0}$	0.5824	$5/8^5$
$\underline{0}\ \underline{0}\ -\underline{4}\ \underline{4}\ \underline{0}-\underline{4}\ \underline{4}\ \underline{0}\ -\underline{4}\ \underline{0}\ \underline{0}$	0.5824	$5/8^5$
$\underline{0}\ \underline{0}\ -\underline{4}\ \underline{0}\ -\underline{4}\ \underline{0}\ -\underline{4}\ \underline{4}\ \underline{0}\ \underline{0}$	0.5888	$4/8^4$
$\underline{0}\ \underline{0}\ -\underline{4}\ \underline{0}\ -\underline{4}\ \underline{4}\ \underline{0}\ \underline{4}\ \underline{0}\ \underline{0}$	0.5888	$4/8^4$
$\underline{0}\ \underline{0}\ -\underline{4}\ \underline{4}\ \underline{0}\ \underline{4}\ \underline{0}\ \underline{4}\ \underline{0}\ \underline{0}$	0.5888	$4/8^4$
$\underline{0}\,\underline{0}\ -\underline{4}\ \underline{0}\ \underline{4}\ -\underline{4}\ \underline{4}\ \underline{0}\ -\underline{4}\ \underline{0}\ \underline{0}$	0.5952	$5/8^5$
$\underline{0}\ \underline{0}\ -\underline{4}\ \underline{0}\ \underline{4}\ \underline{0}\ -\underline{4}\ \underline{4}\ -\underline{4}\ \underline{0}\ \underline{0}$	0.5952	$5/8^5$
$\underline{0}\ \underline{0}\ -\underline{4}\ \underline{4}\ -\underline{4}\ -\underline{4}\ \underline{4}\ \underline{0}\ \underline{0}$	0.5952	$5/8^5$
$\underline{0}\ \underline{0}\ -\underline{4}\ \underline{4}\ -\underline{4}\ \underline{0}\ \underline{4}\ -\underline{4}\ \underline{4}\ -\underline{4}\ \underline{0}\ \underline{0}$	0.5952	$7/8^7$
$\underline{0}\ \underline{0}\ -\underline{4}\ \underline{4}\ -\underline{4}\ \underline{0}\ \underline{4}\ \underline{0}\ -\underline{4}\ \underline{0}\ \underline{0}$	0.5952	$5/8^5$
$\underline{0}\ \underline{0}\ -\underline{4}\ \underline{4}\ -\underline{4}\ \underline{4}\ \underline{0}\ -\underline{4}\ \underline{4}\ -\underline{4}\ \underline{0}\ \underline{0}$	0.5952	$7/8^7$
$\underline{0}\ \underline{0}\ -\underline{4}\ \underline{4}\ \underline{0}\ -\underline{4}\ \underline{4}\ -\underline{4}\ \underline{4}\ -\underline{4}\ \underline{0}\ \underline{0}$	0.5952	$7/8^7$
$\underline{0}\ \underline{0}\ -\underline{4}\ \underline{4}\ \underline{0}\ -\underline{4}\ \underline{4}\ \underline{0}\ \underline{0}$	0.5952	$4/8^4$
$\underline{0}\ \underline{0}\ -\underline{4}\ \underline{4}\ -\underline{4}\ \underline{4}\ -\underline{4}\ \underline{0}\ \underline{4}\ -\underline{4}\ \underline{0}\ \underline{0}$	0.5952	$7/8^7$

5.6 Conclusions

In this chapter, we studied the effect of varying levels of inter-track interference (ITI) on the performance of optimal bit detectors for bit patterned media (BPM) recording channels. For this, we considered a simplified family of BPM channel models described by a single parameter for intersymbol interference (ISI) and a single parameter for ITI. We presented simulated bit-error-rate (BER) curves for a maximum *a posteriori* (MAP) bit detector on representative

channels in this family, as a function of the ITI parameter. For channels both with and without ISI, we observed that, in a range of values of the ITI parameter, the detector performance improved as the level of ITI was increased. In the presence of track misregistration (TMR), we observed a similar phenomenon. For the no-ISI case, this behavior was explained by means of an exact probability of error analysis for the MAP bit detector. For channels with ISI, we used an error event analysis of a punctured maximum-likelihood (ML) joint-track detector to shed light on the improvement in performance that can accompany an increased level of ITI within a certain range of ITI parameter values.

Acknowledgment

Portions of this chapter appear in the paper: S. Karakulak, P. H. Siegel, and J. K. Wolf, "A Parametric Study of Inter-Track Interference in Bit Patterned Media Record," *IEEE Trans. Magn.*, vol. 46, pp. 819-824, Mar. 2010.

Bibliography

[1] S. Karakulak, P. H. Siegel, J. K. Wolf, and H. N. Bertram, "A new read channel model for patterned media storage," *IEEE Trans. Magn.*, vol. 44, pp. 193–197, Jan. 2008.

[2] H. Burkhardt, "Optimal data retrieval for high density storage," *Proc. CompEuro '89., VLSI and Computer Peripherals. VLSI and Microelectronic Applications in Intelligent Peripherals and their Interconnection Networks*, pp. 43–48, May 1989.

[3] L. Bahl, J. Cocke, F. Jelinek, and J. Raviv, "Optimal decoding of linear codes for minimizing symbol error rate," *IEEE Trans. Inform. Theory*, vol. IT-20, pp. 284–287, Mar. 1974.

[4] W. Tan and J. R. Cruz, "Evaluation of detection algorithms for perpendicular recording channels with inter-track interference," *Journal of Magnetism and Magnetic Materials*, vol. 287, pp. 397–404, 2005.

[5] B. G. Roh, S. U. Lee, J. Moon, and Y. Chen, "Single-head/single-track detection in interfering tracks," *IEEE Trans. Magn.*, vol. 38, pp. 1830–1838, July 2002.

[6] S. Karakulak, P. H. Siegel, J. K. Wolf, and H. N. Bertram, "Equalization and detection in patterned media recording," *Intermag Dig. of Tech. Papers*, p. HT10, May 2008.

[7] S. Karakulak, P. H. Siegel, J. K. Wolf, and H. N. Bertram, "Joint-track equalization and detection in patterned media recording," submitted to *IEEE Trans. Magn.*, 2008.

[8] H. Suzuki, W. C. Messner, J. A. Bain, V. Bhagavatula, and S. Nabavi, “A method for simultaneous position and timing error detection for bit-patterned media,” *IEEE Trans. Magn.*, vol. 45, pp. 3749–3752, Oct. 2009.

[9] A. D. Weathers, S. A. Altekar, and J. K. Wolf, “Distance spectra for PRML channels,” *IEEE Trans. Magn.*, vol. 33, pp. 2809–2811, Sept. 1997.

[10] S. A. Altekar, “Detection and coding techniques for magnetic recording channels.” Ph.D. dissertation, University of California, San Diego, 1997.

[11] G. D. Forney, “Maximum-likelihood sequence estimation of digital sequences in the presence of intersymbol interference,” *IEEE Trans. Inform. Theory*, vol. IT-18, pp. 363–378, May 1972.